# THE EFFECT OF BIOFUEL IMPURITIES ON THE HOT CORROSION OF YTTRIA-STABILIZED ZIRCONIA THERMAL BARRIER COATINGS

by

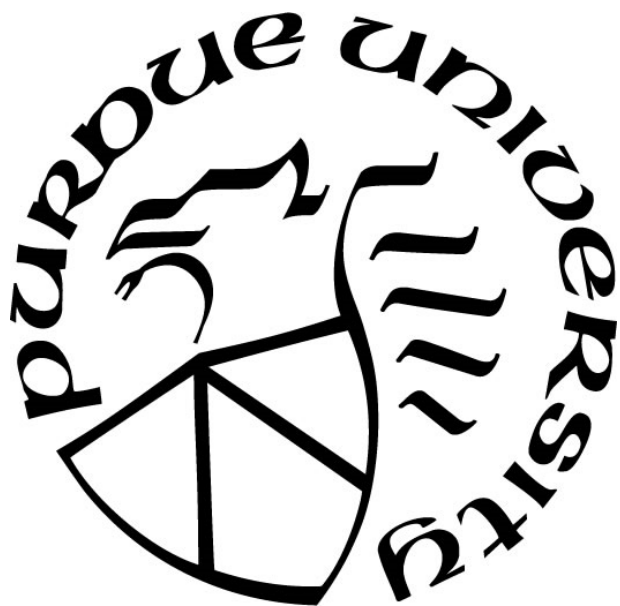**Jorge Hugo Ramirez Velasco**

**A Dissertation**

*Submitted to the Faculty of Purdue University*

*In Partial Fulfillment of the Requirements for the degree of*

**Doctor of Philosophy**

School of Materials Engineering

West Lafayette, Indiana

December 2019

# THE PURDUE UNIVERSITY GRADUATE SCHOOL
# STATEMENT OF COMMITTEE APPROVAL

**Dr. Rodney W. Trice**

School of Materials Engineering

**Dr. Kevin Trumble**

School of Materials Engineering

**Dr. Mysore Dayananda**

School of Materials Engineering

**Dr. Elliott B. Slamovich**

School of Materials Engineering

**Approved by:**

Dr. David Bahr

*The present work is dedicated to the persons who gave up everything so I could chase my dreams. Their life lessons, principles, and values will perdure for the rest of my life.*

*Thanks, Mom, Dad, and Sister.*

# ACKNOWLEDGMENTS

I am thankful to god for being a source of strength and the blessings that were bestowed upon me. I want to thank and give my most profound appreciation to my advisor Prof. Rodney W. Trice, for his continuous support and encouragement. His dedication to improving the quality of my work and my development as a researcher was invaluable to complete the work required for this thesis. I will keep in my heart and memories all the time we spent together.

I would also like to express my gratitude to my committee members, Prof. Dayananda, Prof. Slamovich, and Prof. Trumble, for their lessons inside and outside the classroom; our conversations not only had a positive impact in my work but also in my personal life. I am grateful to distinguished professor Hilkka Kenttämaa, and professor Gozdem Kilaz for allowing me to collaborate with them, their support and assistance through my Ph.D. were of help shaping the fundamental ideas to conclude my degree. I take this opportunity to give a special mention to Dr. Ashlin G. Porter, Dr. Mark Romanczyk, and Dr. Eduardo Barocio Vaca for their unconditional friendship. I will always keep in my mind their vision of humanity and their perception of life in every decision I will take.

# TABLE OF CONTENTS

# LIST OF TABLES

# LIST OF FIGURES

# EXTRA HEADINGS

## List of Abbreviations

| | |
|---|---|
| APS | Air Plasma Spray |
| ASTM | American Society for Testing and Materials |
| BSE | Back-Scattered Electrons |
| CMAS | Calcium-Magnesium-Aluminum Silicates |
| CTE | Coefficient of Thermal Expansion |
| c-YSZ | Cubic YSZ |
| DVC | Dense Vertically Cracked |
| EB-PVD | Electron Beam Physical Vapor Deposition |
| EDS | Energy Dispersive Spectroscopy |
| FT-S8 | Fischer-Tropsch |
| GE | General Electric |
| HEFA | Hydro processed Esters and Fatty Acid |
| HVOF | High-Velocity Oxy-Fuel |
| LW | Long Wavelength |
| m-YSZ | Monoclinic YSZ |
| NASA | National Aeronautics and Space Administration |
| NIR | Near Infra-Red |
| PM | Particulate Matter |
| SEM | Scanning Electron Microscope |
| SIP | Synthesized Iso-Paraffins |
| SW | Specialty Wavelength |
| TBC | Thermal Barrier Coating |
| $T_{evap}$ | Evaporation Temperature |
| TIT | Turbine Inlet Temperature |
| t'-YSZ | Metastable Tetragonal YSZ |
| t-YSZ | Tetragonal YSZ |
| XRD | X-Ray Diffraction |
| YSZ | Yttria-Stabilized Zirconia |

## Variables

| | |
|---|---|
| $\Delta p$ | Driving Pressure |
| $C_p$ | Specific Heat |
| k | Viscosity |
| k | Permeability |
| $k$ | Thermal Conductivity |
| L | Cross-Sectional Thickness |
| $\lambda$ | Wavelength |
| $\varnothing$ | Pore Fraction |
| r | Pore Radius |
| T | Temperature |
| v | Velocity |
| $\Gamma$ | Intercolumnar pore radius |
| $\varepsilon$ | Emissivity |
| $\theta$ | Contact angle |
| $\rho$ | Density |
| $\sigma_{LV}$ | Surface Tension |
| $\tau$ | Tortuosity factor |

# ABSTRACT

Yttria-stabilized zirconia (YSZ) thermal barrier coatings (TBCs) provide thermal and environmental protection to superalloy components operating within the combustor and high-pressure sections of a gas turbine. However, calcium-magnesium-aluminum silicate (CMAS) deposits originated from particulate matter ingested through the air intake degrade YSZ TBCs, ultimately decreasing the overall efficiency of the engines. With the introduction of biofuels into gas turbines, a new list of impurities with no precedent in jet engines may interact with TBCs, arising the possibility to form CMAS deposits without flying in a particular environment and to exacerbate CMAS negative effect through the addition of other contaminants.

In this work, a cyclic thermal gradient rig was developed to test TBCs in similar conditions as in a gas turbine. The heat flux and non-contact surface temperature measurements were validated with a thermal transient model. The effect of biofuel impurities on YSZ TBCs was evaluated by spraying the coatings with impurity cocktails, solutions containing the impurities of interest, and subsequently testing their lifetimes in the ablation rig.

Detailed microstructure analysis revealed that APS and EB-PVD TBCs fail in different ways when exposed to equal concentrations of CMAS. When contaminating APS TBCs with varying combinations of CMAS constituents (e.g., S, C-S, C-A, C-A-S, C-M-S, C-M-A-S), it was possible to identify that coatings delaminated at different rates depending on the combination of CMAS constituents. Finally, the effect of CMAS in combination with contaminants exclusive of biofuels was analyzed on YSZ TBCs. X-ray diffraction (XRD) analysis and micrographs revealed that glass modifiers (e.g., $K_2O$ and $ZnO$) accelerated the degradation of YSZ TBCs.

# 1. INTRODUCTION

## 1.1 Motivation and scope of thermal barrier coatings

Aircraft propulsion, industrial power generation, and marine applications have highlighted the critical role of gas turbines in modern society. Since the 1970s, the unceasing demand for higher efficiency and power ratings have driven a continuous effort to increase gas turbines operating temperatures. Currently, components for these applications must withstand temperatures of at least 1400°C when operating within the combustor and the high-pressure sections of a gas turbine engine [1]. With superalloys operating at its maximum capacity, ceramic multilayered materials systems known as thermal barrier coatings (TBCs) are employed as thermal and environmental protections [2–4]. Fig. 1.1 shows a TBC cross-section superimposed with the temperature gradient between the cooling air channels and the hot combustion gases. The increase of in-service temperature has also come with new challenges, the severity of thermal cycling fatigue and hot corrosion, commonly thermally activated processes, has also increased.
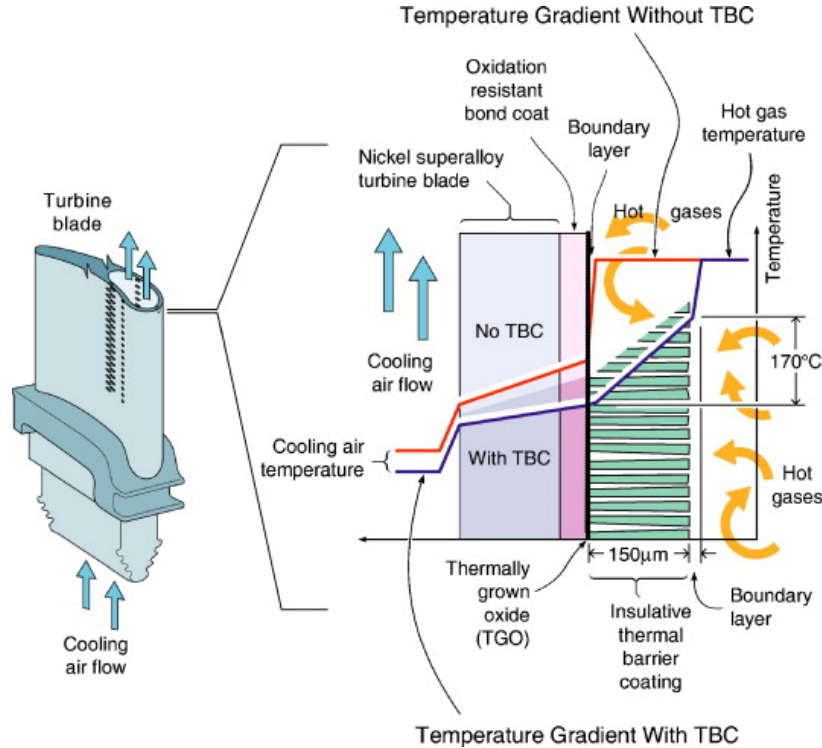


Fig. 1.1. Schematic illustration of a thermal barrier coating consisting of an insulative coating (topcoat), a bondcoat (commonly a Ni or Al alloy), and a substrate (superalloy) [5].

14

## 1.2 The functionality of yttria stabilized zirconia thermal barrier coatings

Finding ceramic materials that can withstand extreme temperatures without compromising the mechanical endurance for gas turbine components is challenging. Zirconia ($ZrO_2$) is among a small group of materials that has the necessary thermomechanical properties for TBCs [6]. However, under thermal cycling, pure zirconia undergoes allotropic transformations that disrupt the microstructure properties: monoclinic(m)→tetragonal(t) at 1170°C and tetragonal(t)→cubic(c) at 2370°C. Specifically, there is a 4-6% volume change associated with the monoclinic→tetragonal phase transformation that develops mechanical stresses, precluding the use of pure zirconia in TBC applications [7,8]. Fig. 1.2 shows that doping zirconia with the aliovalent oxide yttria ($Y_2O_3$), the microstructure is stabilized in a tetragonal+cubic phase above ~1050°C. However, on cooling and with no mechanical constraints, a transformation resulting in a mixture of monoclinic and cubic phases occurs. Because of the nature of the coating deposition techniques, nonequilibrium processes, the deposition of yttria-stabilized zirconia (YSZ) alloy results in a metastable tetragonal-prime (t') phase, described as a single phase with tetragonal structure but supersaturated with yttrium. The deposited complex t' phase is commonly known as a "non-transformable t'-$ZrO_2$" primarily due to its resistance to undergo the t→m transformation and crack propagation. Consequently, t'-YSZ TBCs have the most significant durability as topcoat.
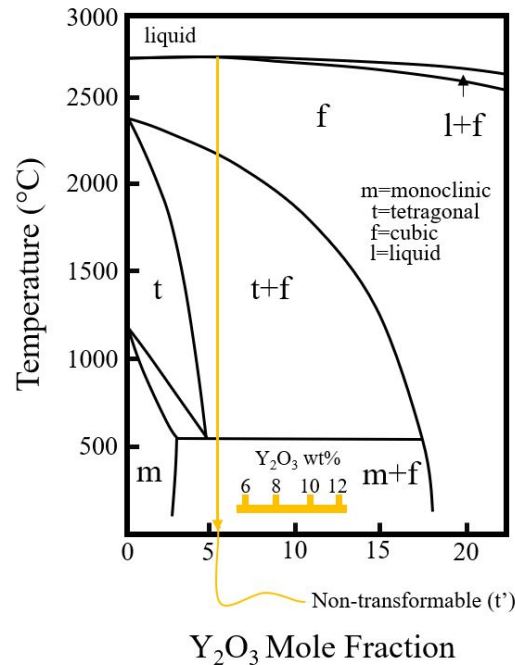


Fig. 1.2. Binary phase diagram of $ZrO_2$-$Y_2O_3$. Adapted from R. Ghasemi et al. (2013) [9].

By conducting a durability test, NASA determined the ideal yttria content to extend a TBC lifetime. Fig. 1.3 shows that the 7-8wt.% $Y_2O_3$ content in zirconia has the highest durability as TBC [10].
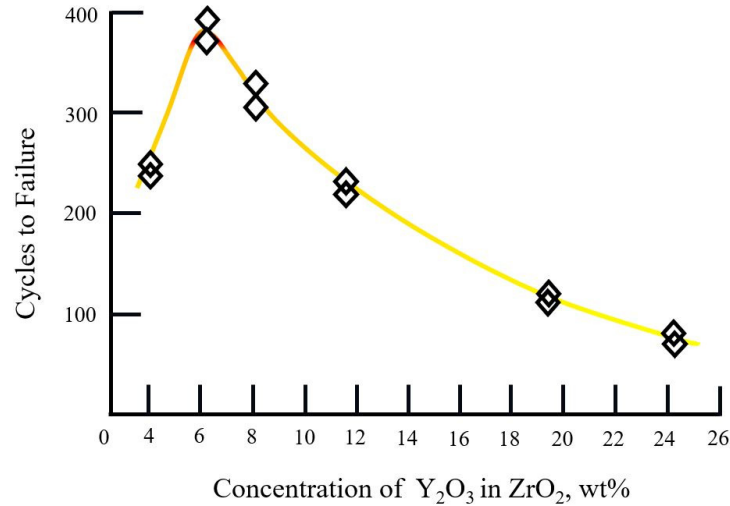


Fig. 1.3. The durability of YSZ TBCs as a function of yttria content. Adapted from Stecura. S [10].

Because of the 7wt.% $Y_2O_3$-$ZrO_2$ (YSZ) melting point, conventional coating techniques are not practical, and limited manufacturing technologies are available. Currently, the deposition methods for most YSZ TBCs are either air plasma spray (APS) or electron beam physical vapor deposition (EB-PVD). APS coatings are typically used for large stationary components such as the combustor while EB-PVD coatings are favored on turbine airfoils (e.g., blades and vanes) that require a smooth surface of high aerodynamic quality [11]. Fig. 1.4 illustrates the two microstructures achieved when using APS and EB-PVD deposition processes.
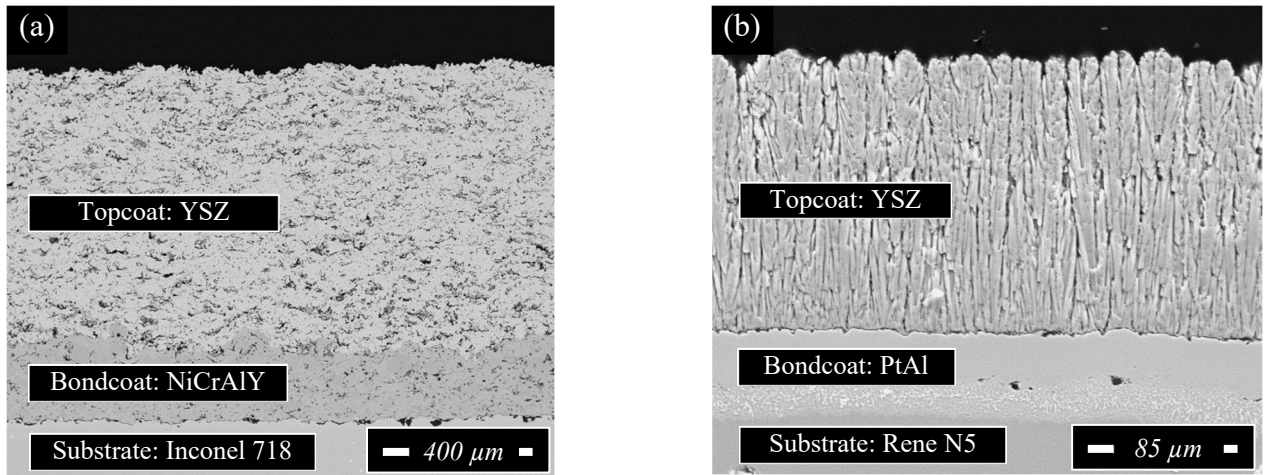


Fig. 1.4. SEM micrographs of YSZ TBCs deposited by (a) APS and (b) EB-PVD

### 1.3 Hot corrosion of YSZ TBCs induced by CMAS and biofuel impurities

With the maximum operating temperature of gas turbines increasing to 1250ºC and above, a new problem has emerged for YSZ TBCs that has been of concern over the last decade [12–14]. Calcium-magnesium-aluminum silicates or CMAS, a particulate common to the middle east regions or found in volcanic ash, can be pulled into a gas turbine. Depending on the composition of the particulate, it can melt and infiltrate into the TBC via the porous pathways in either the APS or EB-PVD microstructures. Upon cooling, the compliance difference between infiltrated and non-infiltrated coating regions causes residual stresses that delaminate the infiltrated coating.

There is currently momentum increase biofuel use in gas turbines. For example, United Airlines flights between Los Angeles and San Francisco, have been using a blend of 70% Jet-A (fossil fuel) and 30% biofuel since 2016. Biofuels can be formed via numerous biomass processing approaches, using a multitude of different biomasses to include wheat, willow, and even olive waste [15]. It has been well established that contaminants found in fossil fuels such as Jet-A can be incorporated into TBCs, ultimately hastening their failure through a variety of different corroding mechanisms. Contaminants found in fossil fuels include S, V, Na, Ca, K, and P [16]. With the use of biofuels, however, a new group of contaminants must be considered. Literature reports show that the concentration of impurities present in biofuels depends directly on the biomass source. The composition of impurities in the biomass source is highly variable due to its dependence on factors such as harvest season, soil composition, and drying temperature. This list includes Al, Ba, Ca, Fe, K, Mg, Na, P, and Si [17]. Inspection of this list reveals that those same elements found in particulate forms of CMAS are found as individual constituents in biofuels. Thus, a gas turbine operating with biofuels could be exposed to the constituents of CMAS without ever being operated in the middle east or a volcanic ash environment. While extensive studies of the effect of fossil fuel impurities have been performed previously [18–21], the effect of impurities and oxides of alkali and alkaline metals found in commercial and military biofuel blends (e.g., HEFA, FT-S8, SIP) is still unknown. The growing importance of biofuels worldwide makes necessary a specific understanding of the possible adverse effects of biofuel impurities to avoid premature failure of TBCs used in gas turbines.

Because of its potential effects, impurities infiltration velocity into TBCs is of concern. By inspecting infiltrated YSZ coatings, Krämer et al. [22] concluded that molten CMAS spreads over the lamellar/columnar surfaces and penetrates any small capillaries. This observation implicates that the model of a liquid infiltrating a porous material can describe molten CMAS infiltration behavior. Thus, Darcy's Law (Eq. 1.1) can be applied to calculate the velocity, v, at which molten species infiltrate through the TBC cross-sectional thickness, L [23].

$$v = \frac{k}{\mu}\left(\frac{\Delta p}{L}\right) \tag{1.1}$$

Inspection of Eq.1.1 reveals that for the infiltration velocity calculation, the permeability of the coating, k, viscosity of the molten impurities, $\mu$, and the pressure driving the liquid, $\Delta P$, must be known. By considering the intercolumnar spaces of an EB-PVD TBC as cylindrical channels of radius, r, application of the Carman-Kozeny permeability model is possible:

$$k \approx \frac{r^2}{8\tau^2}\phi \tag{1.2}$$

Where, for ideal straight intercolumnar gaps, the tortuosity factor, $\tau=1$, and the pore fraction, $\phi$, is given by the TBC manufacturing specifications. Similarly, an expression that describes the pressure driving permeation of a liquid (e.g., molten CMAS) is [24]:

$$\Delta p \approx \frac{2\sigma_{LV}}{\Gamma}cos\theta \tag{1.3}$$

Where $\sigma_{LV}$ is the surface tension of the liquid, $\Gamma$ the intercolumnar pore radius, and $\theta$ the contact angle. Integrating Eq. 1.1 and combining with Eq. 1.2 & 1.3, the expression describing the necessary time for CMAS to infiltrated the coating thickness, L, is:

$$t \approx \frac{2\tau^2}{r\phi}\left(\frac{\mu}{\sigma_{LV}}\right)L^2 \tag{1.4}$$

If the intercolumnar gap size and coating thickness are known, Eq. 1.4 reveals that the molten species surface tension, $\sigma_{LV}$, and viscosity, $\mu$, are missing. According to Kucuk et al. [25], molten CMAS surface tension can be estimated from the oxides wt.% concentrations by:

$$\sigma_{LV}\left(\frac{mJ}{m^2}\right) = 21.72 + 3.32[CaO] + 1.96[MgO] + 3.47[Al_2O_3] \tag{1.5}$$

Finally, the melt viscosity has been modeled experimentally by NASA [26] as a function of temperature:

$$\log(n) = 2.59 + \frac{2418}{T - 759.4} \tag{1.6}$$

Calculations by Zhao et al. [27] using a 200µm thick 7YSZ TBC and a CMAS model, 33CaO–9MgO–13AlO$_{1.5}$–45SiO$_2$, speculated to melt at 1250°C, predicted impurities infiltration just 15 seconds upon melting. Experimental measurements of the same parameters as the calculations validated the theoretical model. Fig. 1.5 shows the cross-sectional views of the EB-PVD used for the CMAS infiltration experiment at 1400°C. To validate the presence of impurities, the Ca concentration respect to Zr was measured. After just 1 minute of exposure, the Ca/Zr ratio average was 0.1 across the coating (Fig. 1.5a). The same ratio along the entire thickness indicated impurities full infiltration. After 4 hours of exposure, the remeasure of the ratio was 0.14 (Fig. 1.5b). Thus, the increase in concentration was not significative respect to the first time frame.
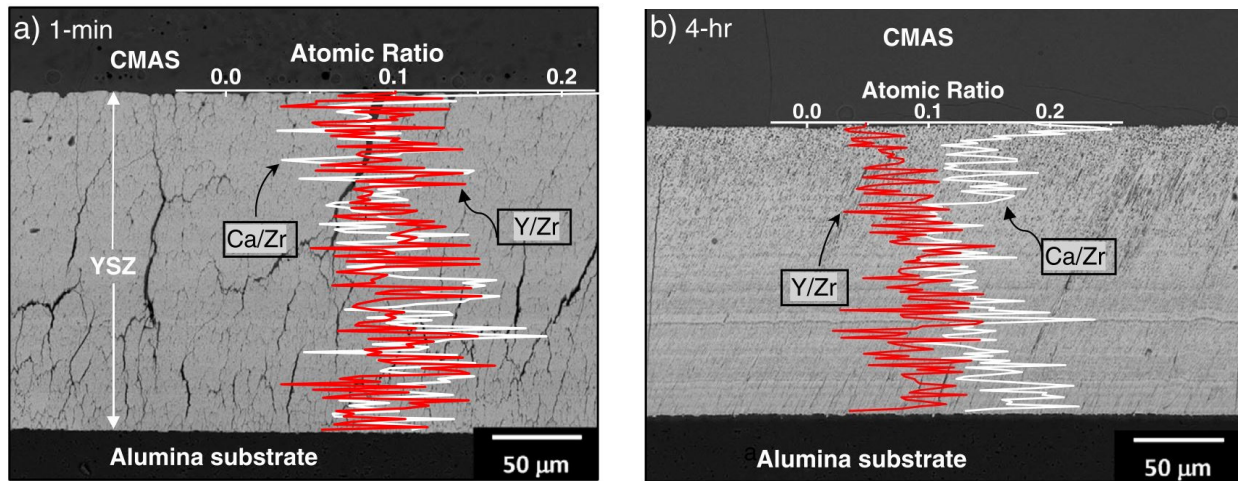


Fig. 1.5. Depth deposition analysis for 7YSZ samples exposed to CMAS at 125°C for (a) 1 min and (b) 4 hrs.

Even though observations validated the model proposed by Krämer et al. [22], it is evident that molten species surface tension, and viscosity, have a chemical composition dependence. Because of the potential effects of fuel contaminants, similar studies taking into consideration biofuels impurities compounds are necessary. Moreover, a detailed comparison of molten impurities infiltrating APS and EB-PVD TBCs is unavailable in the literature.

## 1.4  Degradation mechanisms of TBCs by molten impurities

Experimental studies and theory demonstrate that external contaminants can infiltrate TBCs in short times upon melting. Currently, coatings infiltration by molten impurities is considered the primary cause of TBCs' premature degradation. Therefore, understanding the degradation mechanisms of YSZ/CMAS is necessary to mitigate the negative effect of molten impurities on TBCs. Thus far, the scientific community has identified two degradation mechanisms [14]. The first one (thermomechanical effect) proposes that when the coating surface temperature is high enough, impurities infiltrate into the TBC via different pathways, upon solidification, the stiffening effect of the reaction products causes crack nucleation, and propagation [28]. Extensive studies of these mechanisms have resulted in mathematical models that are in agreement with observations [29, 30]. However, recent examinations of ex-service components revealed a second mechanism associated with the chemical reactions occurring at high temperatures (e.g., corrosion, erosion), suggesting that the YSZ/CMAS local chemistry exacerbates the spallation of  TBCs.  Fig. 1.6 illustrates both degradation mechanisms [27].
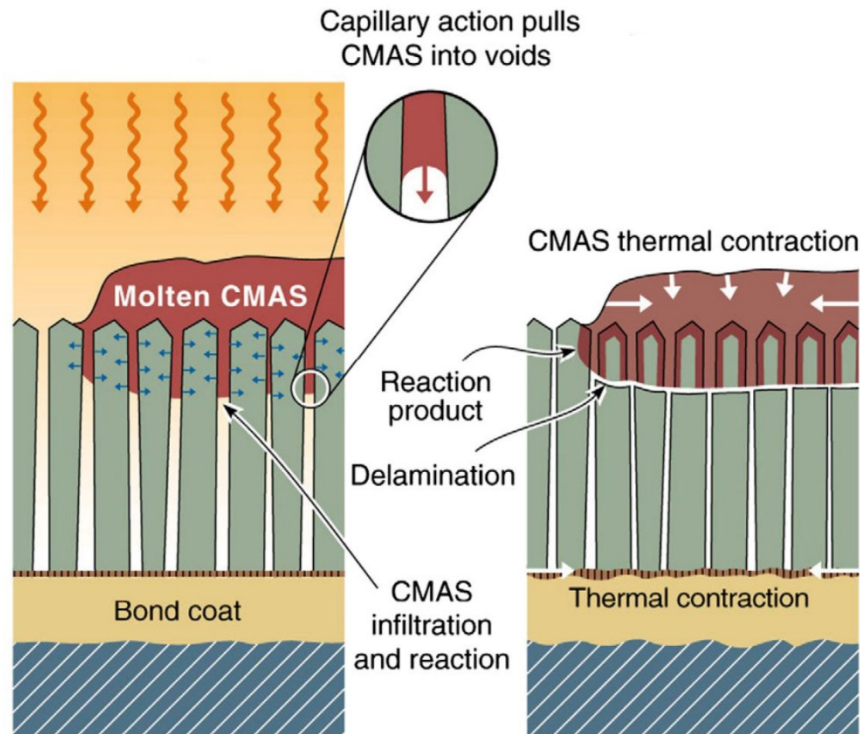


Fig. 1.6. Illustration of molten silicates melting, penetrating, and reacting through the inter-column spaces of an EB-PVD coating. The molten impurities solidify when reaching colder areas than its melting point and subsequently induce delamination [27].

### 1.4.1  Thermochemical degradation of YSZ TBCs by molten impurities

The interaction of YSZ and CMAS, in combination with thermal gradients, cause visible delamination that can be identified inherently as a thermomechanical effect. On the other hand, the thermochemical interaction at high temperatures has not been as prominent. X-ray diffraction (XRD) unveiled evidence about chemical reactions between molten impurities and YSZ. By analyzing spalled debris from ex-service components exposed to CMAS, XRD patterns exhibited the tetragonal peaks characteristic of YSZ. However, the same diffractograms revealed additional peaks identified as the undesired YSZ monoclinic phase. Fig. 1.7 shows the XRD pattern of an ex-service gas turbine shroud exposed to CMAS [14], the diffractogram exhibits the tetragonal and monoclinic peaks of YSZ, and also traces of Ca base compounds. Similar observations led to the conclusion that the chemical reactions of YSZ and CMAS resulted in destabilization of t'-YSZ that lead to a faster TBC degradation.
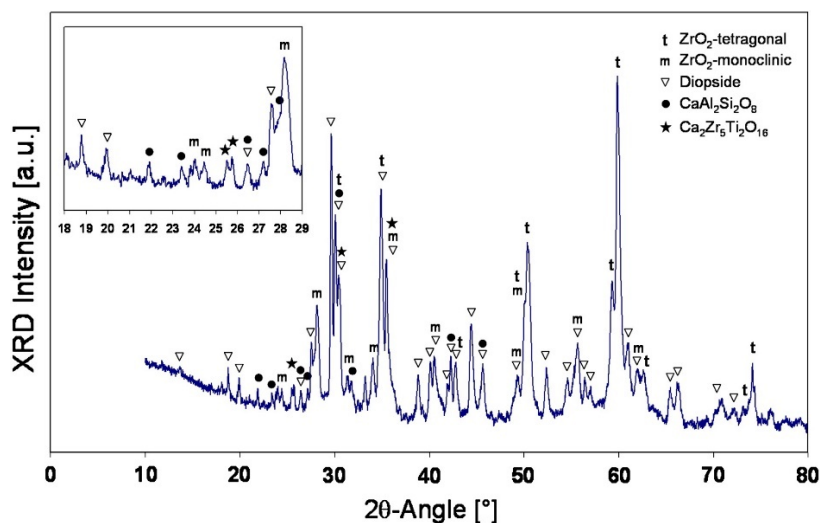


Figure 1.7. X-ray diffraction pattern of CMAS covered TBC from a gas turbine shroud [14].

The presence of numerous reaction products in ex-service components, attributed to highly variable flight environment conditions, has difficulted the study of the thermochemical interaction of CMAS and YSZ. Thus, studying the adverse effect of CMAS has become a challenge. For this reason, the formulation of simplified synthetic models of impurities that can replicate the interactions of molten species and TBCs is a viable option to study the thermochemical interactions. The most common approach is to simulate CMAS composition by mixing fine powders of the primary oxides and carbonates.

**1.4.2   Thermomechanical degradation of YSZ TBCs by molten impurities**

Validation of synthetic CMAS models has been done extensively in the literature. Pujol et al. [13] compared the XRD patterns of three samples exposed to a sol-gel CMAS model for 2 hours at temperatures above and below the solution melting point (1250°C) and a reference sample treated at 1350°C  without impurities (Fig. 1.8). The peaks comparison revealed that the sample exposed to CMAS at 1100°C, below the CMAS melting point, did not exhibit the t→m phase transformation. Nonetheless, the diffractogram exhibited peaks attributed to CMAS recrystallization.

On the other hand, both samples exposed to the CMAS model at 1250°C and 1350°C, above the CMAS melting point, manifested peaks related to monoclinic YSZ. Altogether, it indicated that the synthetic model behaved at low and high temperatures as the real CMAS compound. Finally, the sample treated at 1350°C without impurities did not exhibit new peaks. Therefore, the chemical interaction of YSZ and the synthetic model of CMAS caused the observed changes in the crystal structure of the TBC.
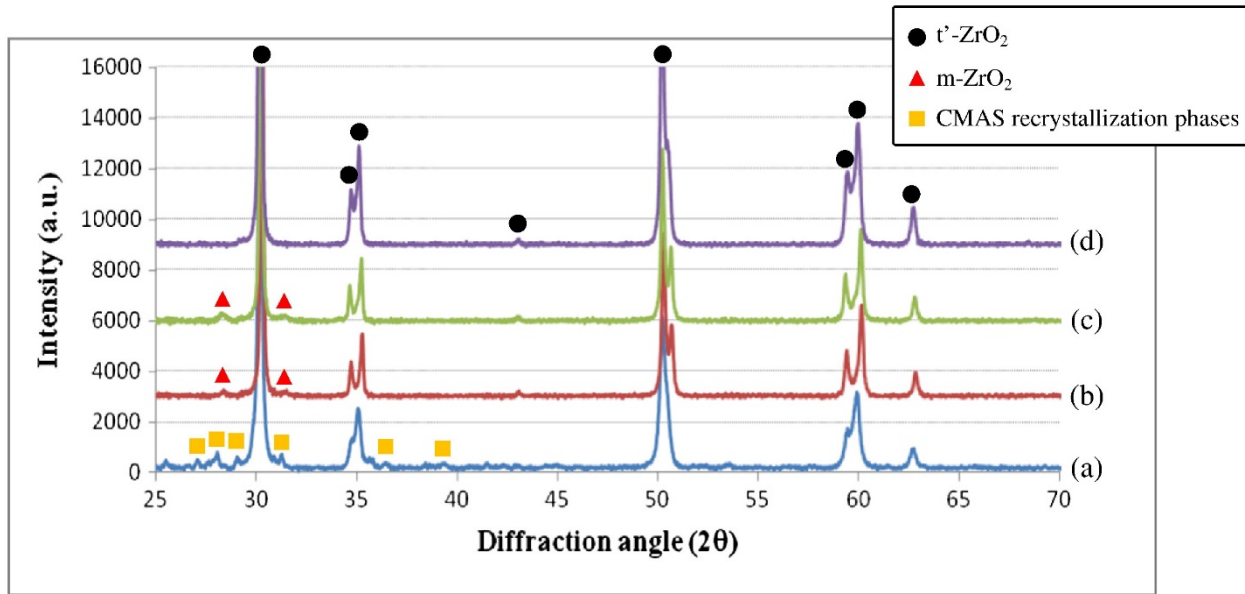


Fig. 1.8. X-ray diffraction patterns of YSZ powder after exposed to sol-gel CMAS for 2 hrs at (a) 1100°C, (b) 1250°C, (c) 1350°C, and (d) YSZ powder without CMAS heat threated at 1350°C for 2 hrs [13].

By employing artificial CMAS models and replicating gas turbines operation conditions, it has been easier to analyze and compare the effect of molten impurities in a controlled environment. Scanning electron microscopy (SEM) has revealed that the disruptive YSZ t→m phase transformation goes along with composition and morphological changes. Vidal-Setif et al. [31] observed dense globular particles primarily on the columnar tips of EB-PVD coatings exposed to synthetic impurities, differing substantially from the original faceted shape of the columns. Energy dispersive x-ray spectroscopy (EDS) analysis has shown that the dense globular morphology has a lower $Y_2O_3$ content (<5%) than the tetragonal phase. Thus, the "non-porous" area on the top of the tips is, in reality, the monoclinic phase of YSZ. Fig. 1.9 shows the monoclinic and tetragonal phases distinguishable by their morphology in the SEM micrograph and composition difference in the elemental maps [32].
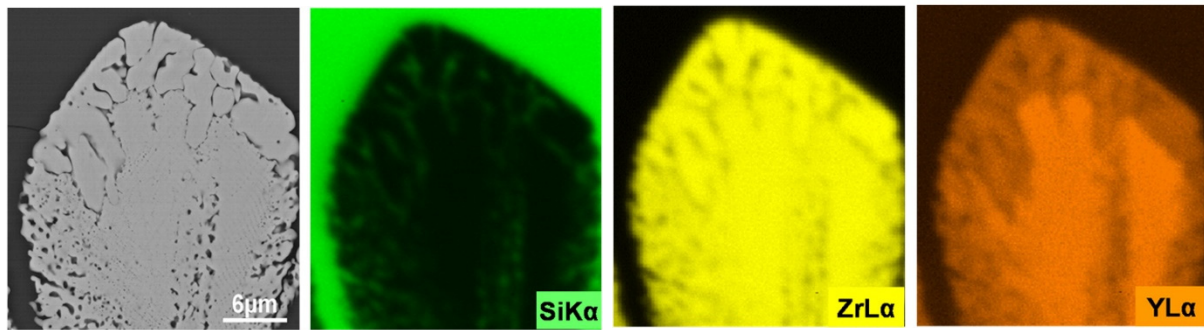


Fig. 1.9. SEM micrograph of YSZ column tip after 4 hrs of exposure to CAS at 1200°C and the corresponding Si, Y, and Zr elemental maps. Yttria elemental map reveals two different concentration zones matching the SEM porous area (t'-ZrO2) and a dense globular area (m-ZrO$_2$). Adapted from Vidal-Setif et al. [32].

The process by which the monoclinic globular microstructure forms is as follows. CMAS infiltrates into the TBC at temperatures above 1250°C, and dissolution is observed only in the columnar tips where a large volume of CMAS is available. Thus, interactions in the columnar bulk are not observed because of the small CMAS/YSZ ratio in comparison to the observed ratio at the surface [22]. In the columnar tips where dissolution takes place, yttria concentration in the melt increases sufficiently that upon cooling, precipitation of a monoclinic phase occurs. The dissolution-precipitation mechanism explains the physical interface between the two phases. Even though this process is coherent with the observations, questions concerning varying impurities

composition, degradation role of each of the individual molten compounds, the dissolution rate of the TBC, and mitigation strategies for CMAS attack are still under study.

The mechanism and rate by which the reaction takes place are still under debate. However, conclusions recognizing the sequence and composition by which YSZ dissolves and re-precipitates simplify the problem to approximate the degradation rate. These observations can set the process and concentration limits that govern the maximum/minimum degradation rates of YSZ. Also, composition measurements show that the monoclinic phase precipitated from the melt is primarily a compound of zirconia lower in yttria and with minimum calcium content, indicating that MgO and $Al_2O_3$ in the CMAS melt do not affect substantially YSZ solubility in the melt [14].

## 1.5    Summary and objectives

Thermal barrier coatings are a necessary future in gas turbines to increase the overall efficiency of the engines. Unfortunately, environmental and fuel contaminants that deposit on TBCs in the form of ash or sand degrade the TBCs. Ultimately the degradation and failure of TBCs reduce the efficiency of gas turbines. Unlikely to volcanic ash and desert sand, the introduction of biofuels to gas turbines carries a new list of contaminants with no precedent in aircraft engines. Studies in literature have reported the effect of CMAS and fossil-derived fuel contaminants, but a few or none have analyzed the effect of impurities exclusive of biofuels.

Moreover, CMAS literature reports are carried out in different cycle tests (e.g., Tube furnace, Burner Rig, Laser Ablation), different thermal cycling parameters (i.e., heating and cooling periods), and multiple methodologies to synthesize and deposit the contaminants of interest on the TBCs, making difficult to compare with previous studies the effect of impurities exclusive of Biofuels on TBCs. In this work, we developed and validated a methodology that allows us to normalize contaminants composition, the deposited concentrations of contaminants on the coatings, and the thermal conditions for TBCs evaluation. The primary objective was to evaluate combinations of CMAS constituents (i.e., $CaO-MgO-Al_2O_3-SiO_2$) on TBCs and their behavior when interacting with other impurities exclusive of biofuels.

## 1.6    References

[1]     R. a. Miller, "Thermal barrier coatings for aircraft engines: History and directions," *J. Therm. Spray Technol.*, **6** [1] 35–42 (1995).

[2]     R.C. Reed., *The superalloys: fundamentals and applications.* Cambridge University Press; 2006, n.d.

[3]     R.A. Miller, "History of Thermal Barrier Coatings for Gas Turbine Engines," [March 2009] (2009).

[4]     F.O.R. Aeronautics, "Review of an Investigation of Ceramic Coatings for," [March] (1947).

[5]     Z. Yu, K.P. Dharmasena, D.D. Hass, and H.N.G. Wadley, "Vapor deposition of platinum alloyed nickel aluminide coatings," *Surf. Coatings Technol.*, **201** [6] 2326–2334 (2006).

[6]     J.T. Demasi-Marcin and D.K. Gupta, "Protective coatings in the gas turbine engine," **69** 1–9 (1994).

[7]     R. Eriksson, *High-temperature degradation of plasma sprayed thermal barrier coating systems*. 2011.

[8]     B. Rashkova, "Microstructural Characterization of Yttria-Stabilized Zirconia Thermal Barrier Coatings Grown on Sapphire Substrates," *Max-Planck-Institut für Met.*, [145] (2003).

[9]     R. Ghasemi, R. Shoja-Razavi, R. Mozafarinia, and H. Jamali, "Comparison of microstructure and mechanical properties of plasma-sprayed nanostructured and conventional yttria-stabilized zirconia thermal barrier coatings," *Ceram. Int.*, **39** [8] 8805–8813 (2013).

[10]    Stephan Stecura (Lewis Research Center), "Optimization of the NiCrAI-Y / ZrO2-Y203 Thermal Barrier System" (2017).

[11]    H.S. Materials, O. Committee, H.S. Materials, T. Systems, C. Isbn, T. Pdf, N.A. Press, N.A. Press, *et al.*, *Coatings for High-Temperature Structural Materials*. 1996.

[12]    M.P. Borom, C.A. Johnson, and L.A. Peluso, "Role of environment deposits and operating surface temperature in spallation of air plasma sprayed thermal barrier coatings," *Surf. Coatings Technol.*, **86**–**87** 116–126 (1996).

[13]    G. Pujol, F. Ansart, J.P. Bonino, A. Malié, and S. Hamadi, "Step-by-step investigation of degradation mechanisms induced by CMAS attack on YSZ materials for TBC applications," *Surf. Coatings Technol.*, **237** 71–78 (2013).

[14]    M.H. Vidal-Setif, N. Chellah, C. Rio, C. Sanchez, and O. Lavigne, "Calcium-magnesium-alumino-silicate (CMAS) degradation of EB-PVD thermal barrier coatings: Characterization of CMAS damage on ex-service high-pressure blade TBCs," *Surf. Coatings Technol.*, **208** 39–45 (2012).

[15]    J.L. Easterly and M. Burnham, "Overview of biomass and waste fuel resources for power production," *Biomass and Bioenergy*, **10** [2–3] 79–92 (1996).

[16]    P. MOHAN, "Environmental Degradation of Oxidation Resistant and Thermal Barrier Coatings for Fuel-Flexible Gas Turbine;" University of Central Florida, 2010.

[17]    M.S. Danigole and L. Col, "BIOFUELS, An Alternative to US Air Force Petroleum Fuel Dependency," *Occas. Pap. No. 62*, (n.d.).

[18]     a D. Foster, "Fuels Flexibility in Heavy-Duty Gas Turbines," *Fuel*, (1961).

[19]    H.T. Corrosion, "Hot Corrosion in Gas Turbines," *High Temp. Corros. Mater. Appl.*, 249–258 (2007).

[20]    A. American and N. Standard, "Standard Specification for Gas Turbine Fuel Oils 1," *Methods*, **05** 1–7 (2003).

[21]  G.E. Company, "Specification for Fuel Gases for Combustion in Heavy-Duty Gas Turbines," *Methods*, [April] (2007).

[22]  S. Krämer, J. Yang, C.G. Levi, and C.A. Johnson, "Thermochemical Interaction of Thermal Barrier Coatings with Molten CaO–MgO–Al2O3–SiO2(CMAS) Deposits," **3175** 3167–3175 (2006).

[23]  R.E. Collins, *Flow of fluids through porous materials.* New York, Reinhold Pub. Corp., New York, 1961.

[24]  P.-G. De Gennes, F. Brochard-Wyart, D. Quéré, A. Reisinger, and B. Widom, "Capillarity and Wetting Phenomena: Drops, Bubbles, Pearls, Waves," *Phys. Today - PHYS TODAY*, **57** 66–67 (2004).

[25]  A. Kucuk, A.G. Clare, and L. Jones, "An estimation of the surface tension for silicate glass melt at 1400°C using statistical analysis.," *Glas. Technol.*, **40** [5] 149–153 (1999).

[26]  N.P. Bansal and S.R. Choi, "Properties of CMAS glass from desert sand," *Ceram. Int.*, **41** [3] 3901–3909 (2015).

[27]  H. Zhao, C.G. Levi, and H.N.G. Wadley, "Molten silicate interactions with thermal barrier coatings," *Surf. Coatings Technol.*, **251** 74–86 (2014).

[28]  C. Mercer, "A delamination mechanism for thermal barrier coatings subject to calcium – magnesium – alumino-silicate ( CMAS ) infiltration," **53** 1029–1039 (2005).

[29]  A.G. Evans and J.W. Hutchinson, "The mechanics of coating delamination in thermal gradients," *Surf. Coatings Technol.*, **201** [18] 7905–7916 (2007).

[30]  S. Krämer, S. Faulhaber, M. Chambers, D.R. Clarke, C.G. Levi, J.W. Hutchinson, and A.G. Evans, "Mechanisms of cracking and delamination within thick thermal barrier systems in the aero-engines subject to calcium-magnesium-alumino-silicate (CMAS) penetration," *Mater. Sci. Eng. A*, **490** [1–2] 26–35 (2008).

[31]  C.G. Levi, J.W. Hutchinson, M.-H. Vidal-Sétif, and C.A. Johnson, "Environmental degradation of thermal-barrier coatings by molten deposits," *MRS Bull.*, **37** [10] 932–941 (2012).

[32]  M.H. Vidal-Sétif, C. Rio, D. Boivin, and O. Lavigne, "Microstructural characterization of the interaction between 8YPSZ (EB-PVD) thermal barrier coatings and a synthetic CAS," *Surf. Coatings Technol.*, **239** [May] 41–48 (2014).

# 2. INSTRUMENTATION AND PROCEDURES

## 2.1  Oxy-acetylene ablation rig development

### 2.1.1  Design, assemblage, and calibration of ablation rig

Fig. 2.1 illustrates the design and construction of the ablative set up in compliance with ASTM E285-08 [1]. Capabilities include ablating samples up to 2200°C, indirect thermal gradient measurements across samples, and characterization of the combustion atmosphere.
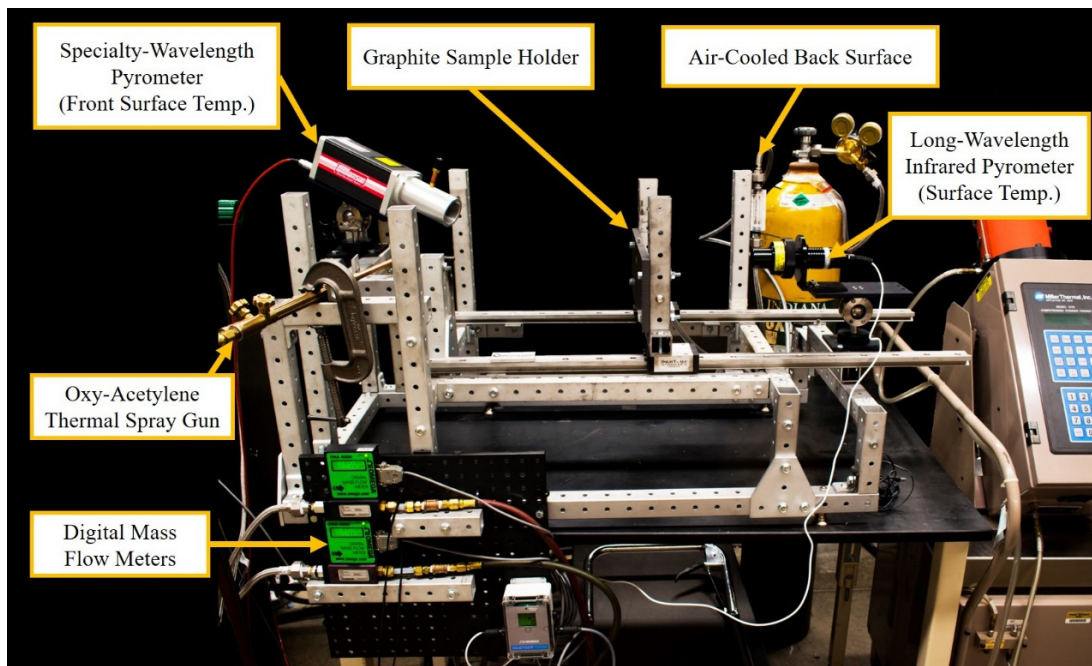


Fig. 2.1. Oxy-acetylene ablation rig summarizing the main components: Ablation torch, sample holder, indirect temperature measurement devices, and flow meters to characterize the combustion atmosphere.

Multi-layered systems temperature profiles constituting of ceramic coatings and metallic substrates are measured using two laser aiming pyrometers. A specialty wavelength (10.5 µm) pyrometer measures the ceramic coating temperature in a range of 500-1700°C (Williamson Co., Neustadt, Germany), while simultaneously a long-wavelength pyrometer (8–14 µm) measures the metallic substrate temperature in a range of 20-2500°C (OS555, Omega Engineering Inc., Stamford, USA). Data loggers and command modules record the pyrometers temperature readings with resolutions up to 0.1 seconds and ±2% accuracy.

The design of the sample holder allows fixing the position of the TBCs by pressing the substrate with a set screw and avoiding contact with the topcoat and bondcoat. Thermal expansion and sample fitting tolerances were considered according to ISO 286-2 (Figure 2.2) [2]. Due to its high melting temperature, relatively excellent resistance to ablation, and low coefficient of thermal expansion (CTE), graphite plates grade 2N (i.e., 99% pure graphite) were machined with the specifications for the sample holder [3]. A drawback of the graphite holder is the decomposition of the graphite above 600°C, and localized oxidation in the zones in direct contact with the flame. Due to degradation, the fixture was replaced every 2 hours of ablation.
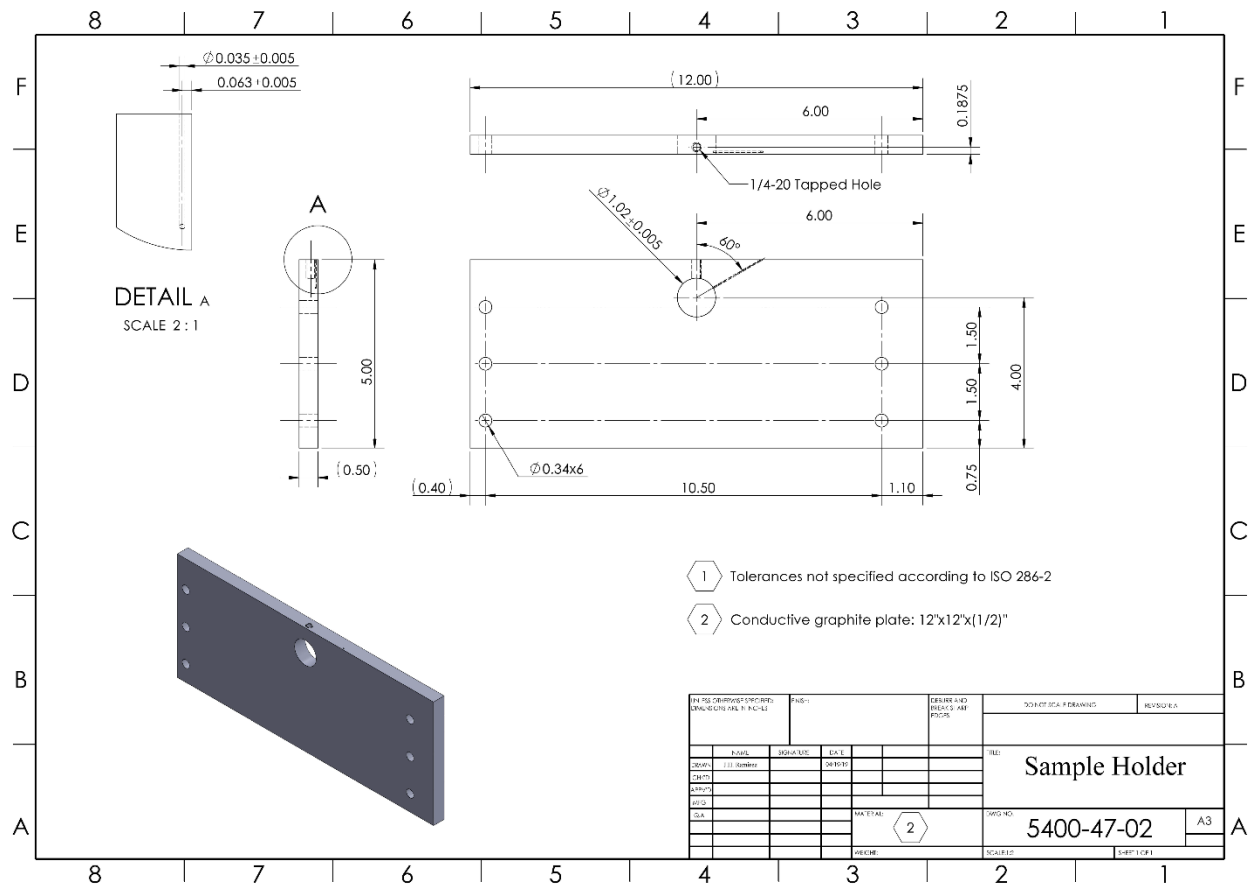


Fig. 2.2. Specifications of the graphite sample holder.

## 2.1.2 Heat flux characterization and thermal profile of ablated samples

The heat flux generated by the oxy-acetylene torch was characterized in function of the distance from the torch tip to the target surface with a circular-foil heat flux transducer TG-1000 (Vatell Corporation, VA, USA). The heat flux sensor was mounted in the graphite holder and cooled with water, making it appropriate for the ablation rig high heat-flux level and less sensitive to mounting conditions. Fig. 2.3 shows the heat flux when varying the distance between the torch tip and sensor.
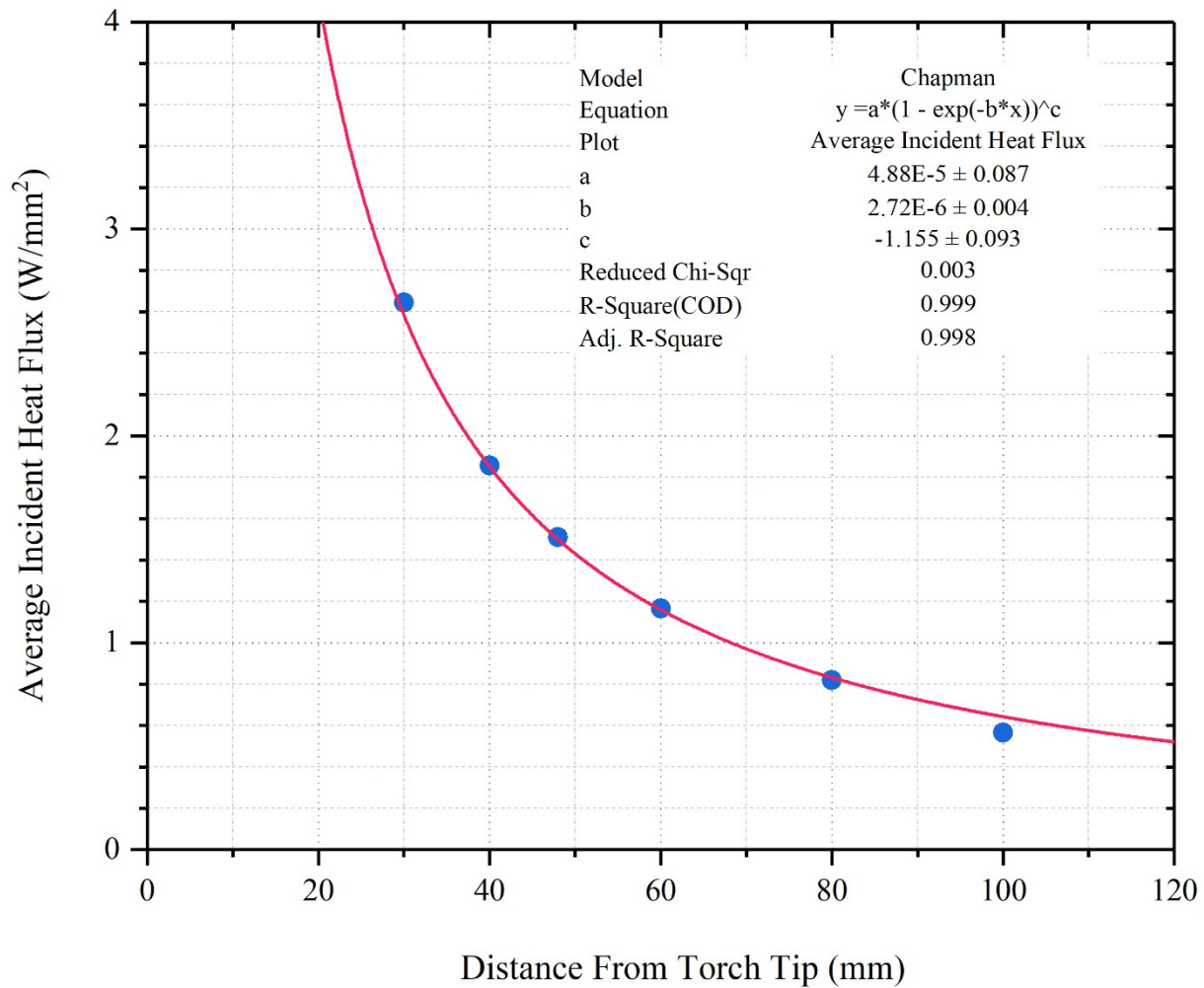


Fig. 2.3. Incident heat flux as a function of the distance between the target surface and the torch tip.

A preliminary test of the ablation rig was carried on APS TBCs specimens with a 750 μm thick YSZ topcoat, a 230 μm thick CoNiCrAlY bondcoat, and 6 mm thick Inconel 718 substrate. The pyrometers' emissivities were set to the values reported in the literature for YSZ and Inconel 718. Yang et al. [4] determined the emittance/absorptance spectra of YSZ APS TBCs in function of the coating thickness and porosity. For the case of an APS TBC close to a porosity density of 20%, and at a wavelength of 10.5 μm, the emittance approaches an ideal black body (i.e., ε=1). For the case of Inconel 718 at temperatures higher than 1000°C, Pottlacher et al. [5] determined that the emissivity at long-wavelengths is about 0.55. Fig. 2.4 shows the topcoat and substrates surface temperature along with the calculated temperature gradient across the sample of a TBC ablated for 10 minutes with a heat flux of 1.1 W/mm$^2$.
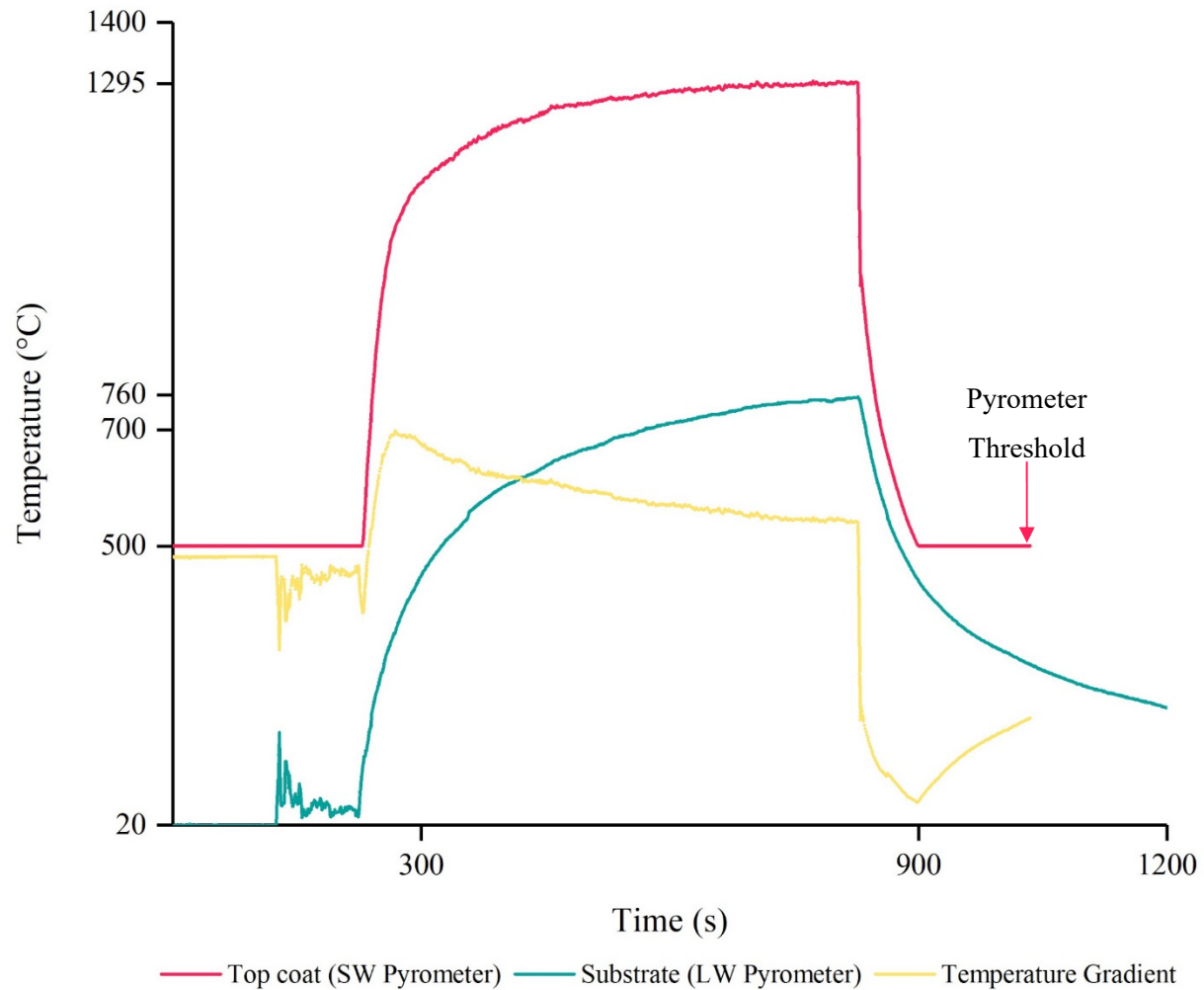


Fig. 2.4. Topcoat and substrate surface temperature measurements and calculated temperature gradient of an APS TBC ablated for 10 minutes.

### 2.1.3 Modeling and simulation considerations

A heat transfer model was used to validate the preliminary surface temperature measurements. Simulation of the thermal gradient across the TBC and the surface temperatures of the topcoat (ablated surface) and substrate (cooled by natural convection) was possible using ANSYS (Canonsburg, PA). A transient thermal study was used to model the ablated samples with a heat flux input of 1.1 W/mm². The thermal properties of the topcoat, bondcoat, and substrate were taken from the literature. Ekisehir et al. [6] determined that for a YSZ topcoat with a porosity density of 20%, the thermal conductivity and specific heat are described in function of temperature as in Eq. 2.1 and 2.2:

YSZ Thermal Conductivity (W/m°K):

$$k = 1.1397 + 0.0015T - 5x10^{-6}T^2 + 8x10^{-9}T^3 - 7x10^{-12}T^4 + 2x10^{-15}T^5 + 5x10^{-19}T^6 \qquad (2.1)$$

YSZ Specific Heat (J/kg°K):

$$C_p = 0.6516 - 0.0027T + 1.2357x10^{-5}T^2 - 2.4294x10^{-8}T^3 + 2.56x10^{-11}T^4 + 1.5041x10^{-14}T^5 + 4.6457x10^{-18}T^6 - 5.8813x10^{-22}T^7 \qquad (2.2)$$

The thermal conductivity and specific heat of the bondcoat and substrate were assumed to be constant [7–9]. Table 2.1 enlists the thermal properties of CoNiCrAlY and Inconel 718:

Table 2.1. Thermal properties of bondcoat and substrate alloys.

| Material | Specific heat (J/kg°K) | Thermal conductivity (W/m°K) |
|---|---|---|
| CoNiCrAlY | 473 | 4.3 |
| Inconel 718 | 652 | 15.05 |

Finally, the simulation model assumed isotropic thermal conductivity for all the TBC layers, standard temperature-dependent air convection coefficients for the sample, fixture surfaces in contact with stagnant air, and gray/diffuse surfaces for emissivity and absorptivity purposes (independent of wavelength).

Fig. 2.5 shows the maximum and minimum simulated surface temperatures at a time frame of 10 minutes of ablation with constant heat flux. As expected, the maximum temperature is observed on the surface of the ablated topcoat (~1270°C). The minimum temperature is displayed on the fixture heat dissipating areas.
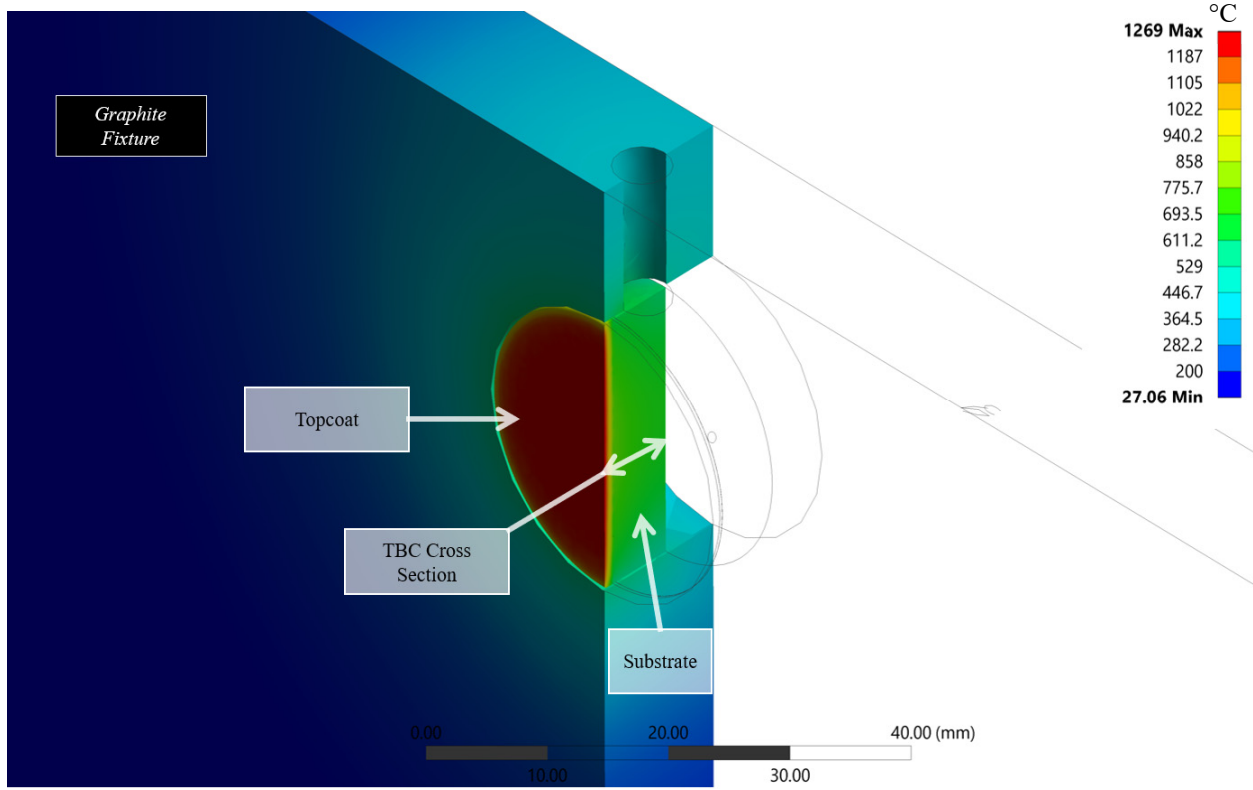


Fig. 2.5. Cross-section of TBC and fixture at a simulated time of 10 minutes of ablation with constant heat flux.

For a better analysis of the simulated model, the topcoat and substrate surface temperatures were analyzed independently. Fig. 2.6 shows the local minimum and maximum on each surface. The YSZ topcoat maximum temperature is ~1270°C at the center of the sample and ~1100°C on the perimeter. Noteworthy, the thermal gradient observed radially in the topcoat should be taken into consideration when doping with impurities since contaminants like CMAS have a melting point higher than 1200°C. Fig. 2.6 also illustrates the radial gradient in the substrate. The maximum simulated temperature in the substrate is ~700°C, which is far from the decomposition temperature reported for Inconel 718 [9].
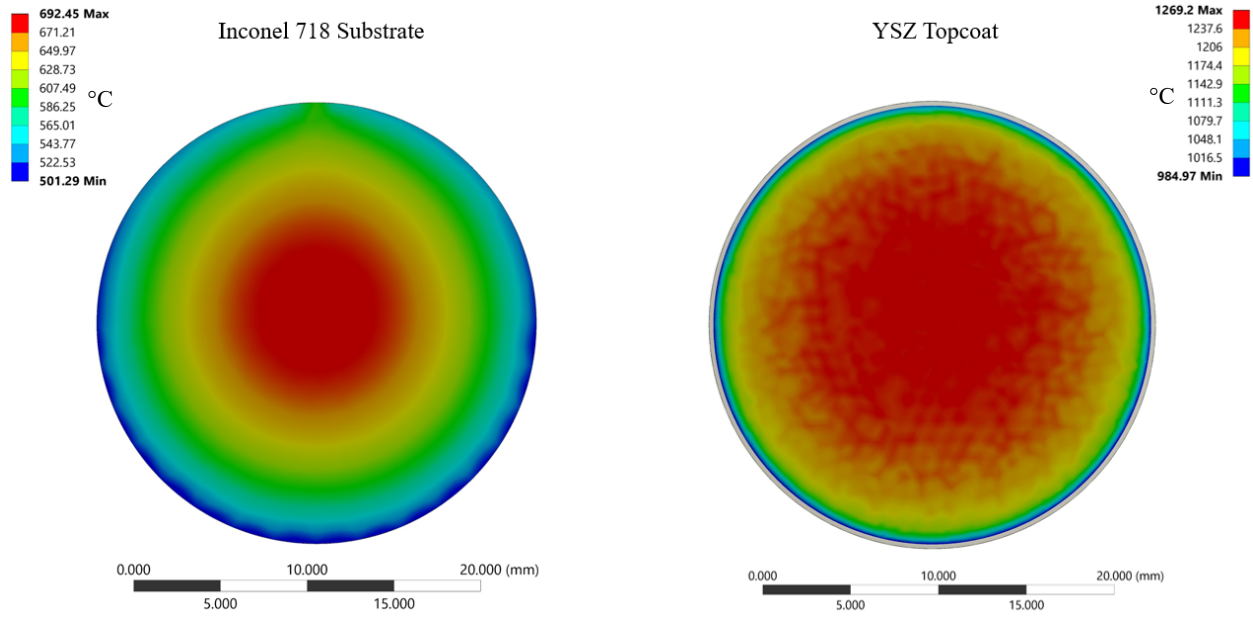
Fig. 2.6. A simulated thermal gradient of the substrate (side cooled by natural convection) and topcoat (ablated side) after 10 minutes of ablation with an input heat flux of 1.1 W/mm².

## 2.1.4    Simulation and experimental results comparison

Finally, a comparison of the simulated and experimental thermal profiles validated the instrumentation settings for ablating APS YSZ TBCs. Fig. 2.7 compares the surface temperatures of the topcoat, substrate, and the calculated thermal gradients. The simulated and experimental results comparison shows that for the case of the topcoat, the measurement error is around 2%. When analyzing the substrate, the error in the measurement is 34% at the highest difference with the simulation. The difference of the substrate temperature profiles is explained by the temperature dependence of the superalloy emissivity in the wavelength range of the pyrometer (i.e., 8-14 µm), introducing a lecture error as the temperature of the substrate increases. However, the pyrometers and simulation coincide that the topcoat surface temperature overpasses the melting temperature of CMAS and that the maximum substrate temperature is not high enough to induce a phase transformation of the substrate.
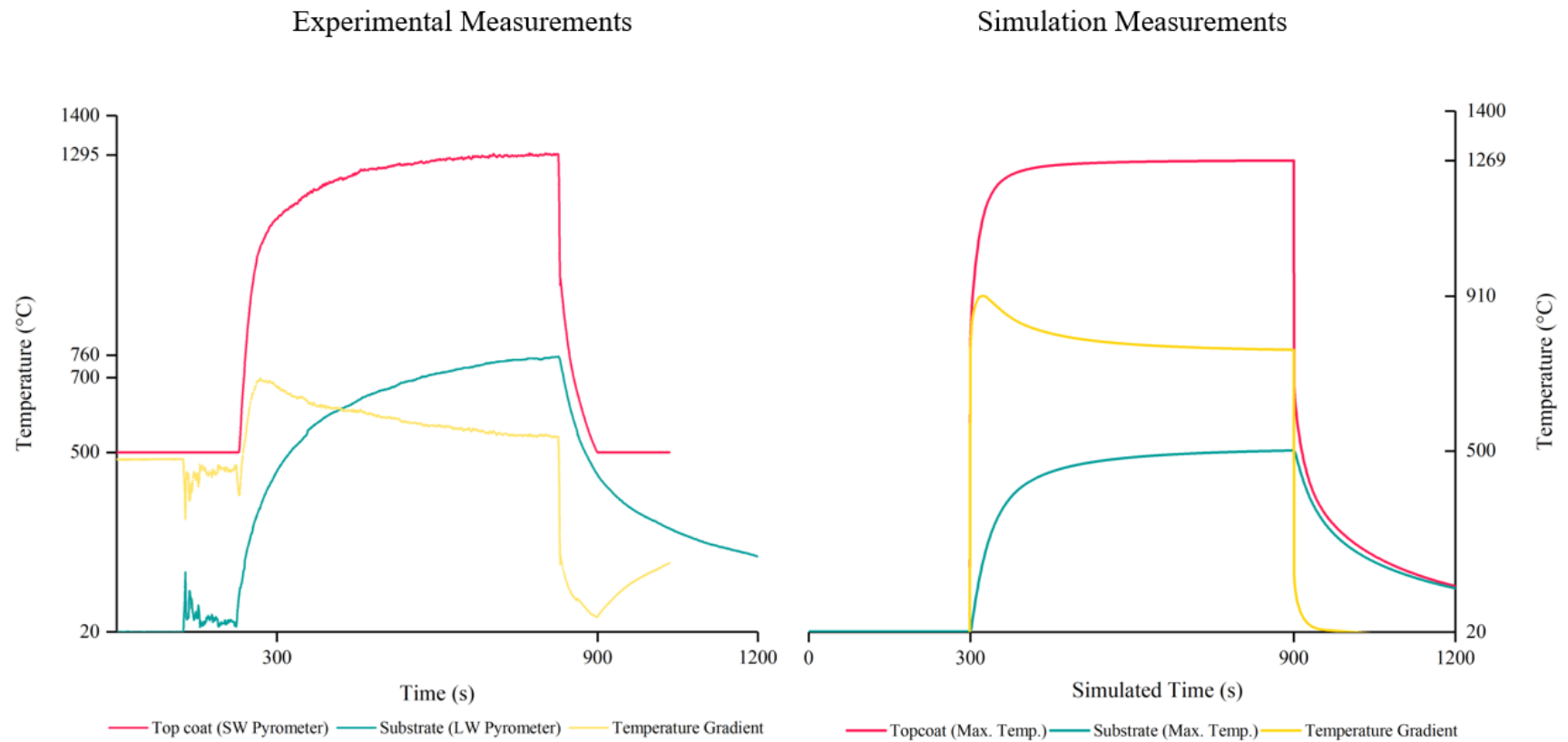
Fig. 2.7. Topcoat and bondcoat thermal profiles of experimental and simulated ablation with the same heat flux input.

## 2.2 Impurities deposition methodology

### 2.2.1 Formulation of impurity cocktails and biofuel impurities precursors

To deposit the impurities of interest on TBCs, we used impurity cocktails, solutions containing precursors of the oxides found in biofuel ash. The purpose of the impurity cocktails is to provide a method that offers the capability of controlling the composition and concentration of contaminants deposited on the topcoat surface while avoiding the erodent effect of particulate matter (PM) impacting the TBC. Impurity cocktails composition was tailored using oxide precursors diluted in ethanol or water. The final concentration of impurities was controlled by spraying the impurity cocktails on the TBCs. Table 2.2 enlists all the biofuel impurities reviewed in this work along with the used precursors for the impurity cocktails.

Table 2.2. List of biofuels impurities and precursors used in the impurity cocktails.

| Biofuel impurity | Precursor | Decomposition temperature | Decomposition reaction |
|---|---|---|---|
| $Al_2O_3$ | $Al(NO_3)_3$ | ~ 200°C | $4Al(NO_3)_3 \rightarrow 2Al_2O_3 + 12NO_2 + 3O_2$ |
| CaO | $Ca(NO_3)_2$ | ~500°C | $2Ca(NO_3)_2 \rightarrow 2CaO + 4NO_2 + O_2$ |
| $Fe_2O_3$ | $Fe_2O_3$ | - | - |
| $K_2O$ | $K_2CO_3$ | ~1200°C | $K_2CO_3 \rightarrow K_2O + CO_2$ |
| MgO | $Mg(NO_3)_2$ | ~300°C | $2Mg(NO_3)_2 \rightarrow 2MgO + 4NO_2 + O_2$ |
| $SiO_2$ | $Si(OC_2H_5)_4$ | ~600°C | $Si(OC_2H_5)_4 \rightarrow SiO_2 + 2C_2H_3OH + 2C_2H_4$ |
| $TiO_2$ | $TiO_2$ | - | - |
| ZnO | ZnO | - | - |

## 2.2.2  Impurity cocktail validation

XRD analysis was performed to validate the conversion of the impurity cocktail into the desired biofuel contaminants. An impurity cocktail formulated to achieve a CMAS reference composition (i.e., 33CaO-9MgO-13AlO$_{1.5}$-45SiO$_2$ mol%) [10] was compared with reports of CMAS phases in literature. Ten milliliters of an impurity cocktail calculated to have the CMAS reference composition was heated in a tube furnace with an air atmosphere at 800°C for 1 hour. The resulting powder from the dried solution was analyzed with a diffractometer using a copper source ($\lambda$=0.1544 nm) in a 2$\theta$ interval from 20 to 90° and a scan speed of 4 degrees per minute in steps of 0.02 degrees. Fig. 2.8a shows the resulting amorphous phase after 800°C. The amorphous phase indicates that there are no segregation products or precursors reacting previous the ablation cycle.

After repeating the heat treatment for the resulting with powder at 1000°C and 1200°C, the diffraction pattern exhibits peaks associated with the crystallization of Ca and Si base phases. Fig. 2.8b shows that the peaks in the XRD pattern match the crystallization of Akermanite, Anorthithe, and Wollastonite. The last is essential since akermanite and anorthite are phases commonly observed in crystallized CMAS on gas turbines components. Both the amorphous phase found above the decomposition temperature of the CMAS precursors, and the crystallized phases at 1200°C agreed that the impurity cocktail mimics the composition of CMAS encountered in flight conditions.
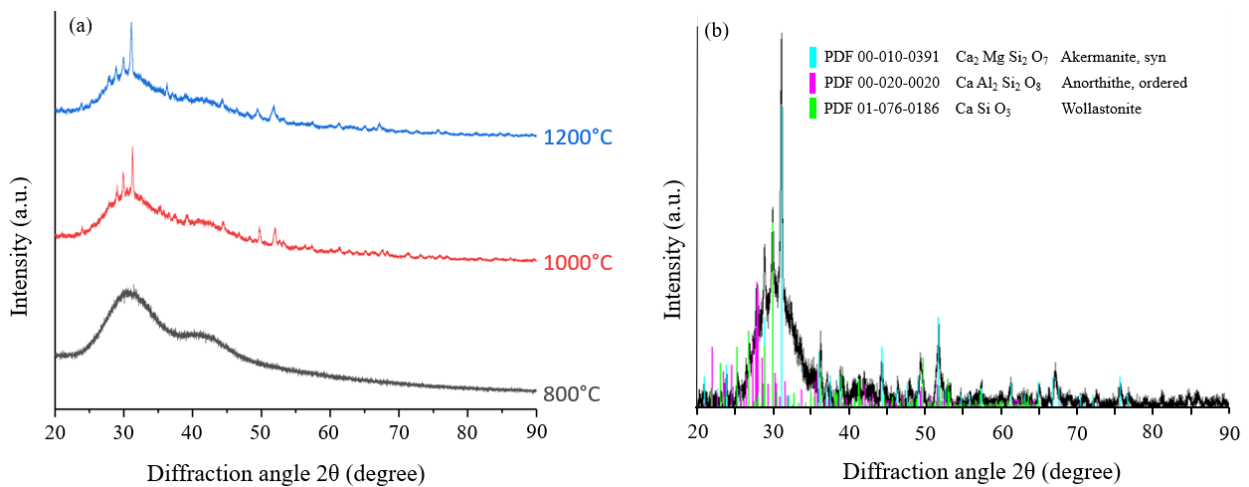


Fig. 2.8. XRD diffraction patterns of (a) the impurity cocktail after heat treatment at different temperatures during 1 hr and (b) analysis of the diffraction peaks crystallized at 1200°C.

### 2.2.3 Impurity cocktails deposition

Fig. 2.9 depicts the setup employed to deposit the impurity cocktails on the TBCs. A spray gun using air as a propellant atomized the impurity cocktail and deposited the contaminants over a heated the sample. A hot plate was used to keep the topcoat surface temperature above 200°C and allowing the solvent (i.e., ethanol or water) to evaporate at contact, leaving behind biofuels precursors on the surface of the TBC and avoiding pre-infiltration of the samples before thermal cycling. The impurity cocktail was sprayed at a distance of 20 cm from the tip of the spray gun to the sample surface to deposit the impurities on the entire topcoat. The coatings were sprayed with the impurity cocktails for 15 seconds and then allowed to reheat for another 15 seconds. Topcoats' temperature was monitored to never go down below 150°C with a thermocouple. Finally, the cross-section of a reference sample was analyzed to monitor the infiltration of the impurities deposition of the impurities. The concentration of the impurity cocktail infiltrating the sample was low enough that it was not possible to determine the depth of penetration of the solution with EDS analysis.
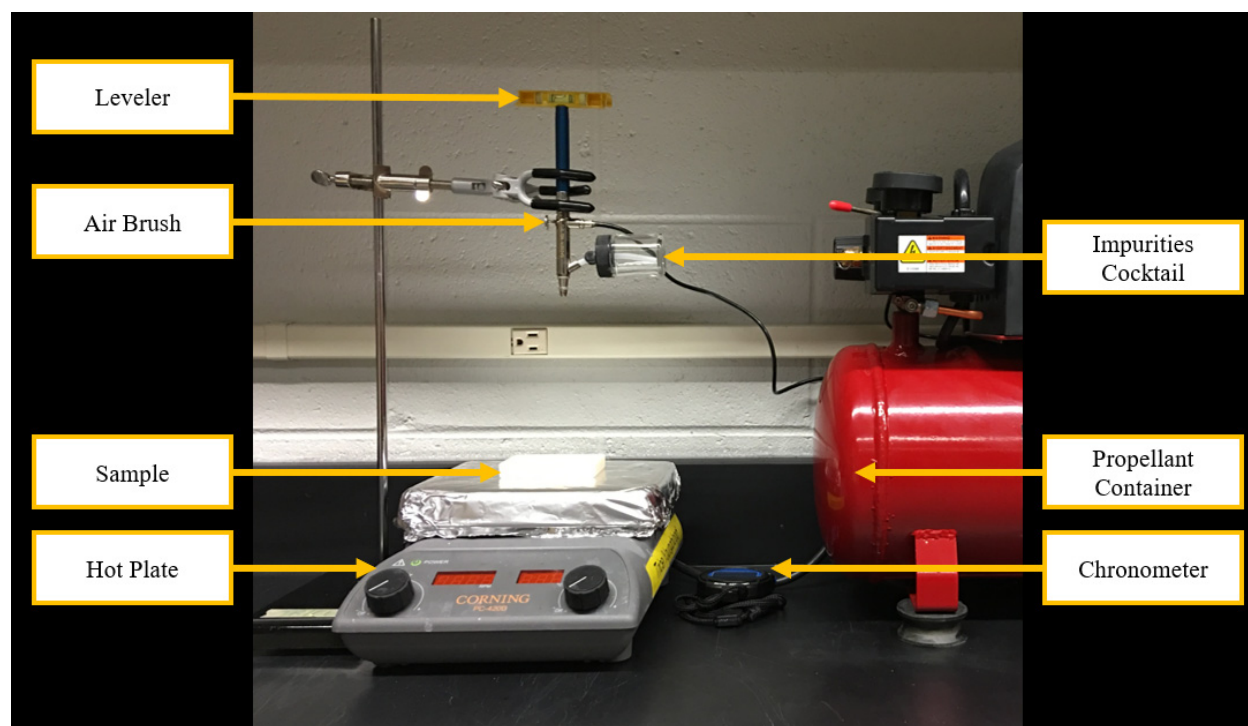


Fig. 2.9. Impurity cocktails deposition setup.

## 2.3    Methodology and preliminary test conclusions

The initial design of the ablation rig took into consideration ASTM standards aimed to test the durability of materials at high temperatures and the work of other burner rigs such as NASA and Jülich [11–13]. A preliminary test of APS TBCs ablated in the burner rig helped to determine the necessary heat flux conditions to reach thermal conditions similar to those encountered in a gas turbine. By using a mixture of acetylene and oxygen of 10:12 l/min, the measured heat flux was 1.1 W/mm$^2$ when placing the target sample at 55 mm from the torch tip. The ablated YSZ topcoats reached a surface temperature of ~1300°C  and a substrate temperature of ~760°C. Simulation of the ablated samples corroborated the thermal measurements of the YSZ topcoat. The modeling of the system also concluded that the real temperature of the substrate is ~150°C higher than the lecture of the pyrometer. The error observed in the readings of the substrate side is attributable to the change of emissivity due to the oxidation of the substrate and the dependence of the emissivity on the temperature of the superalloy. However, both experimental and simulated measurements agreed that the substrate temperatures did not overpass the decomposition temperature of Inconel 718 as to cause a phase transformation of the substrate.

Finally, the concept of formulating impurity cocktails containing the precursors of contaminants present in biofuels was validated. XRD analysis of dried and calcinated products of an impurity cocktail with a CMAS reference composition revealed that the precursors decompose and give place to the oxides present in CMAS. The peaks found in the XRD patterns revealed the presence of  Akermanite, Anorthithe, and Wollastonite, as in CMAS originated from flight conditions.

## 2.4    References

[1]     A. International, "Standard Test Method for Oxyacetylene Ablation Testing of Thermal Insulation," ASTM Int., 80 [C] 1–6 (2008).

[2]     Intrernational Standard, "Geometrical product specifications (GPS) — ISO code system for tolerances on linear sizes," 61010-1 © Iec2001, 2006 13 (2006).

[3]     A. Elements, "Product Datasheet: C-GR-02-PL," Datasheet, [March] 1–2 (2016).

[4]     G. Yang and C.Y. Zhao, "A Comparative Experimental Study on Radiative Properties of EB-PVD and Air Plasma Sprayed Thermal Barrier Coatings," J. Heat Transfer, 137 [9] 091024 (2015).

[5]     H. Hosaeus, A. Seifter, E. Kaschnitz, and G. Pottlacher, "Thermophysical properties of solid and liquid Inconel 718 alloys," High Temp. - High Press., 33 [4] 405–410 (2001).

[6]     Ö.A. Eskisehir and E.B. Istanbul, "Heat Transfer of Thermal Barrier Coatings On a Metal Substrate," [September 2015] (2013).

[7]     F. Fanicchia, D.A. Axinte, J. Kell, R. McIntyre, G. Brewster, and A.D. Norton, "Combustion Flame Spray of CoNiCrAlY & YSZ coatings," Surf. Coatings Technol., 315 [2] 546–557 (2017).

[8]     M. Akoshima, T. Tanaka, S. Endo, Tetsuya Baba, Y. Harada, Y. Kojima, A. Kawasaki, and F. Ono, "Thermal diffusivity measurement for thermal spray coating attached to the substrate using a laser flash method," Jpn. J. Appl. Phys., 50 [11 PART 2] 1–8 (2011).

[9]     J.N. Sweet, E.P. Roth, and M. M, "Thermal Conductivity of Inconel 718 and 304 Stainless Steel," 8 [5] 593–606 (1987).

[10]    M.P. Borom, C.A. Johnson, and L.A. Peluso, "Role of environment deposits and operating surface temperature in spallation of air plasma sprayed thermal barrier coatings," Surf. Coatings Technol., 86–87 116–126 (1996).

[11]    D.S. Fox, R. a. Miller, D. Zhu, M. Perez, M.D. Cuy, and R.C. Robinson, "Mach 0.3 Burner Rig Facility at the NASA Glenn Materials Research Laboratory," [March] 34 (2011).

[12]    R.A. Miller, M.A. Kuczmarski, and D. Zhu, Burner Rig With an Unattached Duct for Evaluating the Erosion Resistance of Thermal Barrier Coatings. 2011.

[13]    R. Vaben, F. Cernuschi, G. Rizzi, A. Scrivani, N. Markocsan, L. Ostergren, A. Kloosterman, R. Mevrel, et al., "Recent activities in the field of thermal barrier coatings including burner rig testing in the European Union.," Adv. Eng. Mater., 10 [10] 907–921 (2008).

# 3. APPLICATION OF BIOFUELS IMPURITIES AND EFFECT OF THE HOT CORROSION OF YTTRIA STABILIZED ZIRCONIA THERMAL BARRIER COATINGS

## 3.1    Abstract

The contaminants found in biofuels include alkali and alkaline metals along with sulfur, phosphorus, and silicon oxides. Furthermore, while calcium-magnesium-aluminum silicates (CMAS) are typically ingested as particulate in middle east theaters, the impurity list in biofuels includes the necessary elements to form CMAS without exposure to any environment. CMAS is particularly destructive for operating temperatures above its melting temperature (~1250℃), particularly affecting the lifetime of 7 wt.%$Y_2O_3$-$ZrO_2$ (YSZ) thermal barrier coatings (TBCs). In the work reported currently, solutions containing the individual and unreacted constituents of CMAS were prepared and sprayed onto either air plasma sprayed (APS) or electron beam physically deposited (EB-PVD) TBCs and subsequently subjected to dynamic heating up to 1400°C, simulating the deposit and thermal conditions of the biofuel impurities during combustion. Microstructure analysis revealed that the individual constituents of CMAS accelerated the degradation of the TBCs compared to the same samples heated without impurities.

## 3.2    Introduction

Gas turbines are an essential element of the modern world, being used to generate electrical power or thrust in commercial and military aircraft. To improve gas turbine efficiency, they have been operated at progressively higher temperatures, with ceramic thermal barrier coatings (TBCs) being employed in the combustion chamber to protect the underlying superalloy structure from temperature extremes. The processes used for depositing YSZ TBCs are typically either air plasma spray (APS) or electron beam physical vapor deposition (EB-PVD). APS coatings are typically used for large stationary components such as the combustion chamber walls, while EB-PVD

coatings are applied to small or rotating components such as blades and vanes. The most utilized TBC material is 7 wt.% $Y_2O_3$-$ZrO_2$ (YSZ) due to its low thermal conductivity and the relatively slow destabilization kinetics of the as-deposited $t'$-$ZrO_2$ phase to $c$-$ZrO_2$ and $t$-$ZrO_2$ phase (and ultimately $m$-$ZrO_2$) upon heating [1]. With the maximum operating temperature of gas turbines increasing to 1250°C and above, a new problem has emerged for TBCs that have been well documented over the last decade [2,3,4]. Calcium-magnesium-aluminum silicates or CMAS, a particulate common to the middle east regions or found in volcanic ash, can be pulled into a gas turbine. Depending on the composition of the particulate, it can melt and infiltrate into the TBC via the porous pathways in either the APS or EB-PVD microstructures. Upon cooling, the compliance difference between infiltrated and non-infiltrated coating regions causes residual stresses that can delaminate the infiltrated coating. Repeated heating/infiltration/cooling cycles can remove the entire TBC.

There is currently momentum to shift to the use of biofuels in gas turbines. For example, United Airlines flights between Los Angeles and San Francisco, have been using a blend of 70% Jet-A and 30% biofuel since 2016. Biofuels can be formed via numerous biomass processing approaches, using a multitude of different biomasses to include wheat, willow, and even olive waste [5]. It has been well established that contaminates found in fossil fuels such as Jet-A can be incorporated into TBCs, ultimately hastening their failure through a variety of different corroding mechanisms. Contaminants found in fossil fuels include S, V, Na, Ca, K, P, etc. [6] With the use of biofuels; however, a new group of contaminants must be considered. It has been determined that the number of impurities present in biofuels depends directly on the biomass source. The composition of impurities in the biomass source is highly variable due to its dependence on factors such as harvest season, the composition of the soil, and drying temperature [7]. This list includes Al, Ba, Ca, Fe, K, Mg, Na, P, and Si [8]. Inspection of this list reveals that those same elements found in particulate forms of CMAS are found as individual constituents in biofuels. Thus, a gas turbine operating with biofuels may be exposed to the constituents of CMAS without ever being operated in the middle east or volcanic ash environment. While extensive studies of the effect of fossil fuel impurities have been performed previously, [9] the effect of impurities and oxides of alkali and alkaline metals found in commercial and military biofuel blends (e.g., HEFA, FT-S8, SIP) is still unknown.

In the reported work, we have developed a methodology to incorporate the individual impurities found in biofuels into TBCs made either via APS or EB-PVD. The approach uses impurity "cocktails," solutions combining the impurities of interest that are subsequently sprayed on TBCs. Their effect on the microstructure is subsequently evaluated after heating/cooling in an ablation rig to temperatures of 1400°C. The goal is to validate a methodology robust enough to easily incorporate impurities that may arise from aviation fuels or external sources to ultimately understand the mechanisms of degradation when impurities are incorporated into a TBC. For such purposes in the presented case of study, a conventional 4-component CMAS composition was select.

### 3.3 Experimental methods

### 3.3.1 Formulation and application of the impurity cocktails

According to Drexler et al. [10], different methodologies are used for testing the degradation of TBCs under high temperatures and corrosive deposit conditions. When testing in a furnace, impurities of interest are commonly deposited over the sample surface in the form of a slurry. This approach for applying impurities is not suitable for burner rig testing since the deposited paste will flake off without infiltrating the sample. Instead, a more practical approach for burner rigs consists of spraying an impurity powder directly into the flame during the dynamic heating cycle. The challenges of this approach include monitoring the concentration of the deposited impurity species during the test and delineating between the thermo-chemical and thermo-mechanical effects on the sample microstructure. In this study, a low viscosity "impurity cocktail" was prepared, which contained a known concentration of impurities. This cocktail was subsequently sprayed on the sample surface at a concentration of 1 mg/cm$^2$ before ablation testing. However, as the coatings investigated presently were porous, the impurity cocktail infiltrates the microstructure to an unknown depth that was not characterized before ablation testing.

Nitrates of the alkaline metals, including $Ca(NO_3)_2$ (Sigma Aldrich), $Mg(NO_3)_2$ (Sigma Aldrich), and $Al(NO_3)_3$ (Sigma Aldrich) are soluble in ethanol. Using these nitrates, and the pre-ceramic polymer $Si(OC_2H_5)_4$ (Sigma Aldrich), an impurity cocktail with a composition in mole percent of

$33CaO-9MgO-6.5Al_2O_3-45SiO_2$ was formulated with the assumption that each nitrate or silicate solution would oxidize upon heating according to:

$$2Ca(NO_3)_2 \rightarrow 2CaO + 4NO_2 + O_2$$

$$2Mg(NO_3)_2 \rightarrow 2MgO + 4NO_2 + O_2$$

$$4Al(NO_3)_3 \rightarrow 2Al_2O_3 + 12NO_2 + 3O_2$$

$$Si(OC_2H_5)_4 \rightarrow SiO_2 + 2C_2H_3OH + 2C_2H_4$$
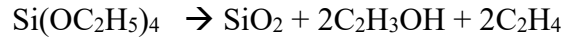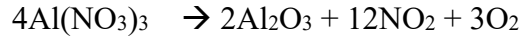
This composition of CMAS chosen was based on the average of deposits on aircraft turboshafts shrouds, as reported by Borom et al. [11] The conversion temperature of the reactions to produce the individual constituents of CMAS are all lower than 670°C. The individual constituents of CMAS were dissolved in ethanol to make a 10% concentration of the impurities in solution. In the as-mixed cocktail, there was no visual evidence of the formation of precipitates to suggest that the constituents reacted with one another or stratification of the added constituents suggesting they unmixed.

Before the deposition of the impurity cocktail, the coatings were heated up to 100°C by placing a hot plate in direct contact with the coating substrates. An airbrush kit, with the air pressure, held constant at 0.2 MPa, was used to spray the impurity cocktail. Impurity cocktails were sprayed on heated TBC/substrates in intervals of 5 seconds, followed by 3 seconds of no spray to facilitate ethanol solvent vaporization. The concentration of the impurity (not including the ethanol carrier) was constant at 1 $mg/cm^2$. Samples were dried at room temperature for 24 hours, and their weight monitored to verify that the ethanol had completely evaporated before the ablation cycle. The impurities were re-applied after each ablation cycle to a concentration of 1 $mg/cm^2$. The expected decomposed oxide products (CMAS) infiltrating the coatings in every spraying/ablation cycle was of a concentration of 0.26 $mg/cm^2$.

### 3.3.2 Specifications of TBCs evaluated.

Table 3.1 presents the APS and EV-PVD TBC coating systems (topcoat of 7 wt.% $Y_2O_3$-$ZrO_2$, and a bondcoat of either CoNiCrAlY or PtAl) evaluated in the current study.

Table 3.1. As-received specifications of APS and EB-PVD TBCs.

| Specification | APS | EB-PVD |
| --- | --- | --- |
| Geometry | Button Ø 25.4 mm | Button Ø 25.4 mm |
| Topcoat material | 7YSZ | 7YSZ |
| Topcoat thickness | 760 μm | 130 μm |
| Bond coat material | CoNiCrAlY | PtAl |
| Bond coat thickness | 230 μm | 50 μm |
| Substrate alloy | Inconel 718 | Rene N5 |
| Total thickness | 4 mm | 3.5 mm |

Each TBC system was applied to a 25 mm diameter superalloy substrate. The APS TBCs coatings were produced by Praxair Surface Technologies. The topcoat of YSZ was processed to have a dense vertically cracked (DVC) microstructure. The vertical cracks in the APS TBC are designed to simulate the columns observed in EB-PVD coatings. A CoNiCrAlY bondcoat was used for the APS TBCs, sprayed first on the Inconel 718. The EB-PVD TBC was supplied by GE, with a topcoat of YSZ, a bondcoat of PtAl, and a superalloy of Rene N5. Cross-sectional and surface views of each coating are shown in Fig. 3.1. The cross-sectional image of the APS TBC (Fig. 3.1a) shows vertical cracks, while the cross-sectional image of the EB-PVD coatings shows the expected columnar microstructure.
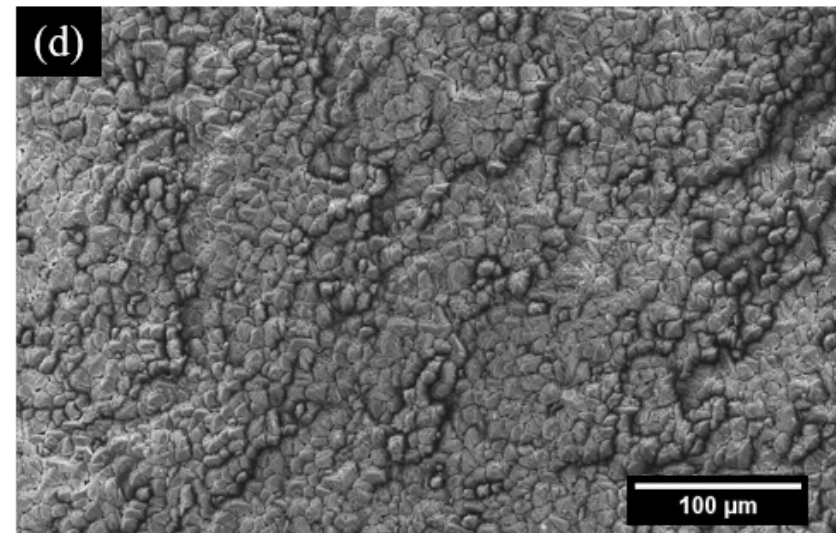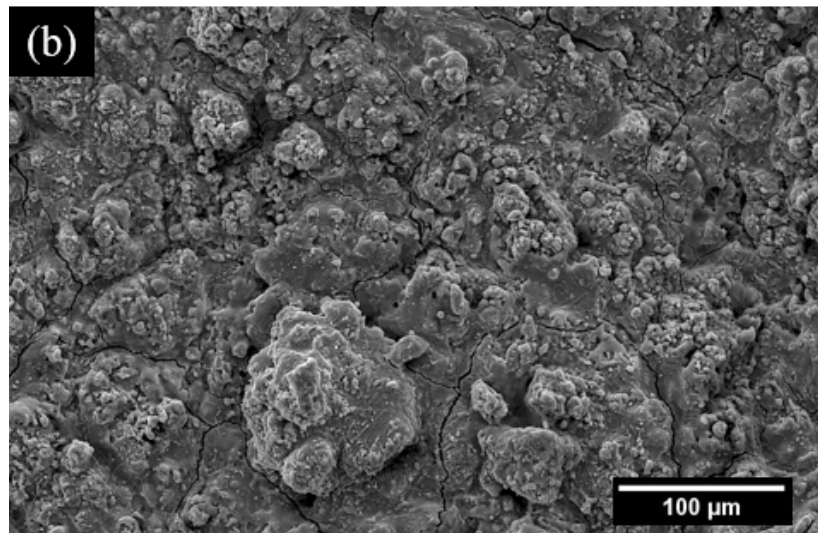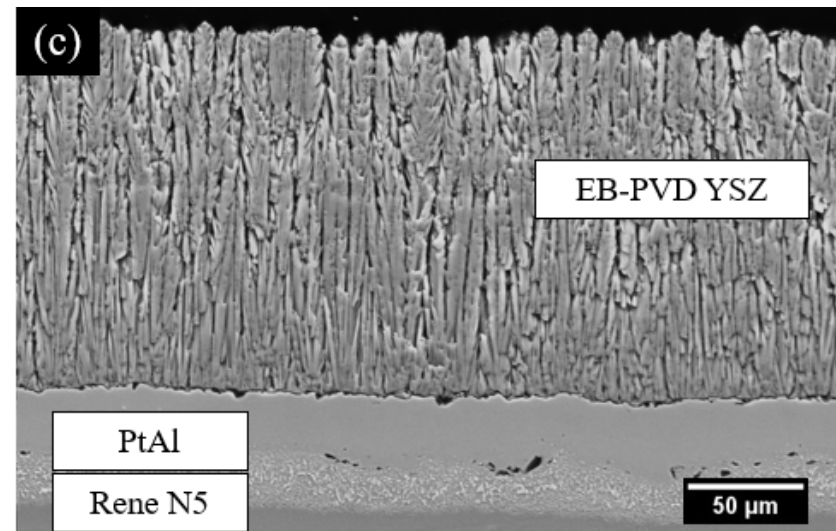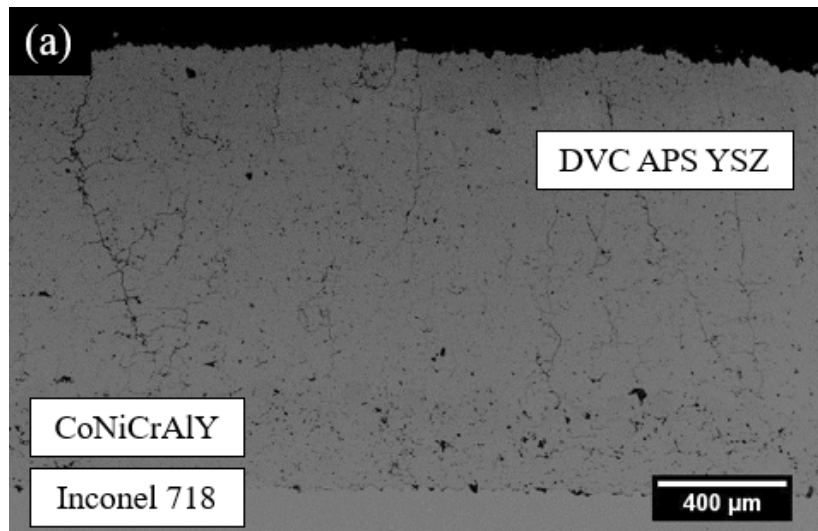
Fig. 3.1. SEM micrographs showing APS and EB-PVD TBCs in the as-received condition. Images (a) and (b) show the cross-section and top surface of the APS coatings studied. Images (c) and (d) show the cross-section and top surface of the EB-PVD coatings studied.

### 3.3.3 Ablation and characterization

In the current study, the deposition of the impurities on the TBCs was performed before ablation cycling, affording better control of the impurity composition, surface impurity concentration, and partial separation of the mechanical effect degradation (e.g., erosion) from the thermochemical degradation effect. The coatings were ablated with a 5-W Victor welding nozzle and acetylene to oxygen ratio of 10:12 liters per minute. Samples were positioned in the ablation rig using graphite plates that touched the top and bottom of the sample. This set-up allowed the entire front face of each sample to be exposed to the flame. The backside of the samples was free of obstructions to permit natural convection cooling of the substrate.

The temperature of the front face (i.e., the TBC surface temperature) was measured in intervals of 1s using an infrared pyrometer (Omega OS3753) with a near-infrared (NIR) wavelength of 1.55µm. As noted by Manara et al. [12], the low emissivity and high reflectivity of YSZ influence the infrared-optical characteristics of TBCs, affecting the precision of measurements taken by a pyrometer. Notably, it has been observed that the infra-red energy measured comes mostly from below the surface of the coating and not from the surface directly exposed to the flame. Thus, the actual surface temperature is likely higher than that measured and reported in the current data set.

The back-surface temperature was measured using a sheathed Type K thermocouple, with a single point in contact with the superalloy substrate. The thermocouple was positioned behind the region of the flame. Front face temperatures were maintained between 1400˚C to 1500˚C for APS and 1250˚C to 1300˚C for EB-PVD coatings. X-ray diffraction investigations in the $2\theta$ range of 72-76º revealed that EB-PVD coatings without added impurities were rapidly transforming the as-deposited $t'$-$ZrO_2$ to other zirconia phases at 1400ºC. Thus, a lower ablation temperature of 1250ºC-1300ºC was chosen. The APS coatings without added impurities remained $t'$-$ZrO_2$ after the 30-min ablation at 1400ºC; thus, an ablation temperature of 1400ºC was used for the APS coatings. The back temperature of the substrates never exceeded 1000˚C for either TBC, avoiding substrate phase changes, and melting temperatures reported for Inconel 718 and Rene N5 [13,14]. After each cycle, samples were allowed to cool down to room temperature by air convection. APS and EB-PVD samples were ablated in 10-minute cycles for a total ablation time of 30 and 20

minutes, respectively. The impurity was reapplied in a 1mg/cm$^2$ concentration after each ablation cycle.

As received and after ablation, X-Ray Diffraction (XRD) patterns were collected with a *Bruker D8 Focus* diffractometer. Samples were analyzed with an X-Ray copper source ($\lambda$=0.1544 nm), a 2$\theta$ interval between 20° to 90° and a scan speed of 3 degrees per minute in increments of 0.01 degrees per step. SEM micrographs of as-received coatings and after ablation were taken for comparison with the contaminated samples. Cross-sectional images of each coating were prepared by mounting the sample in epoxy and polishing down through 5µm using a diamond paste. For both cross-sectional and surface SEM analysis, a carbon coating was applied to the samples to avoid sample charging.

## 3.4    Results and discussion

### 3.4.1    Effect of thermal cycling on APS and EB-PVD TBCs (no impurities added)

Fig. 3.2 shows APS and EB-PVD TBC samples and a topological micrograph for each after being ablated for 30 minutes and 20 minutes, respectively. These samples did not have any impurity applied and, thus, they represent the baseline condition for each TBC type. Neither the APS or EB-PVD TBC samples showed significant degradation after being ablated. Cross-sections of each coating after ablation revealed the formation of small horizontal cracks in the APS sample due to thermal cycling (Fig. 3.2a), and microstructural densification in the EB-PVD TBC (Fig. 3.2c). A comparison of Fig. 3.1b with Fig. 3.2b reveals no difference in the APS coating surface before and after ablation. Similar observations were made for the EB-PVD coatings, as is seen in Fig. 3.1d, and Fig. 3.2d.
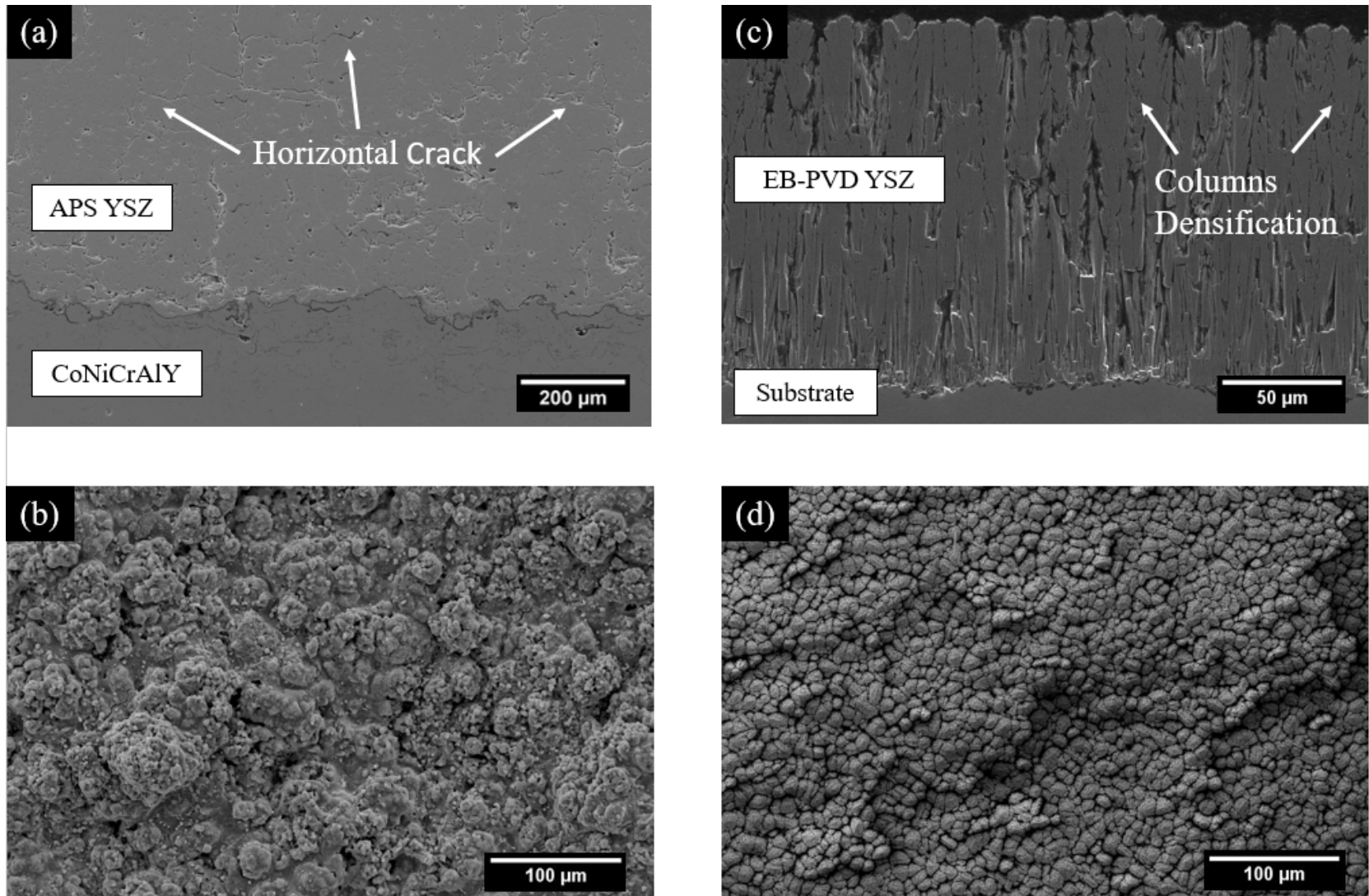
Fig. 3.2. APS TBC (a) cross-section and (b) surface after ablation for 30 minutes without impurities at 1400 °C and EB-PVD TBC (c) cross-section (d) and surface after ablation without impurities for 20 minutes at 1250 °C

### 3.4.2 The combined effect of thermal gradient cycling and CMAS impurities on APS and EB-PVD TBCs

*APS TBCs:*

Fig. 3.3 shows the changes in the APS TBC samples after each 10-minute cycle, with CMAS impurities added before each successive cycle. Fig. 3.3b, d, and f show the top surface of the coating. After the first thermal cycle of 10 minutes to 1400ºC, Figures 3.3a and b show no difference in comparison to the sample surface ablated with no impurities after 30 min at 1400ºC (Fig. 3.2a and b). After reapplication of the impurity cocktail and another 10 minutes of ablation, evidence of spallation and crack formation was apparent (Fig. 3.3c and d). Fig. 3.3d shows a region on the surface where part of the coating has delaminated. Finally, after reapplication of the impurity solution and a total of 30 minutes of ablation, large-scale spallation was visible in the sample (Fig. 3.3e and f). In contrast, the sample that was ablated with no impurities never exhibited coating spallation even after 30 minutes of ablation (Fig. 3.2b).
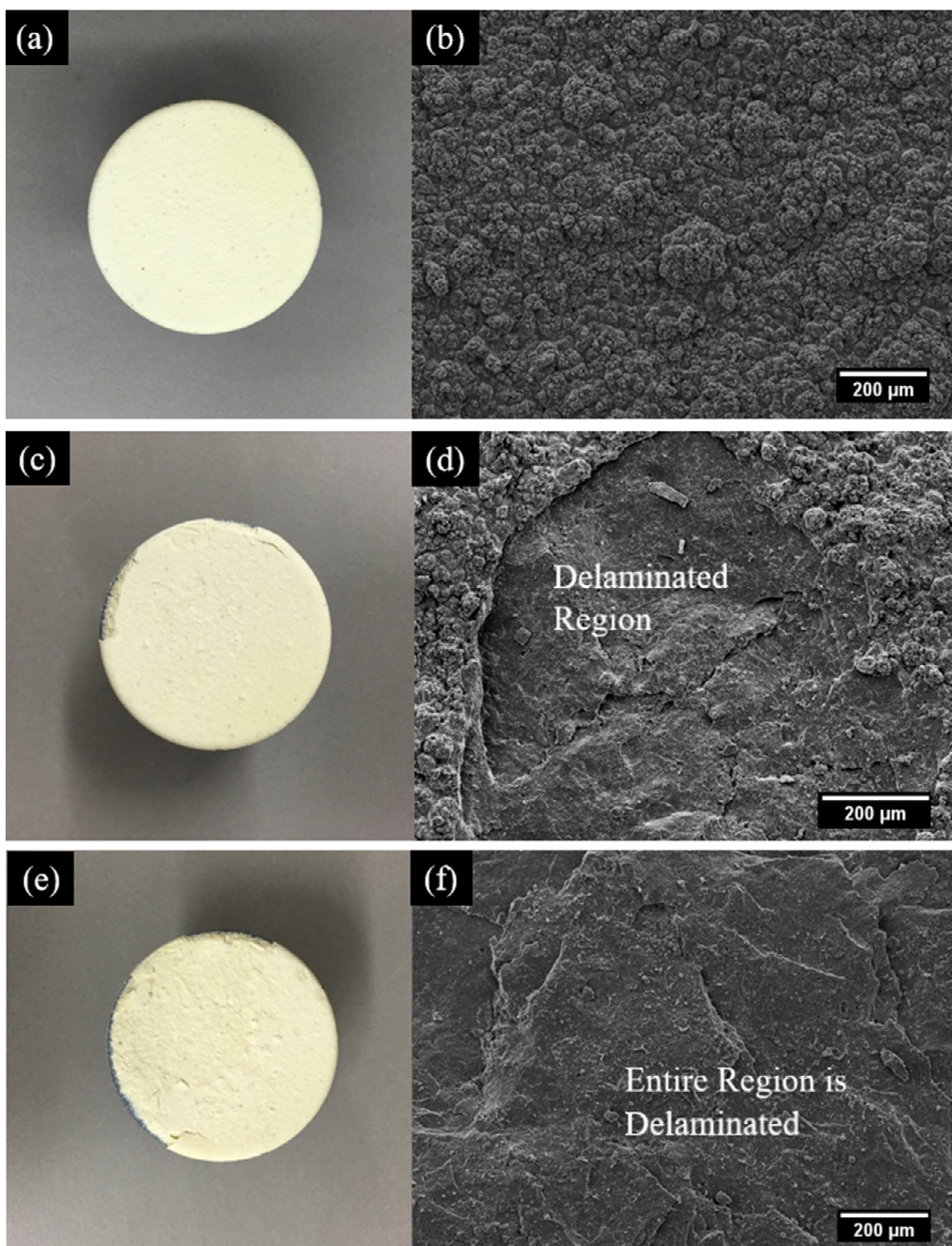
Fig. 3.3. APS sample with CMAS impurities, ablated for 10 minutes (a,b), 20 minutes (c,d) and 30 minutes (e,f) at 1400 °C.

The mechanism by which the APS TBC delaminates can be explained by analyzing the spallation debris. Fig. 4a shows a piece of debris in cross-section. There is a glassy phase that has infiltrated the coating, with a clear demarcation observed between the infiltrated and un-infiltrated parts of the coating. More detailed observations of debris, as in Fig.4b, show horizontal cracks right next to areas where the infiltrated impurities solidified, leading to the conclusion that the layer by layer delamination of the TBC is caused by partial infiltration, solidification, and horizontal crack formation in the TBC during every heating cycle.
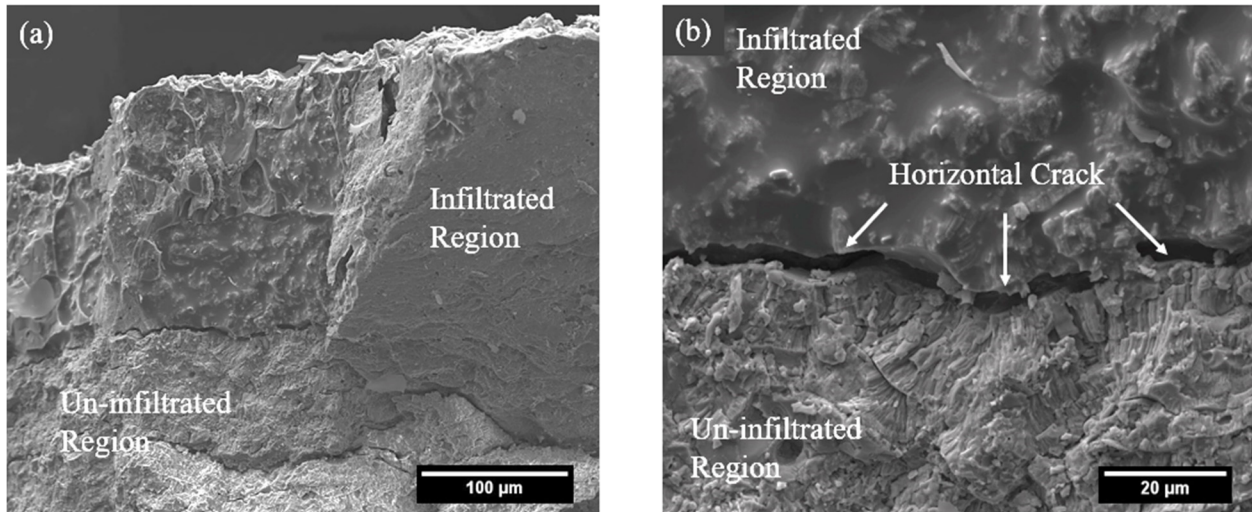


Fig. 3.4. SEM micrographs of a piece of delaminated APS coating following 30 minutes of ablation. Some regions were infiltrated by the reaction products. Horizontal cracks separate infiltrated from un-infiltrated regions in the coating.

Fig. 3.5a shows a polished cross-section of the APS TBC after 30 minutes of ablation time showing filled vertical cracks. Note that this sample had the impurity cocktail applied three times. The vertical crack in this micrograph has been filled with a secondary phase. Also indicated in Fig. 3.5a is a region analyzed using a qualitative energy dispersive spectroscopy (EDS) line scan. Fig. 3.5b shows a close-up of this region. The qualitative EDS revealed the presence of the added impurities within the vertical cracks of the TBC. The strong Si signal suggests the presence of a silica-containing material. Similarly, peaks associated with the presence of Al, Ca, and Mg were also noted in the vertical cracked regions suggesting that the Si, Al, Ca, and Mg have reacted together. Furthermore, zirconium was still observed in the vertically cracked regions, indicating that it was somewhat dissolved by the presence of the glassy product [15,16,17].
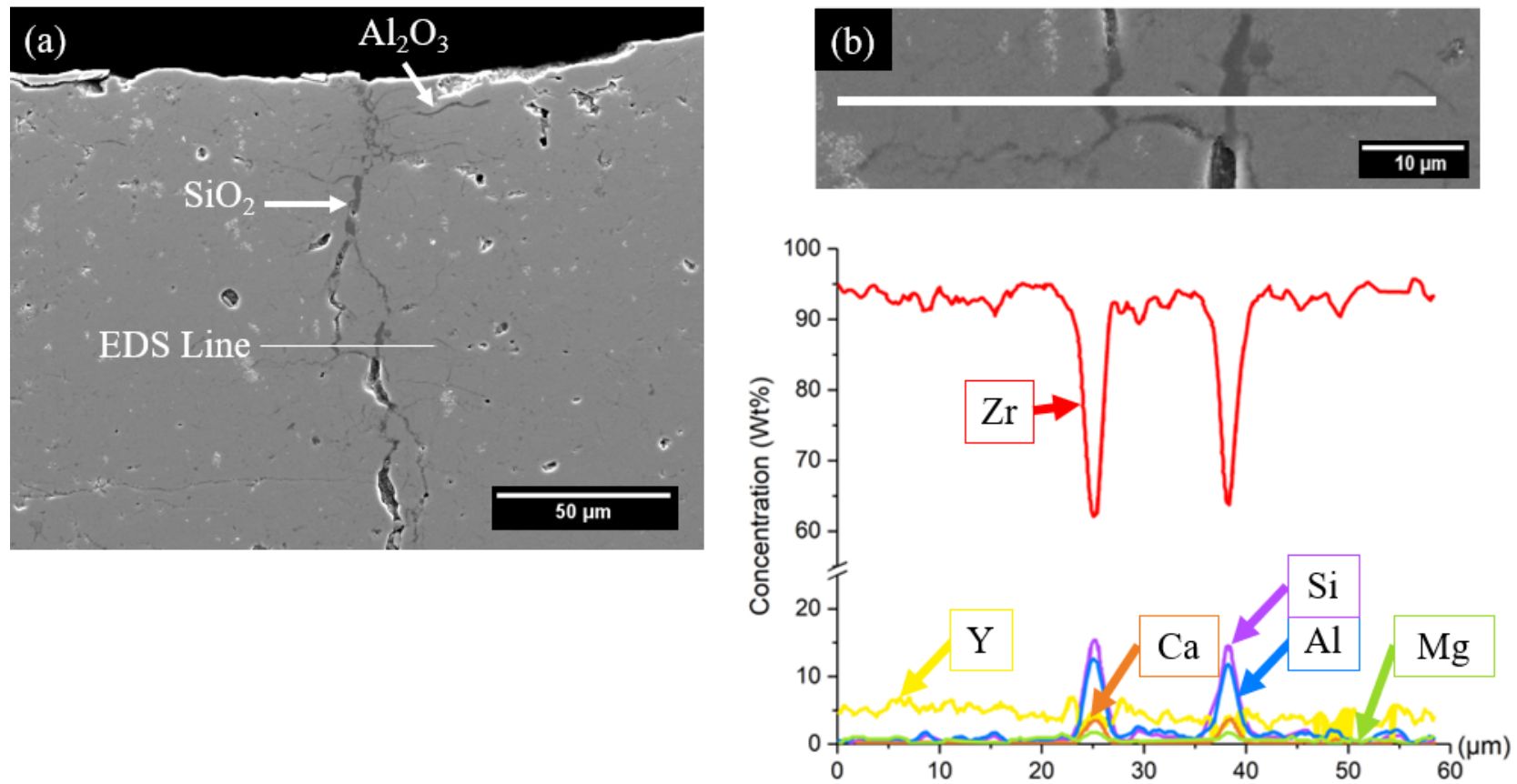
Fig. 3.5. a) SEM micrograph of an APS YSZ top coating after 30 minutes of ablation showing the infiltration of a glassy reaction product and b) enlarged area of this coating, with the corresponding EDS scan and the resulting elemental analysis.

### EB-PVD TBCs:

Fig. 3.6a-d shows the combined effects of thermal cycling and the addition of the impurity solution on EB-PVD TBCs. After the application of impurities and 10-minute ablation near 1300ºC, SEM micrographs revealed column separation in different regions (Fig. 3.6b) as compared to the EB-PVD sample heated to 1300ºC with no impurities (Fig. 3.2d). Reapplication of the impurity followed by another 10-minute ablation cycle caused no apparent delamination of the coating (Fig. 3.6c), in the surface, limited areas with reaction products were observed (Fig. 3.6d).
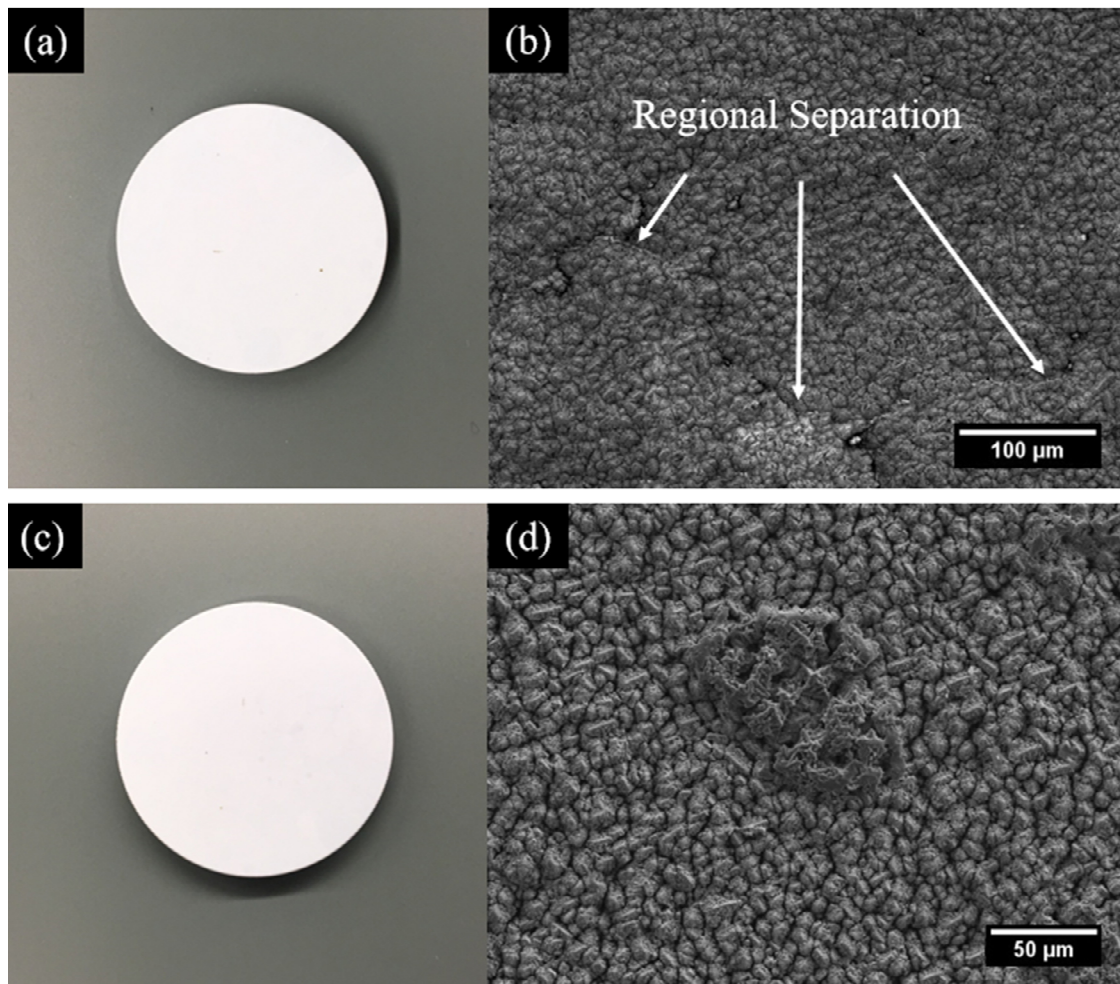


Fig. 3.6. EB-PVD sample with CMAS impurities ablated for 10 minutes  (a, b)  and 20 minutes (c, d).

Fig. 3.7a shows the polished cross-section of the EB-PVD TBC after 20 minutes of ablation and two applications of the impurity cocktail, along with a detailed view of the reaction products near the EB-PVD coating/bondcoat interface (Fig. 3.7b). Fig. 3.7c shows the elemental map for Si at the interface shown in Fig. 3.7b. Fig. 3.7a reveals regions of severe attack in the TBC/substrate interface, as well as void regions. A comparison of Fig. 3.7a to a coating ablated 20 min with no impurities (Fig.3.2c) reveals stark differences in the interface microstructure. Moreover, Fig. 3.7b, which was taken near the coating/bondcoat interface, along with the corresponding EDS map for Si, shows that significant concentrations of silica-containing phases are in this region. The location of the impurities strongly indicates full infiltration of the impurities through its entire thickness, reaching the denser bondcoat. As a reminder, the APS samples did not experience penetration of the modified silica phase through its thickness. This is in part due to the thicker APS topcoat, which suggests that a more significant amount of impurities is necessary to saturate the APS TBC microstructure (e.g., the open porosity) and totally infiltrate the coating. Furthermore, close inspection of Fig. 3.7b shows a horizontal crack developing in this silica-rich region, a precursor to the delamination of the coating.
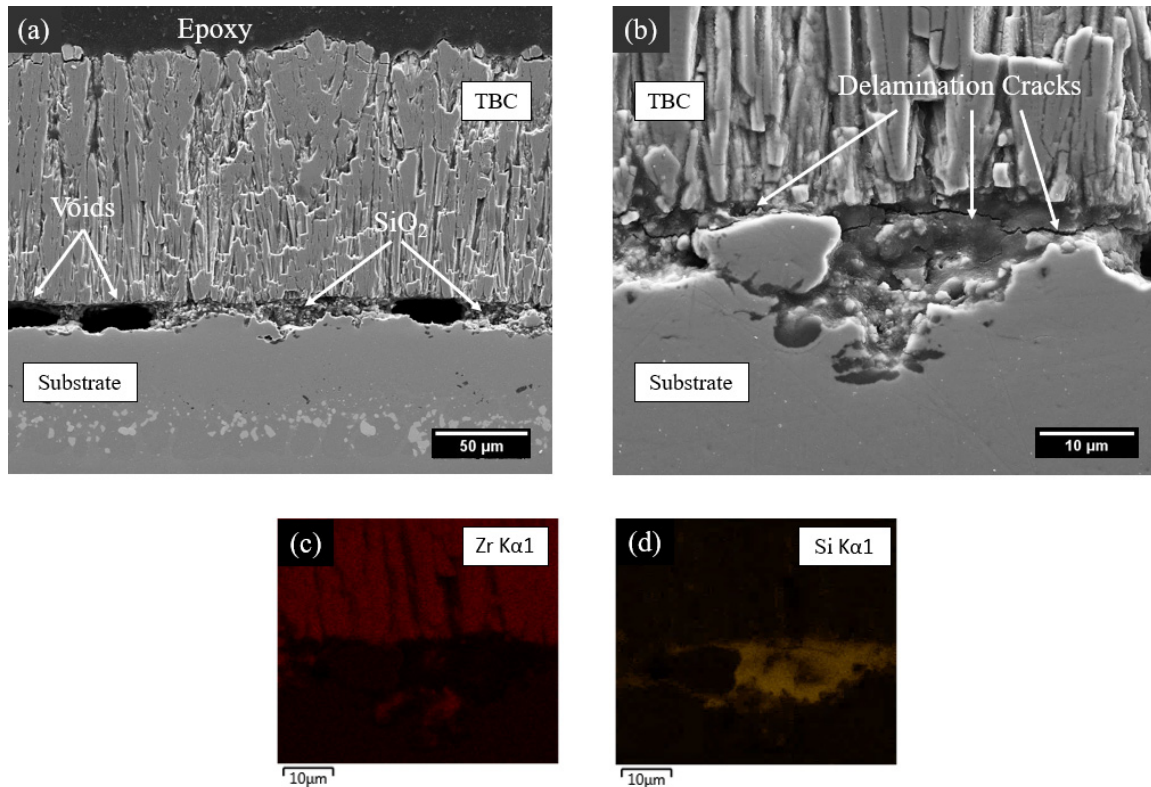


Fig. 3.7. EB-PVD TBC with impurity cocktail and  20 minutes of ablation. Cross-section (a) and close view of the infiltrated products (b) with the corresponding element maps (c and d) for Zr(Lα1) and Si(Kα1).

The location of the impurities products is consistent with the Zhao et al. [18] correlation of liquid permeability/intercolumnar pore fraction for the infiltration of particulate forms of CMAS in TBCs, with correlations made using similar thicknesses and sample compositions to those employed for this study. In their studies the columnar microstructure of the EB-PVD TBC favored the infiltration of the impurities, achieving full infiltration of the impurities (i.e., reaching the substrate) seconds after melting of the particulate form of CMAS. Thermochemical studies of molten CMAS with YSZ TBCs performed by Krämer et al. [19] observed that the full infiltration of molten CMAS in EB-PVD prepared coatings is accompanied by horizontal cracks at the topcoat/bondcoat interface, similar to the observations in Fig. 3.7b. Nevertheless, it is important to note that the infiltration of the impurity was not accompanied by a degradation of the columnar tips as suggested by previous literature. As noted by Vidal-Sétif et al. [20], tip degradation phenomena are present when a large volume of CMAS is present, opposite to the methodology proposed in this study where the amount of impurities is limited during each cycle.

### 3.5    Conclusions

A methodology to incorporate impurities found in aviation fuels and external contaminants has been developed by mixing alkali and alkaline nitrates and a silicon-containing preceramic polymer in an ethanol solution to form impurity cocktails. For this study, the impurity cocktail was designed to match the composition of the individual constituents found in particulate forms of CMAS. The solution was sprayed on both APS and EB-PVD TBCs, and its effect on the microstructure was evaluated after successive ablation cycles. The APS TBC exhibited extreme delamination, with the vertical cracks being filled by the modified silica glass, the oxidation product of the impurity cocktail. Each ablation cycle caused increased delamination. The oxidation product associated with the impurity cocktail interacted with the EB-PVD TBC differently than in the APS TBC, presumably due to differences in the thickness of the two different TBCs layers and the tortuosity of the pores. However, micrographs revealed nucleation and propagation of horizontal cracks in the oxide products for both coating types, features commonly observed as precursors for delamination.

## 3.6 Acknowledgments

## 3.7 References

[1]     R.A. Miller, "Thermal barrier coatings for aircraft engines: History and directions," *J. Therm. Spray Technol.*, 6 [1] 35–42 (1995).

[2]     S. Krämer, S. Faulhaber, M. Chambers, D.R. Clarke, C.G. Levi, J.W. Hutchinson, and A.G. Evans, "Mechanisms of cracking and delamination within thick thermal barrier systems in the aero-engines subject to calcium-magnesium-alumino-silicate (CMAS) penetration," *Mater. Sci. Eng. A*, **490** [1–2] 26–35 (2008).

[3]     N.P. Bansal and S.R. Choi, "Properties of CMAS glass from desert sand," *Ceram. Int.*, 41 [3] 3901–3909 (2015).

[4]     M.H. Vidal-Setif, N. Chellah, C. Rio, C. Sanchez, and O. Lavigne, "Calcium-magnesium-alumino-silicate (CMAS) degradation of EB-PVD thermal barrier coatings: Characterization of CMAS damage on ex-service high-pressure blade TBCs," *Surf. Coatings Technol.*, **208** 39–45 (2012).

[5]     S. V. Vassilev, D. Baxter, L.K. Andersen, and C.G. Vassileva, "An overview of the chemical composition of biomass," *Fuel*, **89** [5] 913–933 (2010).

[6]     Shih, Tom I.-P, and Vigor Yang. Turbine Aerodynamics, Heat Transfer, Materials, and Mechanics, 2014. Print.

[7]     Livingston W R (2009), 'Fouling corrosion and erosion', in Bridgwater A V, Hofbauer H, and van Loo S (eds), Thermal Biomass Conversion, CPL Press, pp. 157–176.

[8]     N.J. Simms, P.J. Kilgallon, and J.E. Oakey, "Degradation of heat exchanger materials under biomass co-firing conditions," *Mater. High Temp.*, 24 [4] 333–342 (2007).

[9]     P. Mohan, "Environmental Degradation of Oxidation Resistant and Thermal Barrier Coatings for Fuel-Flexible Gas Turbine;" M.S. University of Central Florida, 2010.

[10]    J.M. Drexler, A. Aygun, D. Li, R. Vaßen, T. Steinke, and N.P. Padture, "Thermal-gradient testing of thermal barrier coatings under simultaneous attack by molten glassy deposits and its mitigation," *Surf. Coatings Technol.*, **204** [16–17] 2683–2688 (2010).

[11]    M.P. Borom, C.A. Johnson, and L.A. Peluso, "Role of environment deposits and operating surface temperature in spallation of air plasma sprayed thermal barrier coatings," *Surf. Coatings Technol.*, 86–87 116–126 (1996).

[12]    J. Manara, M. Zipf, T. Stark, M. Arduini, H.P. Ebert, A. Tutschke, A. Hallam, J. Hanspal, *et al.*, "Long-wavelength infrared radiation thermometry for non-contact temperature measurements in gas turbines," *Infrared Phys. Technol.*, **80** 120–130 (2017).

[13]    G.A. Knorovsky, M.J. Cieslak, T.J. Headley, A.D. Romig, and W.F. Hammetter, "INCONEL 718: A solidification diagram," *Metall. Trans. A*, 20 [10] 2149–2158 (1989).

[14]     R.J.E. Glenny, J.E. Northwood, and A.B. Smith, "Materials for Gas Turbines," *Int. Mater. Rev.*, 20 [1] 1–28 (1975).

[15]    S. Krämer, J. Yang, C.G. Levi, and C.A. Johnson, "Thermochemical Interaction of Thermal Barrier Coatings with Molten CMAS," 3175 3167–317

[16]    F. Abe, S. Muneki, and K. Yagi, "Tetragonal to monoclinic transformation and microstructural evolution in ZrO2–9.7 mol% MgO during cyclic heating and cooling," *J. Mater. Sci.*, 32 [2] 513–522 (1997).

[17]    C.G. Levi, J.W. Hutchinson, M.-H. Vidal-Sétif, and C.A. Johnson, "Environmental degradation of thermal-barrier coatings by molten deposits," *MRS Bull.*, **37** [10] 932–941 (2012).

[18]    H. Zhao, C.G. Levi, and H.N.G. Wadley, "Molten silicate interactions with thermal barrier coatings," *Surf. Coatings Technol.*, **251** 74–86 (2014).

[19]    S. Krämer, J. Yang, C.G. Levi, and C.A. Johnson, "Thermochemical Interaction of Thermal Barrier Coatings with Molten CaO–MgO–Al2O3–SiO2(CMAS) Deposits," **3175** 3167–3175 (2006).

[20]    M.H. Vidal-Sétif, C. Rio, D. Boivin, and O. Lavigne, "Microstructural characterization of the interaction between 8YPSZ (EB-PVD) thermal barrier coatings and a synthetic CAS," *Surf. Coatings Technol.*, **239** [May] 41–48 (2014).

# 4. THERMOCHEMICAL INTERACTION OF BIOFUEL IMPURITIES WITH YTTRIA-STABILIZED ZIRCONIA THERMAL BARRIER COATINGS

*A version of this chapter has been submitted for publication in a peer-reviewed journal.*

## 4.1    Abstract

State of the art 7wt.%$Y_2O_3$-$ZrO_2$ (YSZ) thermal barrier coatings (TBCs) are used to protect superalloy components from the extreme heat evolved in the hot section of a gas turbine. Airborne contaminants interacting with TBCs originating from flight conditions, such as calcia (C) magnesia (M) alumina (A) silicate (S) or CMAS, are known to degrade the protective ceramic coatings and ultimately shorten in-service hours of jet engines. With the introduction of biofuels to the aviation industry, a new list of impurities arises based on the starting biomass and how it was harvested, opening the possibility to form deposits with compositions not studied previously such as S, CS, CA, CAS, and CMS. Because these impurities reside in the fuel, TBCs can be exposed to each constituent without flying in a specific environment. In this study, we applied combinations of precursors for C, M, A, and/or S, to the surface of a TBC with subsequent ablation to 1400°C to oxidize the precursor and react the constituents.  It was observed that the rate at which an APS TBC degrades varies depending on the impurity constituents. Moreover, microstructure and energy-dispersive X-ray spectroscopy (EDS) analysis revealed that the degradation mechanisms differed depending on the combinations of C-M-A-S constituents interacting with the TBC.

## 4.2    Introduction

Gas turbine development ranging in applications from aviation to power generation are expected to meet the highest standards for in-service lifetime, reliability, efficiency, and greenhouse emissions. A practical way to overcome the ever-growing demands is to reduce the fuel consumption of gas turbines; this is possible by increasing the operating temperature of components located in the combustion chamber and turbine sections of the engine (e.g., blades, vanes, combustor liner) [1–3]. The limiting factor of this approach is the melting temperature of superalloy components, which currently operate at the limit of their capabilities [4–6]. Thermal

barrier coatings (TBCs) emerged as a method to provide thermal insulation to the metallic elements, enabling jet engines to operate at temperatures above ~1250°C. Due to its unique thermo-mechanical properties described in detail elsewhere, the metastable *t'* phase of 7-8 wt.%$Y_2O_3$-$ZrO_2$ (YSZ) is the preferred ceramic phase for TBCs [7–9]. However, YSZ TBCs are susceptible to an accelerated degradation hastened by deposits of metallic and non-metallic elements arising from volcanic ash and airborne contaminants in the form of calcia (C) magnesia (M) alumina (A) and silicate (S) or CMAS [10, 11]. Several studies have correlated CMAS melting and coating infiltration behavior to the development of thermomechanical stresses that contribute to coating delamination [12, 13]. Additionally, the thermochemical interaction of YSZ with CMAS hastens the non-desirable phase transformation (t'-$ZrO_2$ → t-$ZrO_2$ + c-$ZrO_2$ → m- $ZrO_2$ + c-$ZrO_2$) of YSZ that promotes the coating degradation [14].

The limited oil reserves for fossil fuels distillation and a fluctuating supply cost, make aviation fossil fuels like Jet-A and Jet-B year by year less reliable. Alternative fuels are feasible options to replace fossil fuels since they are synthesized from biomass, making them a renewable and "environmentally friendly" source of energy [15]. However, concerns regarding biofuels include their effects on gas turbines components that were designed assuming that in-service conditions are set by the combustion of petroleum-distillate jet fuels [16].

In particular, ash deposition is a persistent problem in gas turbines burning biofuels that leads to a loss of efficiency. Cain et al. [17] identified that the particulate matter (PM) produced by burning biofuels varies in concentration, size, and composition depending on the nature of the biomass and process employed to synthesize the alternative fuels [18,19]. Kramer et al. [20] noted that the adhesion and infiltration of PM on ceramic coatings is dependent primarily on the ash composition that governs the melting point and viscosity of impurities. To avoid costly maintenance or adverse effects on engine performance and endurance, understanding the effect of the compounds found in biofuel PM that interacts with TBCs is necessary.

Fig. 4.1 summarizes the findings of two studies analyzing the composition of biofuel ash and as-synthesized biofuel from different biomass [21, 22]. The chart reveals that regardless of the biomass source, the same impurities appear in both liquid fuels and particle matter in the form of

ash. The list of impurities includes the phosphates and sulfates found in Jet-A, but also impurities with no precedent in aviation fuels such as the individual constituents of CMAS, to include C, M, A, and S in different combinations such as S only, CS, CA, CAS, CMS and CMAS [23–25]. With this possibility comes the need to investigate their role in the degradation of YSZ TBCs due to their presence. To simplify the magnitude of the problem, we limited the scope of this article to study the effect of combined and individual constituents of  CMAS, intending to identify the mechanisms by which a single or multiple C-M-A-S constituents hastens YSZ TBCs degradation.
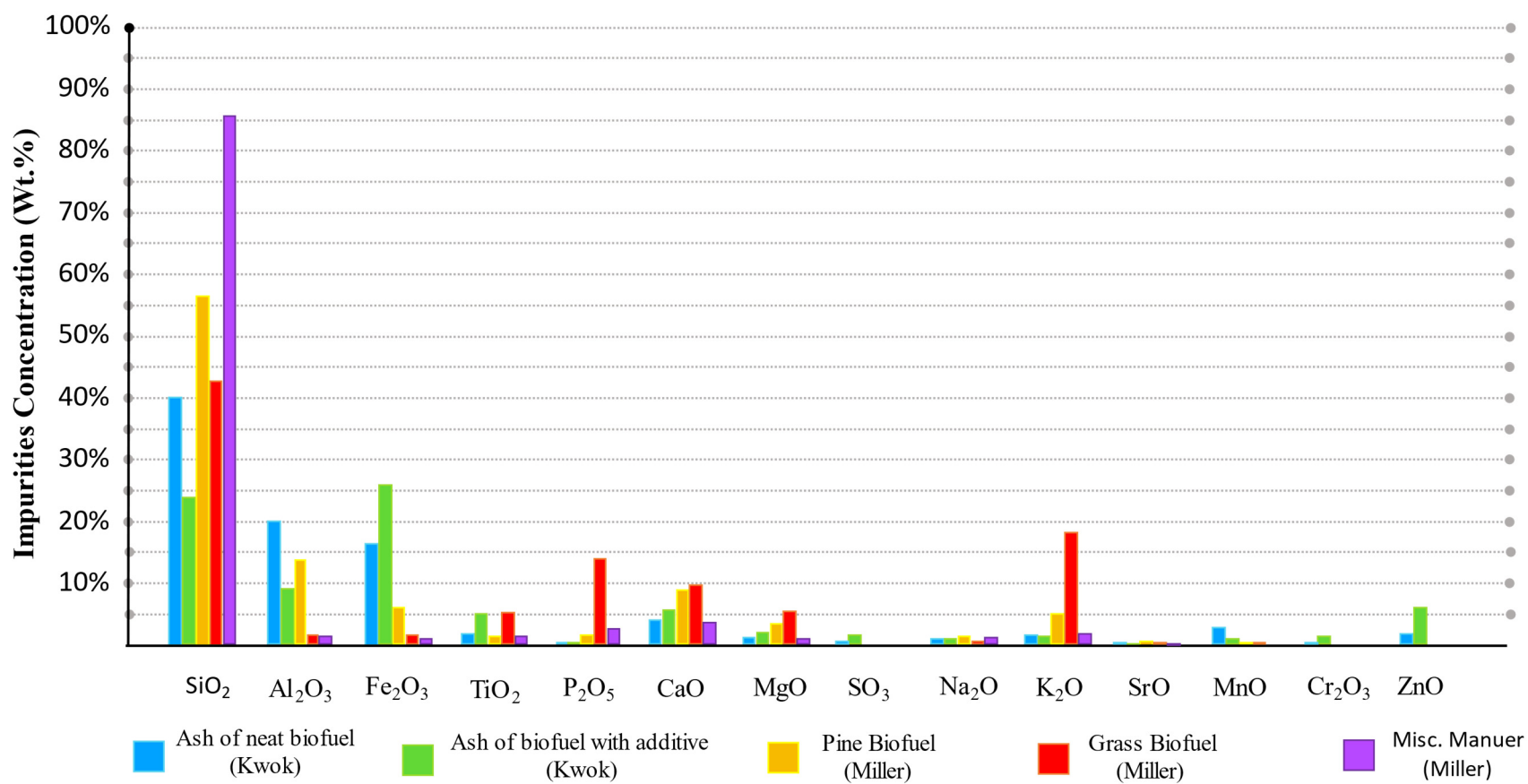
Fig. 4.1. Composition comparison of biofuel ash with liquid biofuel synthesized from different sources and a summary of the average concentration of CMAS constituents. Adapted from Q.S.M. Kwok (2004) and S.F. Miller (2007) [21, 22].

## 4.3 Experimental methods

### 4.3.1 Formulation of C-M-A-S derived impurity systems

Table 4.1 shows the five compositions derived from C-M-A-S constituents along with the reference C-M-A-S composition. Note that hyphens are used in the present study to indicate the impurities are applied to the surface as individual unreacted constituents.

Table 4.1. Sub-systems of impurities derived from alternative fuels contaminants and C-M-A-S reference composition.

| Solution No. | Model abbreviation | Model composition (mol %) | $T_m$ (°C) |
|---|---|---|---|
| 1 | S | $SiO_2$ | 1723 |
| 2 | C-S | $39CaO-61SiO_2$ | 1437 |
| 3 | C-A | $65CaO-35Al_2O_3$ | 1362 |
| 4 | C-A-S | $29CaO-8Al_2O_3-63SiO_2$ | <1200 |
| 5 | C-M-S | $30CaO-15MgO-55SiO_2$ | <1400 |
| 6 | C-M-A-S | $33CaO - 9MgO - 6.5Al_2O_3 - 45SiO_2$ | 1250 |

Fig. 4.1 shows that $SiO_2$ is the primary contaminant in biofuel ash, with an average concentration of ~50 wt.%. Thus, S alone was studied presently. Because of its abundance in biofuels, all impurity compositions studied included silica, except for C-A. The primary criteria used to select the combination and composition of impurities to deposit on the TBC was the melting point of the impurity compound. For the binary systems studied, to include C-S and C-A, eutectic compositions were chosen. In ternary systems, including C-A-S and C-M-S, we chose compositions with a melting point in between 1100 and 1300°C. Finally, a C-M-A-S reference composition, based on the average composition of deposits in turboshaft shrouds, $33CaO-9MgO-13AlO_{1.5}-45SiO_2$ mol%, was studied as the baseline for comparison [26]. For the analyzed compositions the impurity compounds were synthesized by mixing nitrates of calcium in the form

of Ca(NO$_3$)$_2$ (Sigma Aldrich), magnesium in the form of Mg(NO$_3$)$_2$ (Sigma Aldrich) or aluminum in the form of Al(NO$_3$)$_3$ (Sigma Aldrich) with tetraethyl orthosilicate Si(OC$_2$H$_5$)$_4$ (Sigma Aldrich) in ethanol (T$_{evap}$=70ºC) as an impurity cocktail. Heating this solution to 700°C oxidized the nitrates and precursors [27].

### 4.3.2  Application of impurities on TBCs

The degradation induced by C-M-A-S constituents was investigated on air plasma sprayed samples (APS) manufactured by Praxair Surface Technologies. Round buttons of Inconel 718, with a diameter of 25.4 mm and a thickness of 6 mm, were sprayed with a CoNiCrAlY bondcoat and a 7YSZ topcoat. The bondcoat had a total thickness of 230 μm sprayed in two layers. The first layer consisted of an 80μm-thick, highly dense structure with a smooth surface finish to improve the corrosion resistance of the bondcoat. The second layer was 150μm thick, characterized by a porous structure and a rough surface that improved adhesion with the topcoat. The YSZ topcoat was sprayed in a single layer with a nominal thickness between 700 and 750 μm; the resulting topcoat had a density of 92.5% and was designed to have a dense vertically cracked microstructure (DVC) to improve the strain tolerance of the TBC. The starting phase of the topcoat was t'-YSZ [28].

The impurities were deposited on the YSZ topcoat surface by spraying the impurity cocktail at a constant pressure of 0.2 MPa. Samples were heated up to 200°C before the spraying of the impurity cocktail to evaporate the ethanol quickly. The solutions were sprayed in intervals of 5 seconds and followed by 10 seconds of reheating to keep the surface temperature above 150°C. The infiltration of impurities after spraying was low enough that it was not possible to characterize the depth of infiltration of the impurity cocktail. The final concentration of the deposited impurities was 1±0.1 mg/cm$^2$. Samples were dried in air at room temperature for 24 hr before ablation testing.

### 4.3.3  TBCs thermal cycling

After spraying the impurities on the air plasma sprayed (APS) topcoats, the samples were ablated to test the durability of the TBCs when exposed to various combinations of C-M-A-S constituents and thermal conditions similar to gas turbines heating/cooling cycles. Thermal cycling was carried out employing an oxyacetylene ablation rig in compliance with ASTM E285-08. The oxyacetylene

heat source had a volume ratio of oxygen to acetylene of 1:2 to develop a natural flame condition [29]. The mass flow rates of unreacted oxygen and acetylene were set to 12 l/min and 10 l/min, respectively. The incident heat flux on the topcoat surface was calibrated with a flame calorimeter mounted in the same conditions used for the TBCs. The heat flux used to ablate the samples was 1.1 W/mm$^2$. YSZ topcoats surface temperature was monitored in intervals of one second using a two-color pyrometer OS3753 and corroborated with a second long-wavelength pyrometer with a wavelength ranging between 8-14μm. The ablation target temperature for the topcoat surface was 1300±50°C. Thermal cycles consisted of 10 minutes of ablation at "steady-state" temperature in between the target temperature range. Heating and cooling periods were not counted when timing the ablation cycles. The back-surface substrate (i.e., the Inconel 718) temperature was monitored so as not to surpass 1000ºC. The specimen holder consisted of graphite plates in contact with the TBC substrate but not with the topcoat and bondcoat. The back surface of the samples (substrate side) were free of obstruction to permit natural or forced air convection, maintaining the thermal gradient between the topcoat and substrate around 500±80°C during the ablation cycles. After each ablation cycle, samples were cooled down by natural convection, stored for 12 hrs, and then re-sprayed with the impurity cocktail. Five total ablation cycles were used for each impurity composition.

Surface SEM micrographs were collected for the as-received and after spray/ablation cycles. The electrical conductivity of the samples was enhanced with a carbon coating to avoid electrical charging. Cross-sectional views were obtained by mounting the samples in epoxy and auto polishing with diamond paste through 1μm. For the last case, a gold/palladium coating sputtered in argon gas was necessary for collecting the micrographs. The YSZ phase evolution was examined after each ablation cycle with a *Bruker D8 Focus* diffractometer, using a copper source (λ=0.1544 nm), a 2θ interval ranging between 20° to 90° and a scanning speed of 3 degrees per minute.

## 4.4 Results and discussion

### 4.4.1 Effect of impurity type and ablation cycles on microstructure

Fig. 4.2 shows the surface of the TBCs after exposing them to the different C-M-A-S impurities and the first ablation cycle to 1400°C. What appears to be crystalline reaction products were observed on the coatings exposed to C-S, C-A, C-A-S, C-M-S, and C-M-A-S impurities. The morphology of the reaction products for C-A-S, C-M-S, and C-M-A-S indicate that a glassy phase formed during the ablation cycle. The sample exposed to C-S exhibited solidified products on the topcoat surface. In the latter case, the complementary shape of the glassy impurities in the proximity of each other, suggests that the impurities cracked due to mechanical stress during solidification. Lastly, the sample exposed exclusively to silica, S, did not exhibit any new phases or signs of coating degradation.

All samples were ablated for up to four more thermal cycles, every 10 minutes in length, re-spraying the impurities on the TBC after each ablation cycle. Thermal cycling testing was stopped when each coating delaminated to the point where any part of the metal substrate was visible. As shown in Fig. 4.3, the number of cycles required for failure varied with impurity type. For the case of impurities containing MgO (e.g., C-M-S and C-M-A-S), glassy products penetrated the porous and micro cracked coating.  The damaged areas of the C-M-S and C-M-A-S infiltrated coatings show high porosity areas spalling in each thermal cycle. For the cases in which the impurities did not exhibit a continuous morphology (e.g., C-S and C-A), the excess of contaminants with a glassy appearance adhered to the coatings forming a physical interface with the TBCs. Even though no evidence of infiltration was found for the latter cases, the delaminated areas were in the vicinity of the impurities. The last is evidence that the thermal expansion coefficients mismatch between the crystallized impurities and the YSZ topcoat was the primary cause for topcoat spallation. The presence of solidified bubbles on the topcoat sprayed with C-A-S indicates that the impurity compound melted completely. The molten impurities covered all the APS surface morphology and penetrated the TBC through the sample microcracks and open porosity paths. The microstructure observed in the sample with C-A-S impurities is similar to the microstructure observed in the study of Vidal-Setif et al. [30] for the same system of impurities.
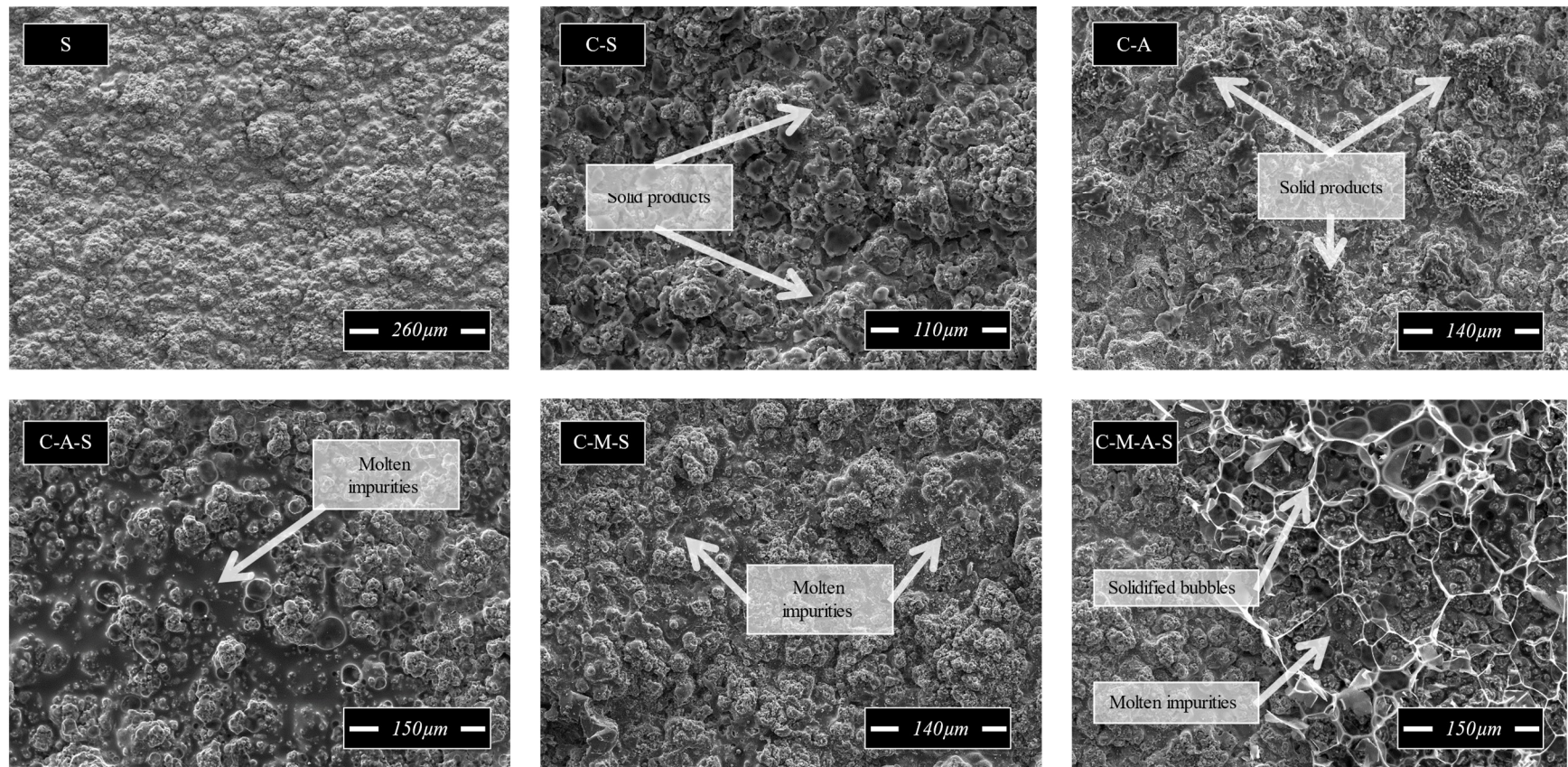
Fig. 4.2. Surface micrographs of APS samples after application of impurities and 10 minutes of ablation at 1400°C.
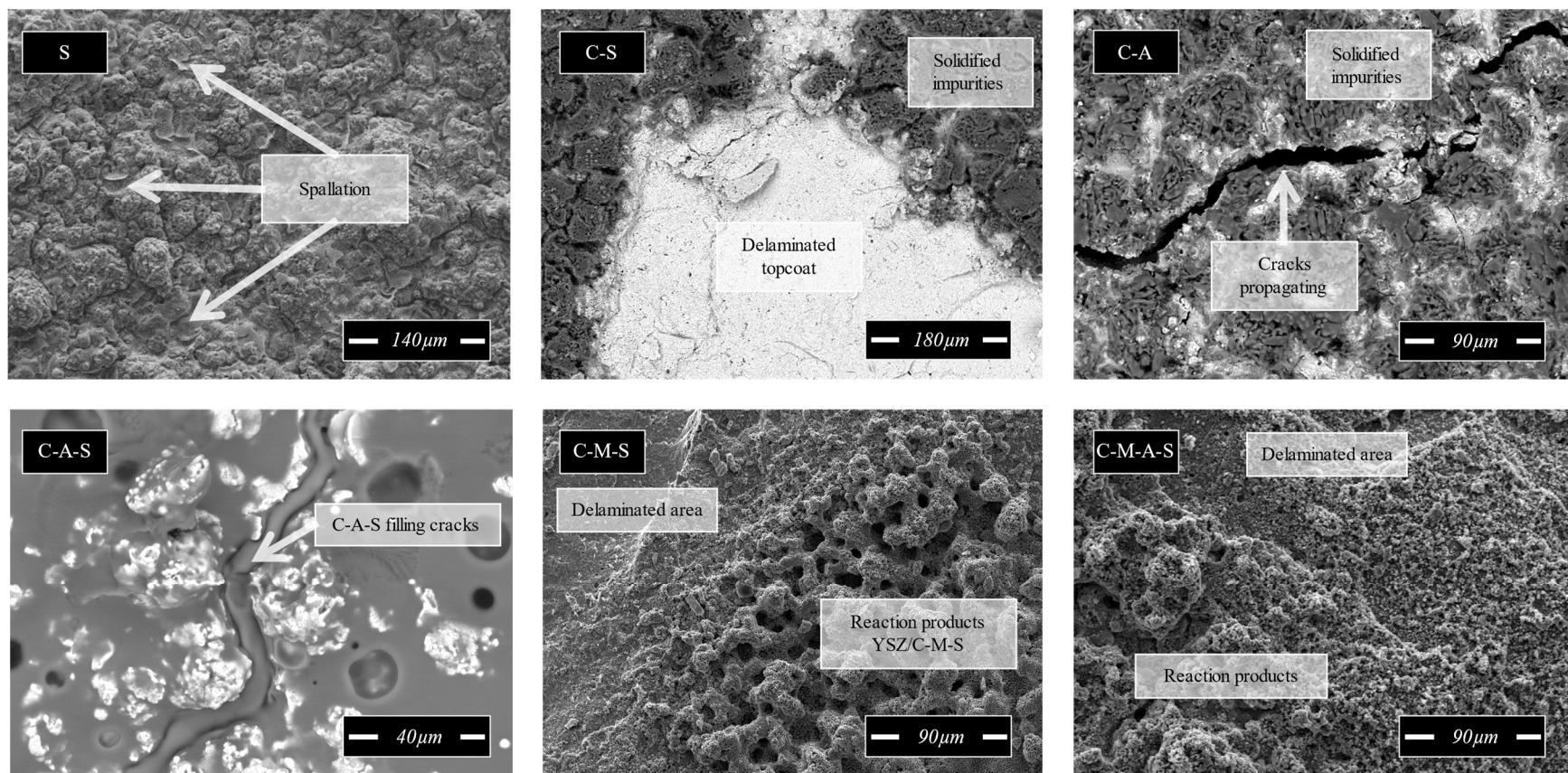
Fig. 4.3. TBC's surface micrographs showing the degradation mechanisms in which the coatings started to delaminate when exposed to impurities and thermally cycled at 1400°C.

### 4.4.2 YSZ and CMAS constituents thermochemical interaction

XRD was used to investigate the phase assemblage of each YSZ surface exposed to the six different impurity combinations after five total ablation cycles, with the impurity re-applied every 10 minutes. Since literature reports that the phase transformation of the metastable t'-YSZ to m-$ZrO_2$ is followed by the topcoat spallation, analysis on the XRD peaks in the range of $2\theta=20$ to $34°$ and $2\theta=72$ to $76°$ was used to determine if the peaks ascribed to the monoclinic $ZrO_2$ appeared in any of the samples [31–33]. Fig. 4.4 shows that the sample ablated for 50 minutes with no impurities exhibits t'-$ZrO_2$ / c-YSZ diffraction peaks consistent with what would be expected for an as-sprayed APS YSZ. TBCs exposed to impurities display diffraction patterns associated with m-$ZrO_2$ (Fig. 4.4b-g). The coatings sprayed with S, C-S, C-A, and -C-M-S developed peaks related to the crystallization of an impurity-based composition, with the calcium and silicon-based compounds exhibiting yttrium and zirconium content, respectively. For example, C-A was found to react with YSZ through the formation of $Si_2Y$. The crystallization of the silicon base product is accompanied by monoclinic zirconia peaks, suggesting the accelerated YSZ degradation through yttria depletion. Fujio et al. [34] reported similar decomposition mechanisms of t'-YSZ when doped with MgO, noteworthy, in this study the XRD observations reveal that the compounds enhancing the topcoat decomposition are Ca and Si crystallized phases. The higher intensity of peaks associated with monoclinic zirconia in samples exposed to contaminants that solidified primarily on the topcoat surface (i.e., S, C-S, C-A) suggests that the decomposition of the metastable t'-YSZ occurred in the proximity of the impurity crystal products.
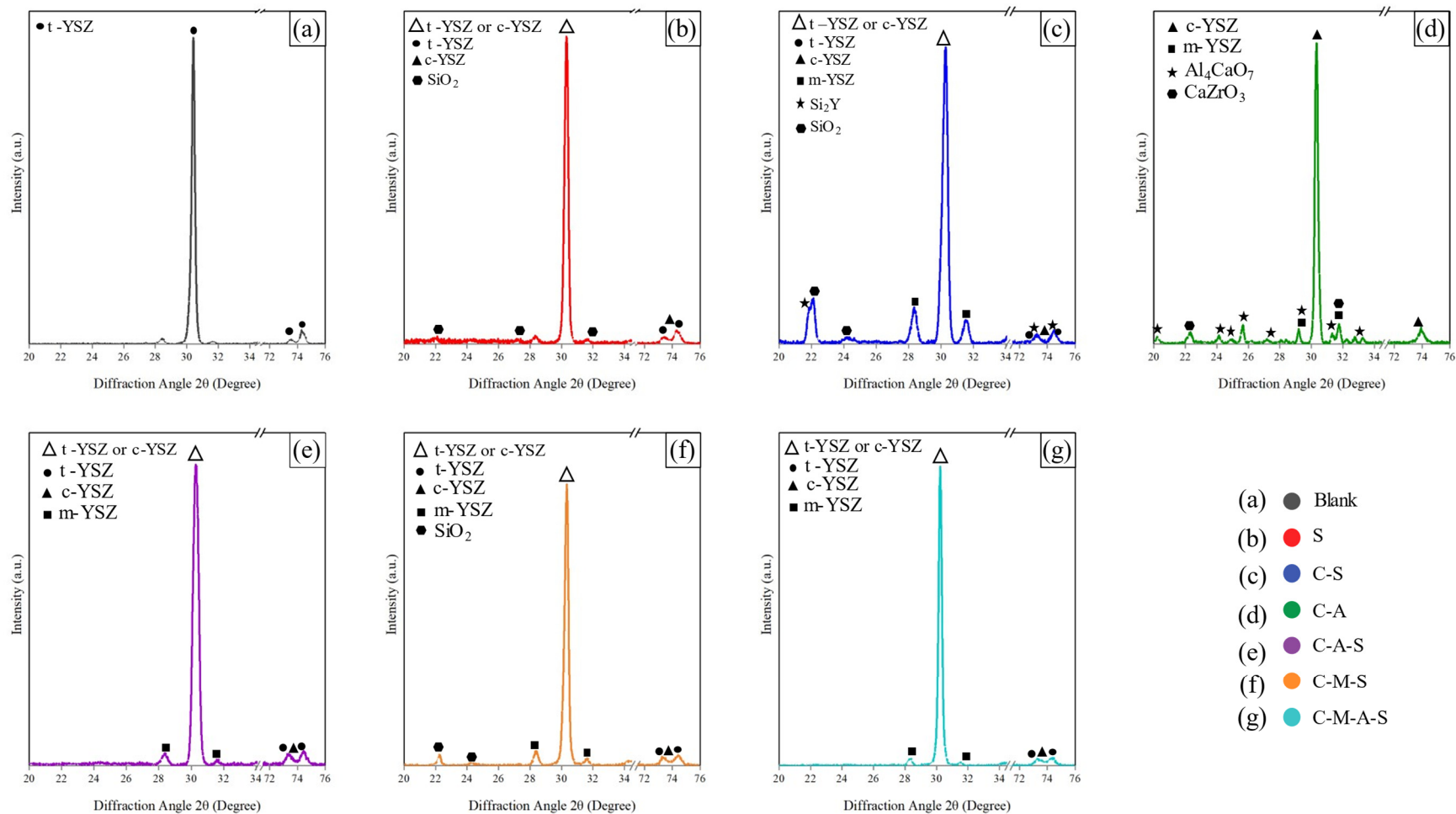
Fig. 4.4. XRD diffraction patterns of YSZ coatings after five cycles of contamination/ablation and reference sample ablated without impurities.

EDS analysis of the samples exposed to S, C-S, and C-A confirmed that the adhesion of deposits on top of the surface introduced a chemical interaction between the bulk YSZ matrix and the impurities (Fig. 4.5a, b, and c). In every case, the presence of one or more reaction layers between the impurity-based products and the bulk YSZ confirmed the reactivity of the impurities with the TBCs. The most prominent case is observed on the sample expose to C-A, where the reaction products of C-A with YSZ exhibit six phases labeled from the YSZ to the impurities core (Fig. 4.5b). Semi-quantitative composition analysis of each sample reveals that the YSZ topcoat is capable of incorporating $SiO_2$ (<1%) in its matrix. Therefore, precipitation of $SiO_2$-based impurities on the sample surface occurred until the third thermal cycle of the YSZ topcoat exposed to S. In all samples the impurities precipitating/crystallizing on the surface contained yttrium and zirconium in a similar ratio as the TBC, but their concentration changed along with the phase layers. The semi-quantitative composition analysis depicts the diffusion of yttrium and zirconium in the impurities core and the diffusion of impurities in the YSZ topcoat. Both, the phase changes and concentration trends suggest the congruent dissolution of 7YSZ in the solid impurities. Collectively, the evidence found in both XRD and EDS denotes that the thermochemical interaction of contaminants was similar for the analyzed compositions at 1400°C and linked directly to the non-desirable transformation of t'-YSZ. None the less, the contaminant diffusion trends were different in the analyzed cases, suggesting that the severity of interaction is dependent on the impurities composition and temperature. An in-depth kinetic assessment of impurities and YSZ interaction at different temperatures is out of the scope of this study.
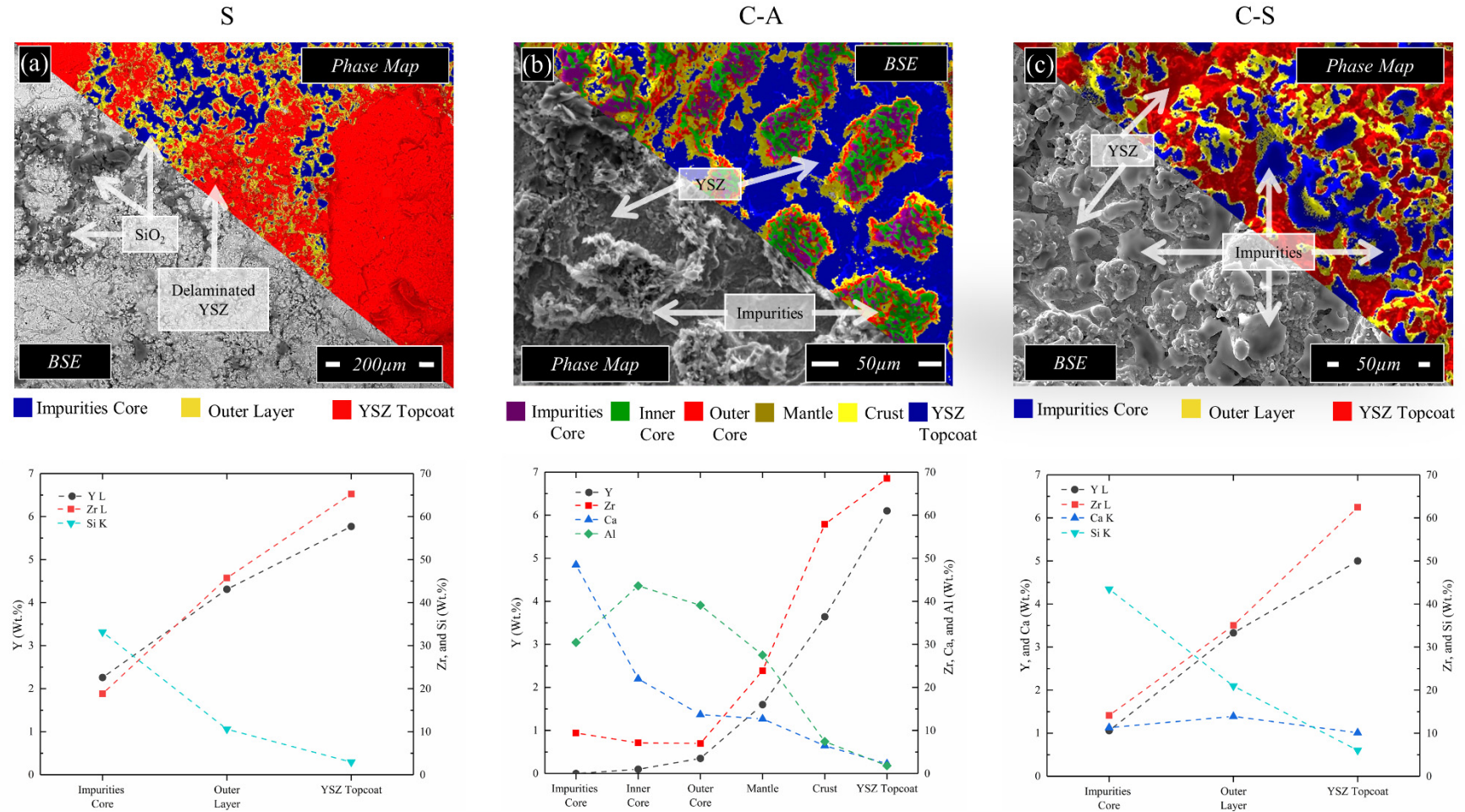
Fig. 4.5. BSE micrographs and EDS analysis of APS YSZ topcoats after 50 minutes of ablation with impurities, showing the phases that crystallized on top of the coatings and the resulting element concentration across each phase.

The rate at which the samples delaminated due to the interaction with the impurity cocktails was tracked with topcoat macrographs and monitoring the weight percent change of the samples. The macrographs for all the analyzed samples revealed that the coatings delaminated regardless of the composition of the impurity compound (Fig. 4.6). However, depending on the composition of the contaminants, the samples delaminated at different rates. Fig. 4.6a shows that the last sample to delaminate was the TBC sprayed with silica; in contrast, the topcoats exposed to C-A-S and C-M-A-S manifested spallation after the second ablation cycle (Fig. 4.6d and f). Interestingly, the coatings sprayed with C-M-A-S did not exhibit premature delamination in comparison to a simpler impurity system like C-A-S, but the severity of degradation was macroscopically different.
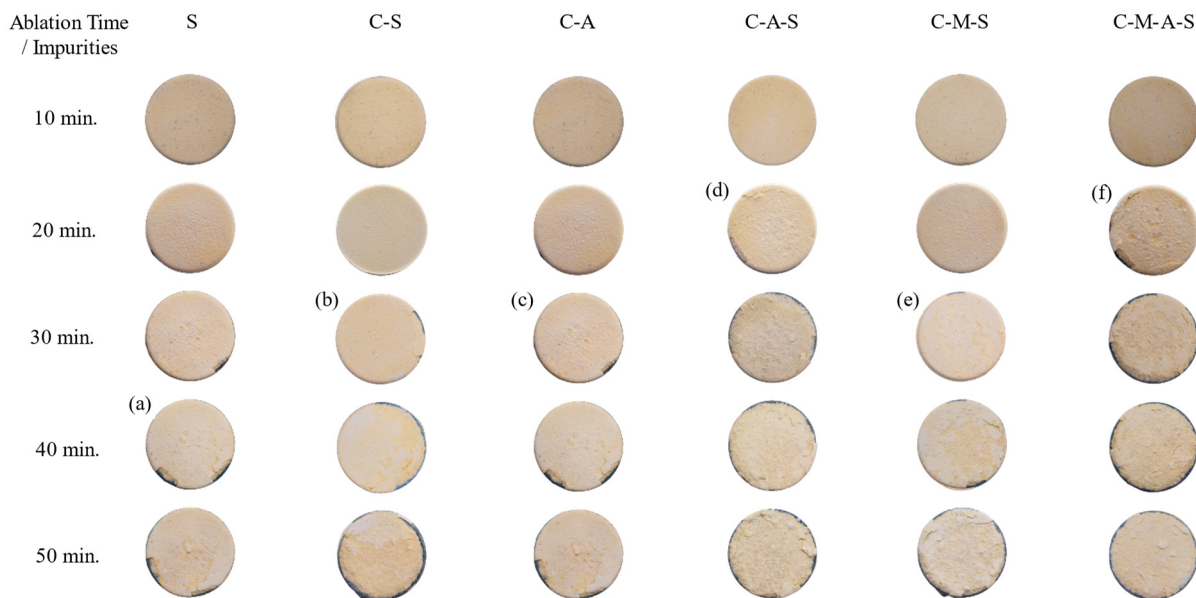


Fig. 4.6. Surface photographs of APS TBCs exposed to impurities and ablated at 1400°C showing the cycle at which the topcoats started to delaminate for: (a) S, (b) CS, (c) CA, (d) CAS, (e) CMS and (d) CMAS.

The weight percent change after 50 minutes of ablation reveals that the severity of the attack is higher on the samples exposed to C-S, C-M-A-S, C-M-S, and C-A-S (Fig. 4.7). There is no evidence suggesting that a specific CMAS constituent preluded the delamination of the TBC. However, any combination of C-M-A-S impurities induced TBCs failure regardless of their interaction mechanism with the topcoat.
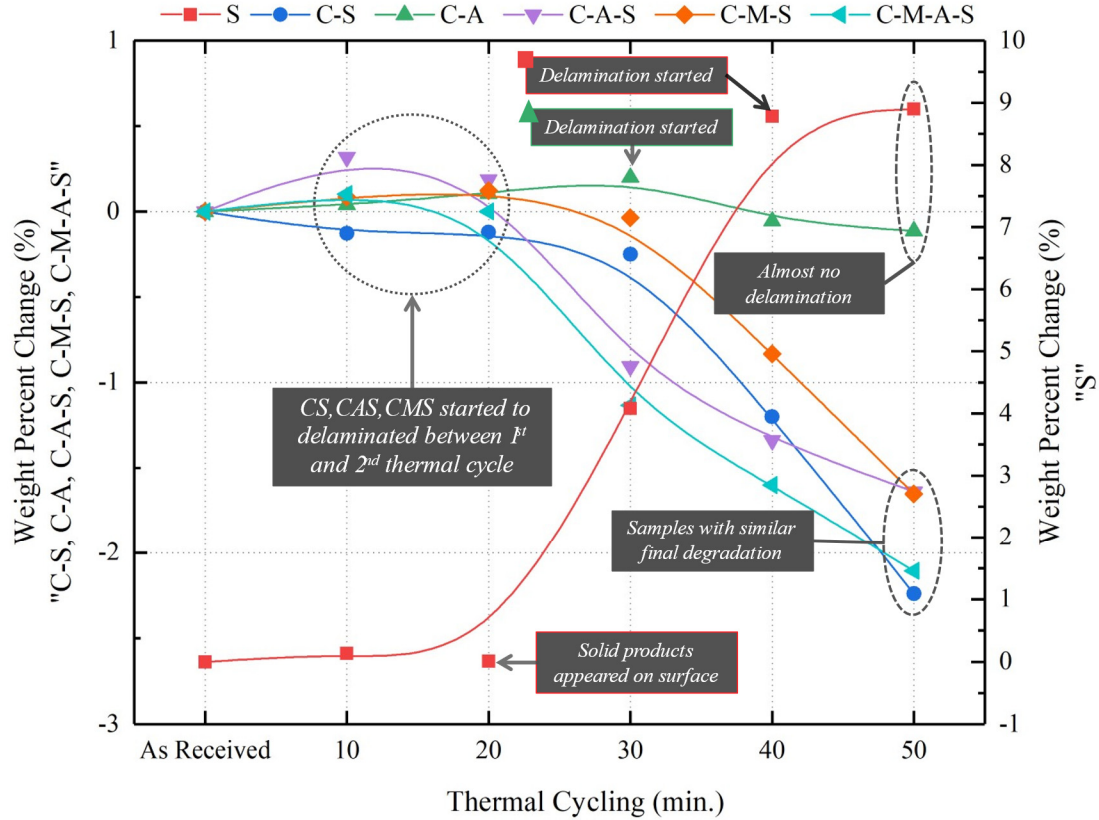
Fig. 4.7. Weight change of APS TBCs after each contamination/ablation cycle.

### 4.4.3 YSZ and CMAS constituents thermomechanical interaction

Cross-section analysis revealed the thermomechanical interactions that contributed to the delamination of the TBCs. Fig. 4.8, and Fig. 4.9 shows the two cases discerned for the impurities in this study. The first case encloses solid impurities that did not infiltrate the ceramic coatings but solidified on top of the TBC. Fig.4.8a,b, and d show that the impurities that crystallized on the topcoat surface (S, CA, and CS) cause the nucleation of cracks in the proximity of the surface. A closer look at the areas where the impurities adhered revealed that the thermochemical interaction of CA and CS with the topcoat induced a morphology change of the bulk YSZ, going from a highly dense to a porous topcoat where the cracks propagate along the horizontal plane of the coating (Fig. 4.8c and e). Both the mismatch in the thermal expansion coefficient between the top coat-impurities and a presumably less strain tolerant porous YSZ caused the delamination of the TBC. Fig. 4.9 exemplifies the second case scenario in which the impurities melted and subsequently infiltrated the TBCs; this case encloses the samples contaminated with C-A-S, C-M-S, and C-M-

A-S. The presence of a reaction layer next to the bond coat implies that the impurities thoroughly infiltrated the topcoat. Fig. 4.9a-c show that, for any case, the horizontal cracks propagate next to the contaminants solidified in the areas occurring along with the entire topcoat but mainly in the proximity of the bond coat.

The evidence analyzed with consideration of the XRD, EDS and SEM micrographs revealed that the composition and morphology of the YSZ changed when interacting with any combinations of C-M-A-S constituents. The interactions of the impurities with the TBC diverged in the depth of penetration of the impurities. Two cases were discerned, a first case in which the impurities solidified on the coating surface and interacted thermochemically with the topcoat, and a second case in which the topcoat was infiltrated, and the impurities reached the bond coat. Both observations of products solidifying on top of the surface or fully infiltrating the TBC agreed with the observations of Poerschke et al. [20] noting that the cracks inducing the TBC delamination nucleate in the vicinity of the solidified impurities due to the thermal mismatch between the YSZ matrix and the glassy byproducts. However, the evidence demonstrated that the impurity compound modified the rate at which the ceramic coatings failed.
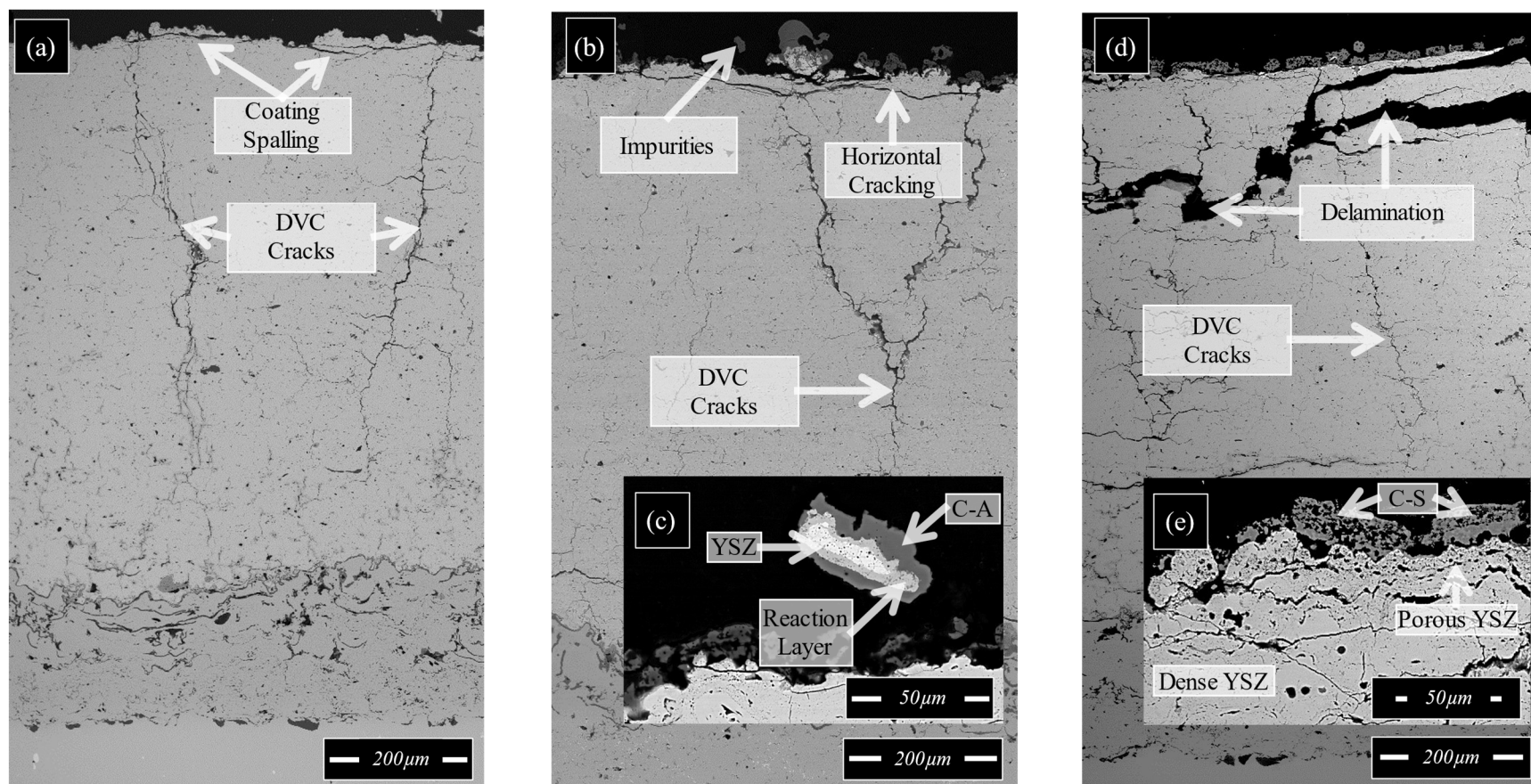
Fig. 4.8. Cross-section micrographs of APS TBCs showing infiltration of impurities and topcoat delamination: (a) C-A-S, (b) C-M-S, and (c) C-M-A-S.
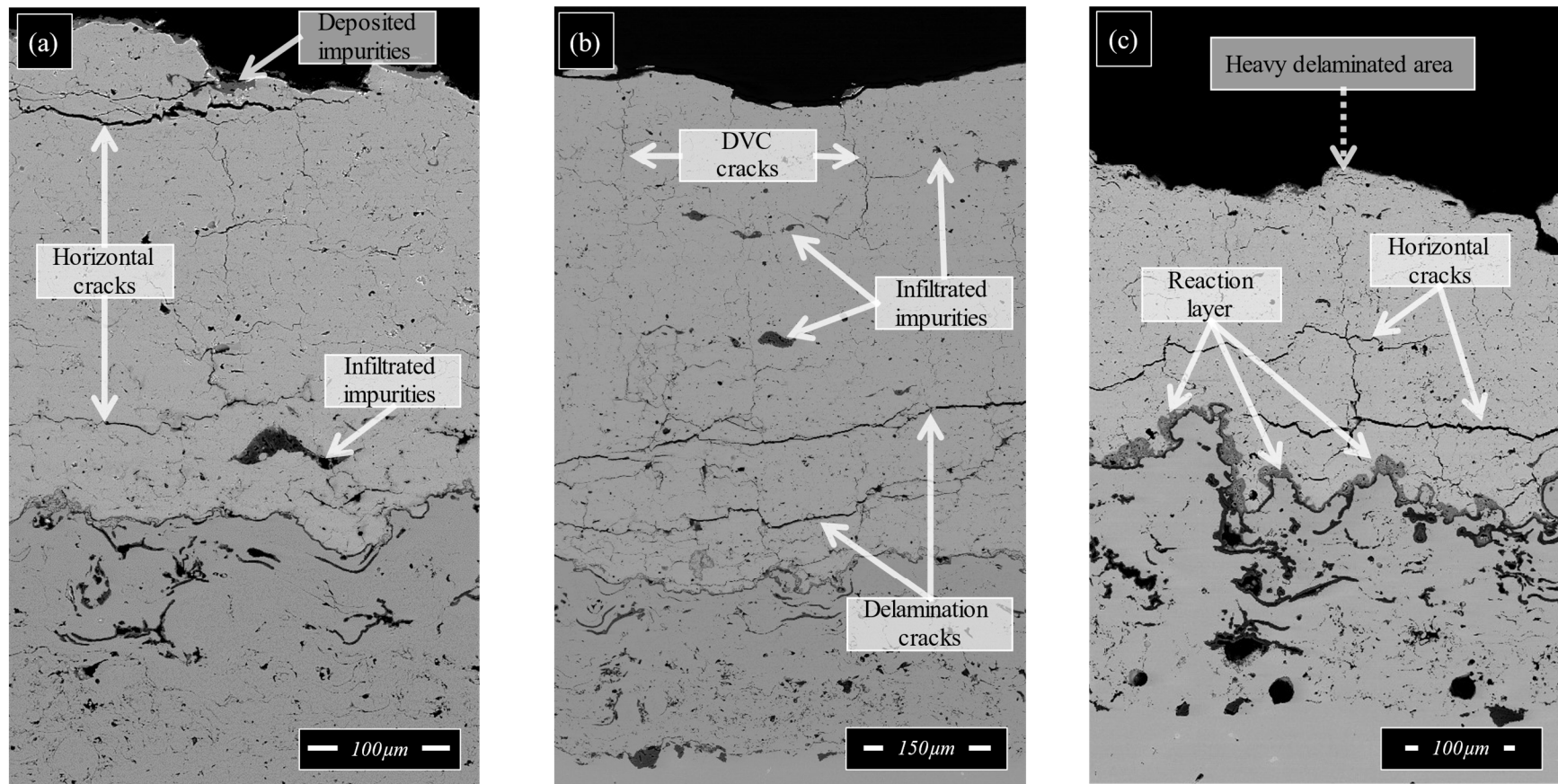
Fig. 4.9. Cross-section micrographs of APS TBCs showing infiltration of impurities and topcoat delamination: (a) C-A-S, (b) C-M-S, and (c) C-M-A-S.

## 4.5 Conclusions

This work analyzed the degradation of APS YSZ TBCs when exposed to the primary impurities found in biofuel ash to include CaO, MgO, $Al_2O_3$, and $SiO_2$. A comparison of the delaminated TBCs with a C-M-A-S reference composition revealed that compositions with fewer impurities than CMAS are detrimental for TBCs. Two scenarios were elucidated. The first corresponds to impurities that infiltrated the topcoat and interacted thermomechanically with the coating, and second theater enclosing the cases in which the contaminants crystallized on the sample surface and decomposed the YSZ matrix via a thermochemical interaction. Whether the deposited impurities only crystallized on the surface (i.e., no topcoat infiltration) or melted and infiltrated the coating, the TBCs failed.

## 4.6 Acknowledgments

## 4.7 References

[1]     M. Arai, H. Ochiai, and T. Suidzu, "A novel low-thermal-conductivity plasma-sprayed thermal barrier coating controlled by large pores," *Surf. Coatings Technol.*, **285** 120–127 (2016).

[2]     N. Coomar and R. Kadoli, "Comparative analysis of steady-state heat transfer in a TBC," *Sadhana - Acad. Proc. Eng. Sci.*, **35** [February] 1–17 (2010).

[3]     T. Torigoe, Y. Okajima, I. Okada, J. Masada, and K. Tsukagoshi, "Development of the Advanced TBC for High-Efficiency Gas Turbine," *Mater. Sci. Forum*, **879** 1980–1986 (2016).

[4]     Y. Tamarin, "Choosing Optimum Coatings for;" pp. 5–23 in *Prot. Coatings Turbine Bl.* 2002.

[5]     A.M. Kolagar, N. Tabrizi, M. Cheraghzadeh, and M.S. Shahriari, "Failure analysis of gas turbine first stage blade made of nickel-based superalloy," *Case Stud. Eng. Fail. Anal.*, **8** [February] 61–68 (2017).

[6]     L.S. Langston, "Gems of Turbine Efficiency," *Mech. Eng.*, **136** [09] 76 (2018).

[7]     A. Keyvani, M. Saremi, M. Heydarzadeh Sohi, and Z. Valefi, "A comparison on thermomechanical properties of plasma-sprayed conventional and nanostructured YSZ TBC coatings in thermal cycling," *J. Alloys Compd.*, **541** 488–494 (2012).

[8]     C. Yu, H. Liu, C. Jiang, Z. Bao, S. Zhu, and F. Wang, "Modification of NiCoCrAlY with Pt: Part II. Application in TBC with pure metastable tetragonal (t′) phase YSZ and thermal cycling behavior," *J. Mater. Sci. Technol.*, **35** [3] 350–359 (2019).

[9]     F. Klaus and C. Ley, "Review on advanced EB-PVD Ceramic Ttopcoats for TBC applications ar," *Appl. Ceram. Technol.*, **1** [4] 302–315 (2004).

[10]    G. Witz, V. Shklover, W. Steurer, S. Bachegowda, and H.P. Bossmann, "High-temperature interaction of yttria stabilized zirconia coatings with $CaO-MgO-Al_2O_3-SiO_2$ (CMAS) deposits," *Surf. Coatings Technol.*, **265** 244–249 (2015).

[11]    Q. Ahmed, I.N. Qureshi, and I.U. Salam, "Investigation of Hot Section (Nozzle Guiding Vane) Distress due to Interaction of Thermal Barrier Coatings with CMAS," *Key Eng. Mater.*, **778** 245–250 (2018).

[12]    T.R. Kakuda, C.G. Levi, and T.D. Bennett, "The thermal behavior of CMAS-infiltrated thermal barrier coatings," *Surf. Coatings Technol.*, **272** 350–356 (2015).

[13]    R. Naraparaju, J.T. Gomez Chavez, U. Schulz, and C. V. Ramana, "Interaction and infiltration behavior of Eyjafjallajökull, Sakurajima volcanic ashes and a synthetic CMAS containing FeO with/in EB-PVD ZrO2-65 wt% Y2O3coating at high temperature," *Acta Mater.*, **136** 164–180 (2017).

[14]    V.H. Mohan, P., Patterson, T., Sohn, Y., & Desai, "Degradation of Yttria Stabilized Zirconia Thermal Barrier Coatings by Molten CMAS ($CaO-MgO-Al_2O_3-SiO_2$ ) Deposits," *Mater. Sci. Forum*, **598** [January] 207–212 (2008).

[15]    N. Yilmaz and A. Atmanli, "Sustainable alternative fuels in aviation," *Energy*, **140** [2017] 1378–1386 (2017).

[16]    FAA, Boeing, and University of Dayton Research Institue, "Impact of Alternative Jet Fuel and Fuel Blends on Non-Metallic Materials Used in Commercial Aircraft Fuel Systems CLEEN Project Final Report – Submitted by The Boeing Company," (2014).

[17]    J. Cain, M.J. Dewitt, D. Blunck, E. Corporan, R. Striebich, D. Anneken, C. Klingshirn, W.M. Roquemore, *et al.*, "Characterization of gaseous and particulate emissions from a turboshaft engine burning conventional, alternative, and surrogate fuels," *Energy and Fuels*, **27** [4] 2290–2302 (2013).

[18]    K. Masera and A.K. Hossain, "Biofuels and thermal barrier: A review on compression ignition engine performance, combustion, and exhaust gas emission," *J. Energy Inst.*, (2018).

[19]    J. Yang, Z. Xin, Q. (Sophia) He, K. Corscadden, and H. Niu, "An overview on performance characteristics of bio-jet fuels," *Fuel*, **237** [August 2018] 916–936 (2019).

[20]    D.L. Poerschke, R.W. Jackson, and C.G. Levi, "Silicate Deposit Degradation of Engineered Coatings in Gas Turbines: Progress Toward Models and Materials Solutions," *Annu. Rev. Mater. Res.*, **47** [1] 297–330 (2017).

[21]     Q.S.M. Kwok, D.E.G. Jones, G.F. Nunez, J.P. Charland, and S. Dionne, "Characterization of bio-fuel and bio-fuel ash," *J. Therm. Anal. Calorim.*, **78** [1] 173–184 (2004).

[22]     S.F. Miller and B.G. Miller, "The occurrence of inorganic elements in various biofuels and its effect on ash chemistry and behavior and use in combustion products," *Fuel Process. Technol.*, **88** [11–12] 1155–1164 (2007).

[23]     Z. Chen, J. Mabon, J.G. Wen, and R. Trice, "Degradation of plasma-sprayed yttria-stabilized zirconia coatings via ingress of vanadium oxide," *J. Eur. Ceram. Soc.*, **29** [9] 1647–1656 (2009).

[24]     P. Mohan, T. Patterson, B. Yao, and Y. Sohn, "Degradation of thermal barrier coatings by fuel impurities and CMAS: Thermochemical interactions and mitigation approaches," *J. Therm. Spray Technol.*, **19** [1–2] 156–167 (2010).

[25]     L. Li, N. Hitchman, and J. Knapp, "Failure of thermal barrier coatings subjected to CMAS attack," *Proc. Int. Therm. Spray Conf.*, **19** [January] 77–82 (2009).

[26]     S. Krämer, J. Yang, C.G. Levi, and C.A. Johnson, "Thermochemical Interaction of Thermal Barrier Coatings with Molten CaO–MgO–Al$_2$O$_3$–SiO$_2$(CMAS) Deposits," **3175** 3167–3175 (2006).

[27]     J.H.R. Velasco, G. Kilaz, and R.W. Trice, "Application of biofuel impurities and effect on the hot corrosion of yttria-stabilized zirconia thermal barrier coatings," *Surf. Coat. Technol.* (2018).

[28]     H. Araki, M. Watanabe, Y. Sakka, S. Kuroda, T. Ohnuki, X. Chen, H. Murakami, and M. Gizynski, "Columnar and DVC-structured thermal barrier coatings deposited by suspension plasma spray: high-temperature stability and their corrosion resistance to the molten salt," *Ceram. Int.*, **42** [15] 16822–16832 (2016).

[29]     A. International, "Standard Test Method for Oxyacetylene Ablation Testing of Thermal Insulation," *ASTM Int.*, **80** [C] 1–6 (2008).

[30]     M.H. Vidal-Setif, N. Chellah, C. Rio, C. Sanchez, and O. Lavigne, "Calcium-magnesium-alumino-silicate (CMAS) degradation of EB-PVD thermal barrier coatings: Characterization of CMAS damage on ex-service high-pressure blade TBCs," *Surf. Coatings Technol.*, **208** 39–45 (2012).

[31]     B. Cheng, Y.M. Zhang, N. Yang, M. Zhang, L. Chen, G.J. Yang, C.X. Li, and C.J. Li, "Sintering-induced delamination of thermal barrier coatings by gradient thermal cyclic test," *J. Am. Ceram. Soc.*, **100** [5] 1820–1830 (2017).

[32]     D. Zhou, O. Guillon, and R. Vaßen, "Development of YSZ Thermal Barrier Coatings Using Axial Suspension Plasma Spraying," *Coatings*, **7** [8] 120 (2017).

[33]     R.W. Trice, Y.J. Su, J.R. Mawdsley, K.T. Faber, A.R. De Arellano-López, H. Wang, and W.D. Porter, "Effect of heat treatment on phase stability, microstructure, and thermal conductivity of plasma-sprayed YSZ," *J. Mater. Sci.*, **37** [11] 2359–2365 (2002).

[34]     F. Abe, S. Muneki, and K. Yagi, "Tetragonal to monoclinic transformation and microstructural evolution in ZrO2–9.7 mol% MgO during cyclic heating and cooling," *J. Mater. Sci.*, **32** [2] 513–522 (1997).

# 5. DEGRADATION OF YTTRIA STABILIZED ZIRCONIA THERMAL BARRIER COATINGS BY THE COMBINED EFFECT OF BIOFUEL IMPURITIES AND CMAS

*A version of this chapter has been submitted for publication in a peer-reviewed journal.*

## 5.1 Abstract

State of the art 7-8 wt%$Y_2O_3$-$ZrO_2$ (YSZ) thermal barrier coatings (TBCs) are used to increase the temperature at which superalloy-made components (e.g., blades, vanes, liners) operate in a gas turbine. When operating above ~1250°C, TBCs are prone to corrosion induced by deposits of calcium-magnesium-aluminum silicates (CMAS) that melt, infiltrate, and induce the failure of the ceramic coatings. CMAS deposits arise when flying in a volcanic ash or desert sand environment. However, the combustion of biofuels in gas turbines has come with contaminants previously unknown to TBCs. The primary contaminants found in biofuels combustion products are $SiO_2$, CaO, MgO, $Al_2O_3$, $Fe_2O$, $TiO_2$, ZnO, and $K_2O$. Arising the possibility to form deposits of C-M-A-S unreacted constituents that when combined with glass modifiers (i.e., $Fe_2O$, $TiO_2$, ZnO, and $K_2O$) could hasten the degradation of TBCs. In this work, we used a burner rig to thermally cycle YSZ TBCs that were exposed to C-M-A-S alone and in combination with other impurities exclusive of biofuels. EDS and XRD analysis showed that $K_2O$ and $TiO_2$ exacerbated the detrimental effect of C-M-A-S on TBCs, while $Fe_2O_3$ and ZnO delaminated the coating independently to CMAS constituents.

## 5.2 Introduction

A practical manner to increase the performance of a gas turbine is to increase the turbine inlet temperature (TIT). With current operation conditions, the TIT goes above ~1400°C, overpassing the melting point of gas turbines superalloy components such as linings, nozzles, blades, and vanes [1–3]. A method to increase the turbine efficiency and avoid damage of the metallic parts is to employ thermal barrier coatings (TBCs), multilayered systems that thermally insulate the components in the hot-gas-path of the engine [4–6]. Ultimately, the use of TBCs lowers the temperature gradients, reduces the thermally induced stresses, and extends the lifetime of the

engine [7, 8]. A typical TBC consist of an insulating ceramic topcoat attached to the superalloy substrate by an oxidant resistant bondcoat. NiCrAlY alloys are the choice for bondcoat layers since it outperforms CoCrAlY compounds when operating in oxidizing atmospheres above ~1000°C. For the topcoat layer, the metastable (t') 7-8 wt%$Y_2O_3$-$ZrO_2$ (YSZ) is the preferred ceramic mostly due to its low thermal conductivity (2.2 $Wm^{-1}K^{-1}$), high melting point (~2680°C) and mechanical properties that make it relatively resistant to erosion [9, 10]. The most common methodologies to apply bondcoat and topcoat layers are air plasma spray (APS) and electron beam physical vapor deposition (EB-PVD) [11].

Regardless of the quasi-ideal properties of YSZ for TBCs, increasing the components surface temperature above 1250 °C introduced corrosion problems associated with molten deposits arising from in-flight conditions. Observations of ex-service engine parts indicate that molten deposits penetrate the porous TBC microstructure and change the stiffness of the infiltrated regions. The compliance between a less strain tolerant infiltrated region and a non-infiltrated region induce the nucleation of cracks that propagate across the topcoat, ultimately causing the delamination of the TBC [12, 13]. Also, molten deposits species interact thermochemically with YSZ. The chemical attack accelerates the phase transformation of the metastable YSZ (t'-$ZrO_2$ → t-$ZrO_2$ + c-$ZrO_2$ → m- $ZrO_2$ + c-$ZrO_2$), giving place to a volumetric expansion and shear stress that prelude the failure of the coating [14, 15]. Due to its highly detrimental effect on TBCs, CMAS molten deposits have received particular attention over the last decade. Currently, the degradation mechanisms that take place when molten CMAS interacts with YSZ TBCs are still under investigation as to develop mitigation strategies to counter TBCs degradation [16–19]. Observations indicate that CMAS deposits originate from airborne ingested by the turbine when operating in a desert-sand or volcanic ash environment. However, the ongoing international interest to introduce alternative fuels in gas turbines introduces trace element species that form deposits with compositions unknown to TBCs [20, 21].

Chemical analysis of ash produced by burning biofuels revealed the trace elements that deposit on the surface of the coating and infiltrate the TBCs. Biofuels ash contaminants include but are not limited to $SiO_2$, CaO, $Al_2O_3$, $Fe_2O_3$, MgO, $TiO_2$, SrO, $SO_3$, $K_2O$, and ZnO [22–24]. Webb et al. [25] noticed that the elements in the list could be classified as glass modifiers, species that can

change the viscosity and physical properties of the glass (i.e., CaO, $Al_2O_3$, $Fe_2O_3$, MgO and $K_2O$) and network formers (i.e., $SiO_2$ and $TiO_2$). Noting that the list of contaminants includes CMAS unreacted constituents, $CaO$-$MgO$-$Al_2O_3$-$SiO_2$ (i.e., C-M-A-S), in this article we analyzed the effect of network formers and modifiers in combination with C-M-A-S. The main goal is to identify the biofuel impurities that exacerbate the negative effect of CMAS on YSZ APS TBCs.

## 5.3    Experimental methods

### 5.3.1    Formulation and application of the impurity cocktails

To analyze the effect of the glass modifiers in combination with other biofuel impurities, we took a CMAS reference composition as the baseline of molten deposits formed from $SiO_2$. Therefore, all of the samples were exposed to the unreacted compounds of C-M-A-S in the proper ratio to approach a composition observed on ex-service turboshaft shrouds reported by Borom et al. [26] (i.e., $33CaO$-$9MgO$-$13AlO_{1.5}$-$45SiO_2$ mol%). In total, the degradation of six samples was analyzed to include a sample with no impurities and a sample with only the unreacted constituents of CMAS. Table 5.1 enlists the compositions and concentrations of the CMAS modifiers taken into consideration for this study.

Table 5.1. System of impurities deposited on APS YSZ TBCs.

| Sample No. | Impurities composition (mol%) | Deposited impurities concentration | Modifiers $T_m$ |
|:---:|:---:|:---:|:---:|
| 1 | No Impurities | N/A | N/A |
| 2 | CMAS | 2 mols of CMAS | 1250°C |
| 3 | CMAS – $Fe_2O_3$ | 1 mol CMAS – 1mol $Fe_2O_3$ | 1565°C |
| 4 | CMAS – $TiO_2$ | 1mol CMAS – 1 mol $TiO_2$ | 1843°C |
| 5 | CMAS – ZnO | 1mol CMAS – 1mol $TiO_2$ | 1975°C |
| 6 | CMAS – $K_2O$ | 1mol CMAS – 1 mol $K_2O$ | 891°C |

To formulate a solution with unreacted C-M-A-S constituents, nitrates of alkaline metals $Ca(NO_3)_2$ (Sigma Aldrich), $Mg(NO_3)_2$ (Sigma Aldrich), $Al(NO_3)_3$ (Sigma Aldrich) and the ceramic precursor

$Si(OC_2H_5)_4$ (Sigma Aldrich), were incorporated in a 10% vol concentration solution in ethanol. The impurity cocktail reacts at 600°C to give place to the C-M-A-S unreacted constituents, as described in detail in previous studies [27]. Impurity cocktails of glass modifiers were prepared individually, departing from 15 wt.% in ethanol $Fe_2O_3$ (Sigma Aldrich), 40 wt.% in $H_2O$ $TiO_2$ (Sigma Aldrich), 40 wt.% in ethanol ZnO (Sigma Aldrich) and $K_2CO_3$ (Sigma Aldrich). Glass modifiers were diluted individually in ethanol or water to achieve precursors concentrations of 5 vol%. For the case of $K_2CO_3$, we considered that upon reaction at 900°C, the precursor would give place to the desired impurity as described in:

$$K_2CO_3(s) \rightarrow K_2O(s) + CO_2(g)$$

TBCs were sprayed with the impurity cocktails to deposit the contaminants on topcoats surfaces. Previous to the spraying process, the TBCs were pre-heated in a hot plate in direct contact with the substrates. The main idea was to evaporate the solvent of the impurity cocktail when in contact with the samples and depositing only the impurities of interest. Topcoat's surface temperature was monitored with a type K sheathed thermocouple as to not go below 200°C while spraying the impurity cocktails. An airbrush with the pressure held at 0.2 MPa was used to spray the samples with the impurity cocktails. For all cases, samples were sprayed with the C-M-A-S solution in intervals of 15 seconds of spraying and 15 seconds of no spraying to let the ethanol/water evaporate and the sample to partially reheat. After the application of the C-M-A-S ethanol solution, the samples were allowed to dry at 200°C for 20 minutes. Followed by the drying of the samples, the impurity cocktails containing glass modifiers were sprayed on to the TBCs with the same methodology as the C-M-A-S impurity cocktail. The concentration of impurities on the topcoat was monitored after each spraying cycle of C-M-A-S and glass modifiers. The impurities concentration on the surface of the sample (i.e., no ethanol or water) was characterized to be 1 mol of C-M-A-S with the reference composition and 1 mol of the reacted glass modifier (i.e., $Fe_2O_3$, $TiO_2$, ZnO and $K_2O$). After spraying the samples with the impurity cocktails, the TBCs were dried at room temperature for 24 hrs.

### 5.3.2 Morphology of evaluated TBCs

The effect of the unreacted C-M-A-S constituents and biofuels impurities was investigated on APS TBCs manufactured by Praxair. TBCs consisted of a topcoat layer (7 wt.% $Y_2O_3$-$ZrO_2$) attached to the substrate by a corrosion-resistant bondcoat (CoNiCrAlY). Topcoat and bondcoat layers were applied to an Inconel 718 substrate with a cylindrical shape. The substrate had a 25 mm diameter and a 6 mm thickness, while topcoat and bondcoat had thicknesses of 700±50µm and 230±50µm respectively. The topcoat was characterized to be 84% dense. Fig. 5.1 shows the surface and cross-sectional micrographs of as received TBCs.
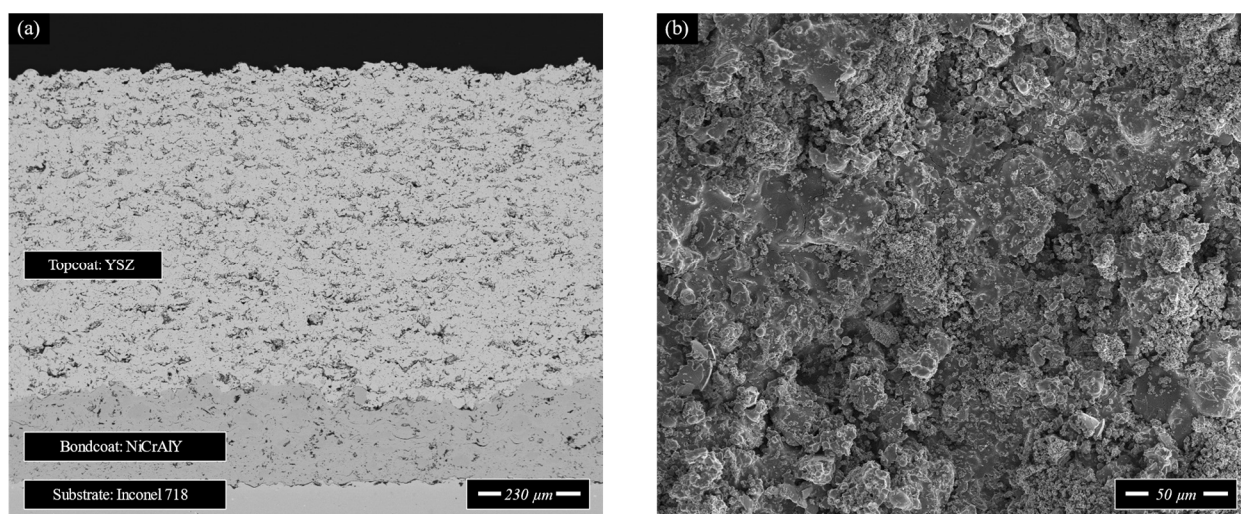


Fig. 5.1. SEM micrographs showing the (a) cross section and (b) surface of APS TBCs in the as-received condition.

### 5.3.3 Ablation and characterization

An oxy-acetylene ablation rig was used to expose the samples to similar thermal conditions as in a gas turbine. Before each ablation cycle, TBCs were sprayed with the impurity cocktails formulated with the unreacted C-M-A-S and glass modifiers. All samples were ablated with a mixture of oxygen and acetylene of 10:12 liters per minute. The heat flux evolved by the combustion reaction was characterized to be 1.1 W/mm$^2$ with a circular foil heat flux transducer (Vatell Corporation, Christiansburg, VA). The topcoat surface temperature was monitored in intervals of 1 second with a specialty wavelength pyrometer (10.5 µm) calibrated at an emissivity of 0.95 (Williamson Corporation, Concord, MA). Samples back face temperature (i.e., substrate) were monitored in intervals of 1 second with a long wavelength pyrometer (8-14 µm) OS554AM-

MV-1 (Omega Engineering, Norwalk, CT). The "steady-state" topcoat surface temperature ranged between 1250°C and 1350°C while the back faces temperatures were monitored not to overpass 1000°C. Ablation cycles timing was started when the topcoat surface reached the minimum steady-state temperature (i.e., 1250°C), therefore heating and cooling transient periods were ignored for timing purposes. Each ablation cycle consisted of an impurity spray phase, a 10-minute ablation period in the burner rig, and 12 hrs. of samples resting/cooling in air until respraying with the impurity cocktails. TBCs surface delamination was tracked with macrographs and SEM micrographs after each ablation cycle. For the latter case, a carbon coating was necessary to reduce the charging effect produced by the dielectric nature of the YSZ. After thermal cycling, cross-sectional views of the TBCs were taken by mounting the samples in epoxy and polishing with diamond paste through 1 μm. For the cross-sections, a gold-palladium coating was used to reduce the charging of the coating due to the simplicity of the process. The phase evolution of the YSZ was monitored with X-Ray Diffraction patterns (XRD) gathered with a Bruker D8 focus diffractometer. XRD patterns were collected using a copper source ($\lambda$=0.1544 nm) in a 2θ interval from 20 to 90° and a 3 degrees per minute scan speed in steps of 0.01 degrees per step.

## 5.4    Results and discussion

### 5.4.1    Topcoat surface evaluation after ablation with biofuel impurities

Fig. 5.2 shows the APS topcoats surface after ablating them with C-M-A-S and glass modifiers for ten minutes (i.e., one ablation cycle). The baseline topcoat, the sample exclusively exposed to C-M-A-S, exhibited solidified bubbles, indication that the impurities reached the melting temperature (Fig. 5.2e). In comparison, the sample exposed to C-M-A-S and $TiO_2$ exhibited two morphologies of impurities on the surface. A morphology similar to C-M-A-S constituents, and another phase of glass grouped in particles as big as 200 μm, possibly compounded of $TiO_2$. The presence of the second morphology makes sense since $TiO_2$ is a network creator such as $SiO_2$. In contrast, the samples exposed to C-M-A-S constituents and $Fe_2O_3$, $K_2O$, and $ZnO$ (Fig. 5.2a-c) exhibited a single type of morphology, presumably incorporating the glass modifiers in the CMAS network. After the first ablation cycle, only the sample sprayed with the $F_2O_3$ impurity cocktail exhibited coating spallation. The spallation of the coatings was tracked by photographing the surface of the topcoats. The thermal cycling was stopped when the substrates were partially visible.
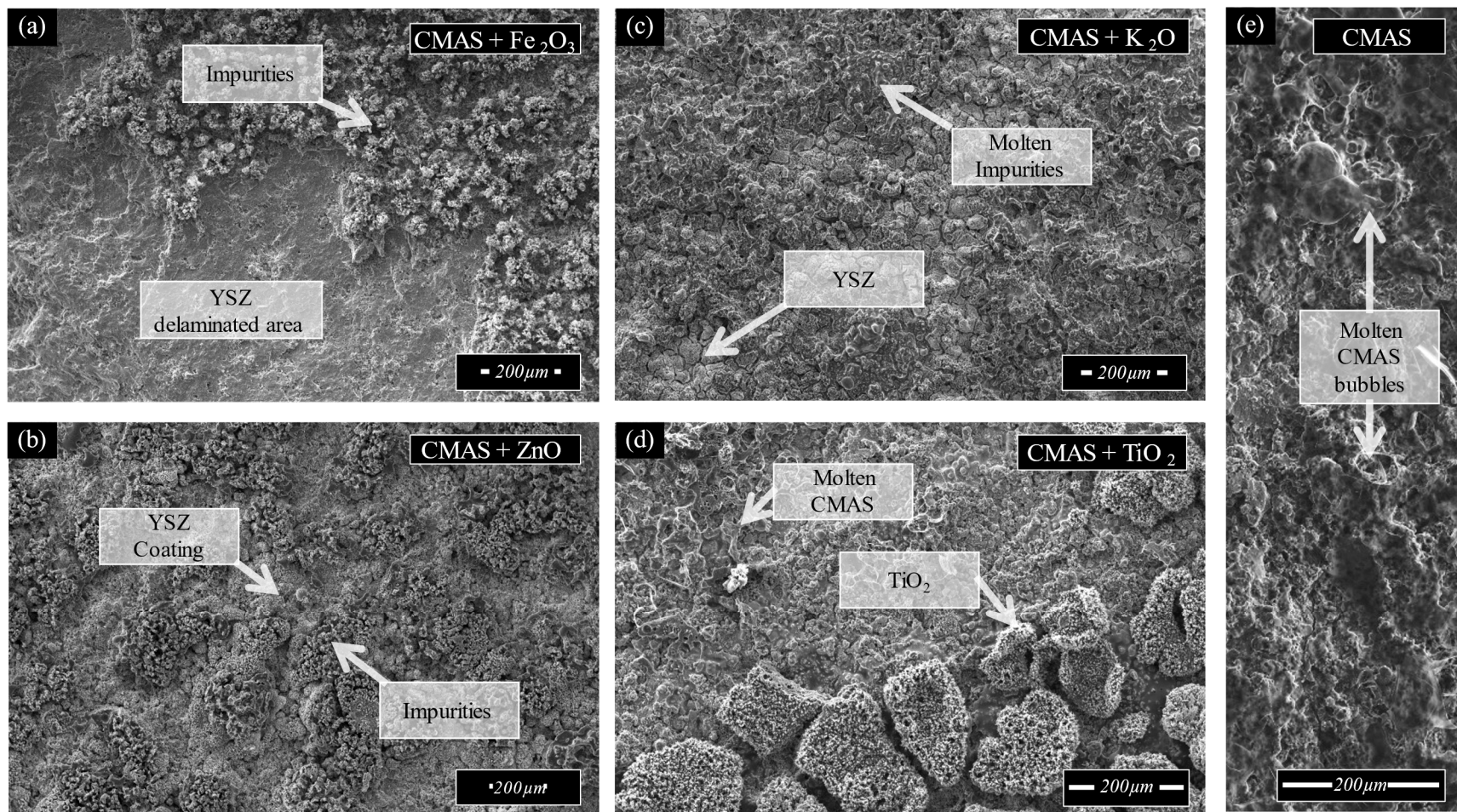
Fig. 5.2. Surface micrographs of APS TBCs after 10 minutes of ablation with biofuel impurities.

Fig. 5.3 shows that spallation occurred in the samples exposed to C-M-A-S and glass modifiers but not in the sample ablated without impurities, in which case the thermal cycling was stopped after 30 minutes of ablation (i.e., three thermal cycles of 10 minutes). Even though all impurities induced the TBCs spallation, the amount of coating lost was different from case to case.
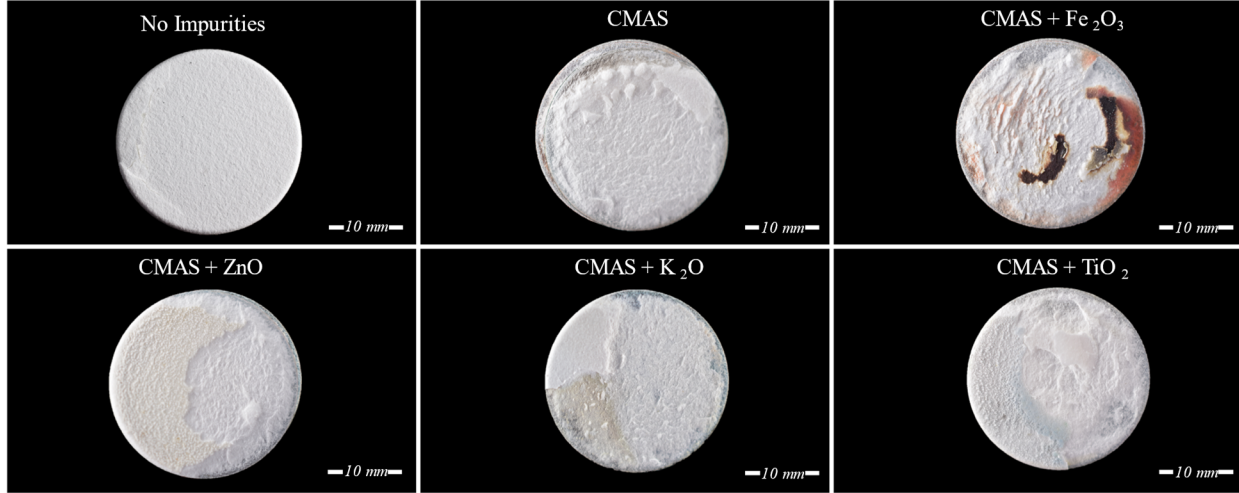


Fig. 5.3. Surface photographs of APS TBCs exposed to impurities and ablated at 1400°C during a total of 30 minutes.

Fig. 5.4 depicts the weight percent change of the samples along with the experiment. The trends show that the samples delaminated at different rates, and after 30 minutes of ablation, the sample that spalled the most was the one sprayed with C-M-A-S combine with $Fe_2O_3$.

The similar weight percent change trends in samples with $Fe_2O_3$ and $TiO_2$ raise the idea that the main factor for the delamination is the coefficient of thermal expansion (CTE) since the CTE of $Fe_2O_3$ ($10 \times 10^{-6}$/°C) and $TiO_2$ ($9 \times 10^{-6}$/°C) are closely similar. Alexander Fluegel's model [28] was used to evaluate the CTE of glass modifiers in combination with C-M-A-S. By using Winkelmann and Schott coefficients for every species, CTEs can be calculated from Eq. 5.1.

$$CTE = (.5)(.33CaO+.09MgO+.065Al_2O_3+.45SiO_2) + (.5)(Fe_2O_3+TiO_2+K_2O+ZnO) \times 10^{-6}/°C \quad (5.1)$$

Calculations with the previous model indicate that the maximum CTE is of C-M-A-S with $K_2O$ $CTE_{(C-M-A-S + K2O)} = 18.07 \times 10^{-6}$/°C, followed by $CTE_{(C-M-A-S + TiO2)} = 10.74 \times 10^{-6}$/°C, $CTE_{(C-M-A-S +}$

$_{Fe2O3)}$ =10.57x10$^{-6}$/°C, and CTE$_{(C-M-A-S + ZnO)}$= 6.90x10$^{-6}$/°C. The trend suggests that the prediction of the CTE influencing the fast delamination of the coating is followed at the beginning of the thermal cycling. However, the trend is not maintained after two more ablation cycles, presumably due to the contributions of thermochemical degradation.
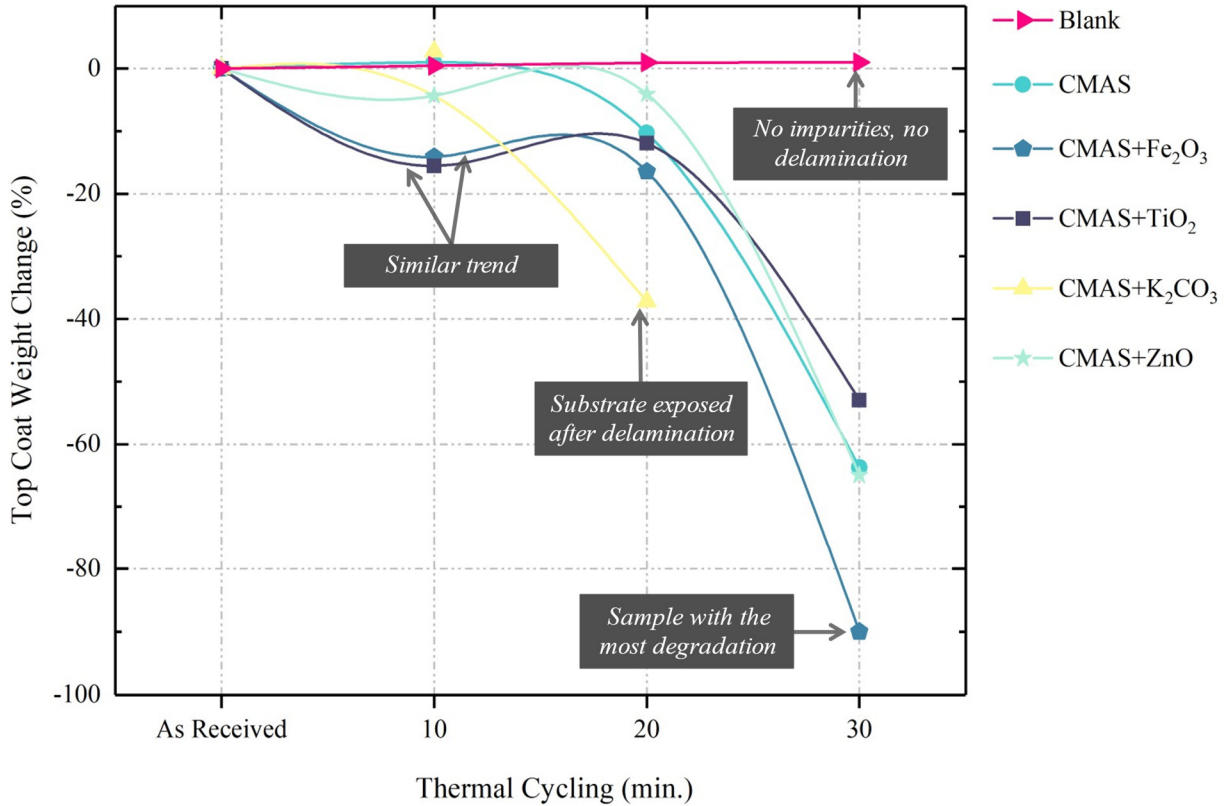


Fig. 5.4. Topcoat weight change of APS TBCs after spraying with impurities and ablating at 1400°C

## 5.4.2   Phase evolution of YSZ after ablation with biofuel impurities

The phase assemblage between the impurities and YSZ was investigated with XRD. Fig. 5.5 shows the diffraction patterns obtained after ablating the samples with C-M-A-S and glass modifiers. The baseline sample (i.e., TBC with C-M-A-S) does not exhibit peaks ascribed to the crystallization of silicates. However, the presence of peaks associated with monoclinic Zirconia indicates that the impurities induced the detrimental phase transformation of the t'-YSZ. TBCs sprayed with C-M-A-S and glass modifiers behaved in three elucidated manners. The diffraction patterns of topcoats exposed to Fe$_2$O$_3$ and ZnO show peaks exclusive of the crystallization of the glass modifiers, evidencing that CMAS constituents and glass modifiers did not mix entirely as to form secondary

phases. In the second case, the glass modifiers reacted with at least one constituent in C-M-A-S. For example, the sample sprayed with $TiO_2$ exhibit peaks related to TiSi. In the last scenario, the diffraction pattern of the sample with C-M-A-S and $K_2O$ did not exhibit peaks related to the decomposition of YSZ or crystallized impurities.

EDS analysis of the TBCs confirmed the thermochemical interaction and composition of impurities solidified on the surface of the topcoat. Fig. 5.6 shows the surface micrographs of the samples exposed to $Fe_2O_3$ and ZnO (i.e., glass modifiers that did not mix or decompose t'-YSZ) along with the elemental map analysis for both impurities. The elemental maps of the sample sprayed with C-M-A-S-ZnO show that the impurities on top of the sample are primarily Zn, with no traces of Si, Y, or Zr  (Fig. 5.6a). Observations in the sample sprayed with C-M-A-S-$Fe_2O_3$ indicated that $Fe_2O3$ did not mix with CMAS or caused yttrium depletion in the YSZ matrix. Therefore, XRD and EDS analysis agreed that the samples exposed to these impurities delaminated primarily to the thermomechanical interaction of the ZnO and $Fe_2O_3$ with the sample.

Phase analysis of the impurities that interacted thermochemically with the TBCs, either crystallizing in secondary phases or decomposing the t'-YSZ matrix, revealed the role of the impurities in the delamination of the topcoats. Fig. 5.7a shows that both Y and Zr diffuse in CMAS when interacting with the molten impurities. Even though Si trend shows to be the primary constituent diffusing in the YSZ matrix, the trends of Ca, Mg, and Al indicate a similar behavior as Si. Therefore, the destabilization of the t'-YSZ phase was not attributed to a single CMAS constituent but a combination of all. For the case of the topcoat sprayed with C-M-A-S-$TiO_2$, the phase map reveals four phases in which the concentrations of the C-M-A-S constituents varies inversely to the amount of Ti dissolved in the impurities (Fig. 5.7b). Regardless of each phase composition, Y and Zr concentrations were low in all phases. Evidencing that there was no YSZ decomposition due to the crystallized phases on the surface. Finally, Fig. 5.7c reveals that the sample exposed to C-M-A-S-$K_2O$ behaves similarly to the sample exposed with $TiO_2$, where the concentration of the glass modifier across phases diminishes as CMAS constituents increases. However, the traces of  Y and Zr indicate that $K_2O$ is responsible for the decomposition of the YSZ matrix. Thus, explaining that C-M-A-S and $K_2O$ attacked the sample with thermo-mechanical and thermo-chemical mechanisms, explaining the fast rate at which the sample delaminated.

89
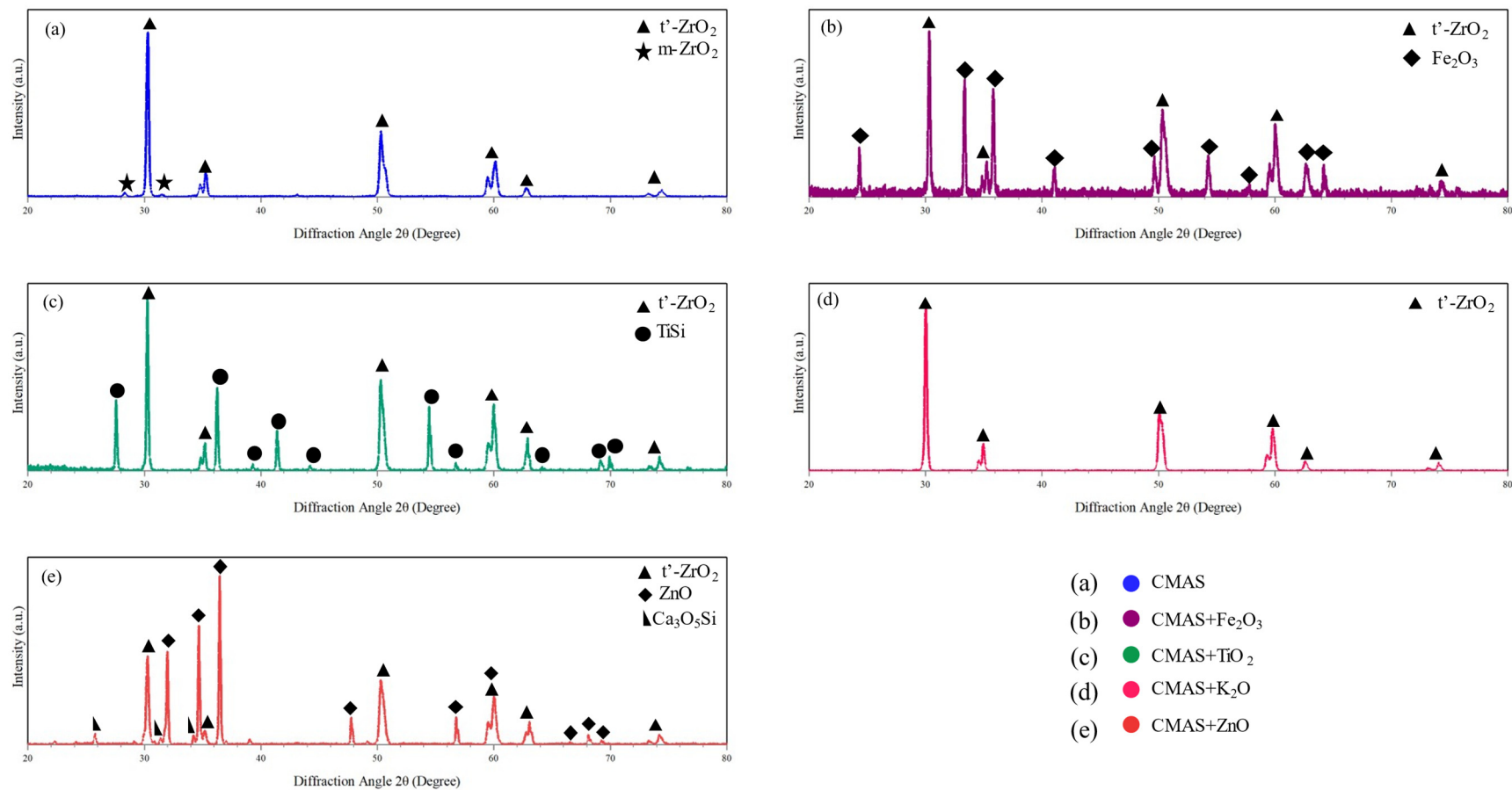
Fig. 5.5. XRD diffraction patterns of YSZ coatings after ablation with C-M-A-S constituents and glass modifiers.
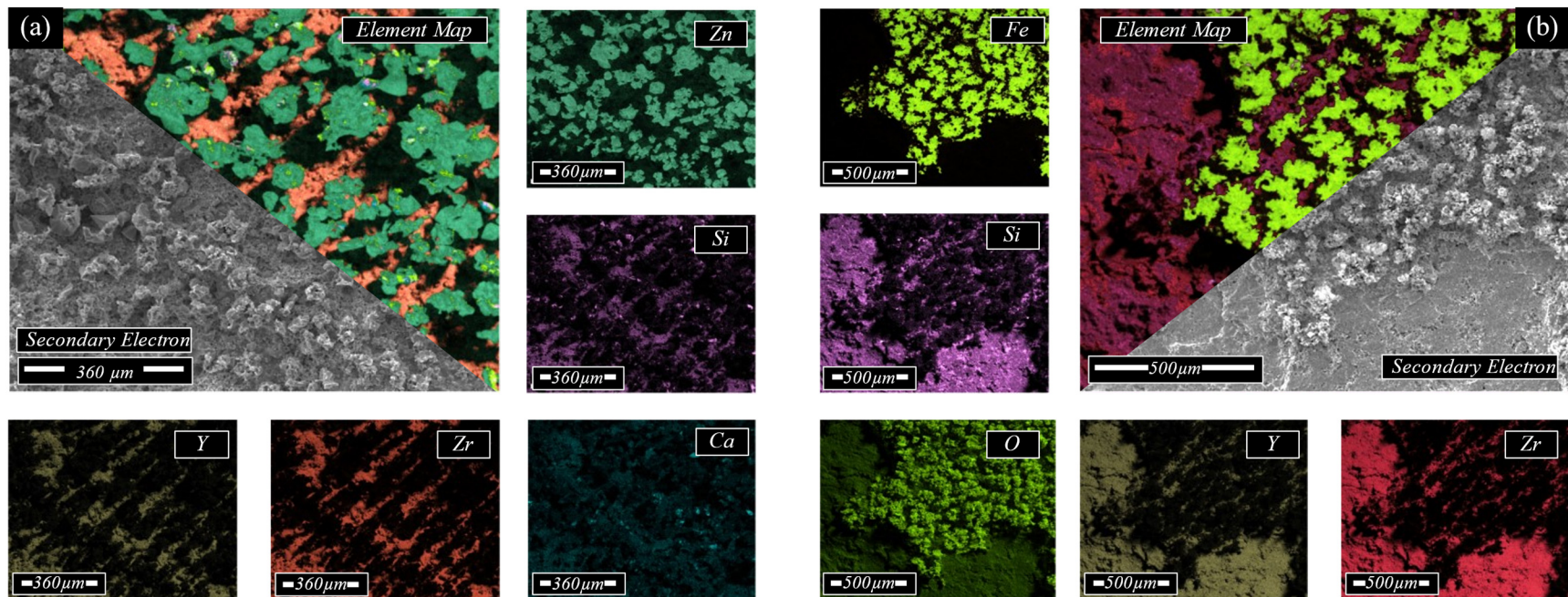
Fig. 5.6. EDS analysis of APS YSZ topcoats after 30 minutes of ablation, showing the impurities that crystallized on the surface when exposed to (a) CMAS – ZnO, and (b) CMAS – $Fe_2O_3$.
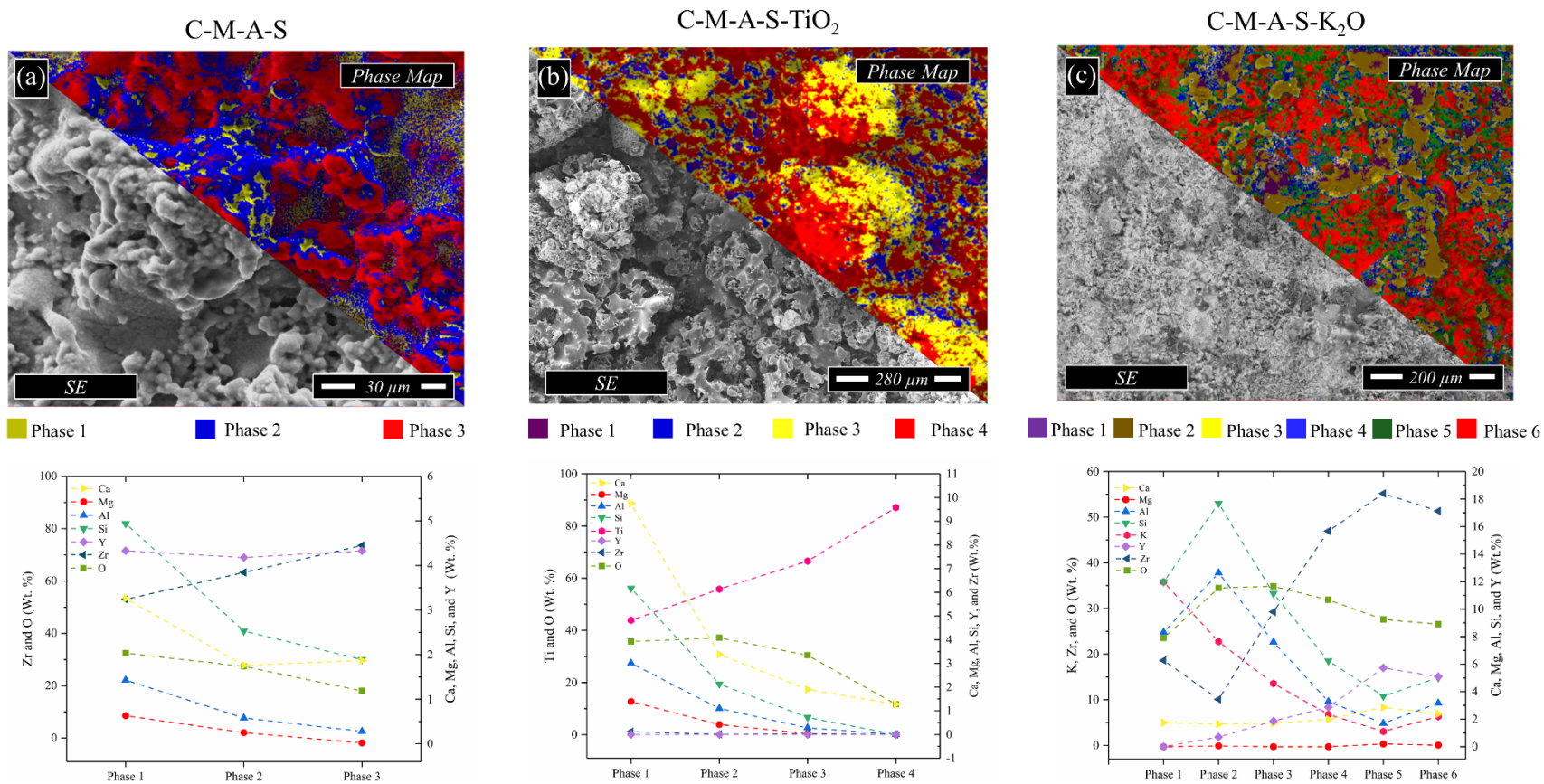
Fig. 5.7. SEM micrographs and EDS analysis of APS YSZ topcoats after ablation, showing the impurities crystallized on top of the coating and the resulting element concentration across each phase.

### 5.4.3 Analysis of APS TBCs cross-sections after ablation with C-M-A-S constituents and biofuel impurities

Fig. 5.8 shows the cross-sections of the TBCs ablated with biofuel impurities and a sample ablated without any impurities. The micrograph of the sample ablated during a total of 30 minutes (i.e., three ablation cycles) with no impurities, does not exhibit any sign of damage or degradation when compared to a sample in the as-received condition (Fig. 5.8a and Fig. 5.1a). In contrast, the samples exposed to glass modifiers and/or C-M-A-S exhibit different signs of degradation. Fig. 5.8b shows that the sample exposed to exclusively C-M-A-S developed cracks close to the bondcoat/topcoat interphase. Also, there was evidence that the impurities melted and infiltrated the coatings through paths created by the cracking of the topcoat. Fig. 5.8c and e show that the samples exposed to $Fe_2O_3$ and ZnO did not infiltrate the topcoat, in possibility due to the high melting point of the glass modifiers (above 1600°C). As a reminder the EDS analysis of $Fe_2O_3$ and ZnO impurities showed no traces of other elements (e.g., Ca, Mg) that could lower their melting point. However, in both cases, cracks nucleated and propagated in areas close to the solidified impurities, indicating that thermomechanical stresses evolved due to the thermal expansion mismatch between the impurities and the topcoat. Fig. 5.8d shows the sample sprayed with C-M-A-S-$TiO_2$; the cross-section micrograph displays a highly porous morphology in the spalled/infiltrated areas. Thus, the infiltrated/reacted areas delaminated due to a less strain tolerant morphology. The sample exposed to C-M-A-S-$K_2O$ shows that the impurities infiltrated the coating and reached the bondcoat. In this sample, signs of nucleation and propagation of cracks were visible in all the topcoat thickness (Fig. 5.8f). The full infiltration of the sample with $K_2O$, explains the fact that the XRD analysis performed on the topcoat surface, did not detect a secondary phase of impurities.

**(a)**
Topcoat: YSZ
No evidence of cracks
Bondcoat: NiCrAlY
Substrate: Inconel 718
425 μm

**(b)**
Solidified CMAS
Horizontal Cracks
CMAS Infiltration
85μm
375 μm

**(c)**
$Fe_2O_3$
Vertical Cracks
Cracks in the bondcoat proximity
430 μm

**(d)**
Porous spalled Coating
Infiltrated $TiO_2$
155μm
557 μm

**(e)**
Cracks close to the surface
ZnO
56 μm
110 μm

**(f)**
Surface cracks
Impurities reaching the bondcoat
225 μm

Fig. 5.8. Cross-section micrographs of APS TBCs after 30 minutes of ablation with (a) no impurities, (b) CMAS, (c) CMAS-$Fe_2O_3$, (d) CMAS-$TiO_2$, (e) CMAS-ZnO, and (f) CMAS-$K_2O$.

Summarizing, all the samples exposed to any combination of biofuel impurities caused the failure of the TBC. The glass modifiers that caused the most delamination (i.e., $Fe_2O_3$ and ZnO) did not mix with CMAS constituents to form secondary phases. Therefore, their effect on the TBCs can be assumed to be independent of other biofuel impurities. The sample that exhibited the fastest delamination was sprayed with impurities that reached the bondcoat when infiltrating the TBC and depleted the yttrium from the YSZ matrix. Interestingly, theoretical calculations demonstrated that C-M-A-S, in combination with $K_2O$, has the highest CTE when compared with the other impurities in the present study. Finally, only the samples exposed to C-M-A-S alone and in combination with $K_2O$ caused the depletion of Yttrium from the YSZ matrix.

## 5.5    Conclusions

This article analyzed the interaction of biofuel impurities with YSZ TBCs by replicating the thermal conditions at which the coatings operate in a gas turbine. It was found that in addition to the negative effect that C-M-A-S constituents have on the ceramic coatings, glass modifiers such as $Fe_2O_3$, $TiO_2$, ZnO, and $K_2O$ exacerbate the corroding effect of CMAS on YSZ. Micrographs and EDS analysis revealed that glass modifiers do not necessarily mix with CMAS constituents (i.e., $Fe_2O_3$ and ZnO). However, regardless of the melting temperature of biofuel impurities and their ability to mix with CMAS constituents, biofuel impurities hasten the delamination of the topcoat even without infiltrating the TBC. This study also discerned that, even though $TiO_2$ mix with C-M-A-S constituents to form secondary phases, the thermochemical interaction with YSZ was low enough that no depletion of Zr or Y was found across phases. Therefore, C-M-A-S-$TiO_2$ interacts only thermomechanically with the TBC. The samples that showed evidence of Yttria depletion were sprayed with C-M-A-S alone and C-M-A-S with $K_2O$.

## 5.6    Acknowledgments

# 5.7 References

[1] M. Okada, T. Hisamatsu, and T. Kitamura, "Examination on microstructural change of a bondcoat in a thermal barrier coating for temperature estimation and aluminum-content prediction," *Am. Ceram. Soc.*, **Advanced C** 61–69 (2008).

[2] S.I. Kim, M.H. Rahman, and I. Hassan, "Effect of turbine inlet temperature on rotor blade tip leakage flow and heat transfer," *Int. J. Numer. Methods Heat Fluid Flow*, **22** [1] 73–93 (2012).

[3] U. Desideri, Fundamentals of gas turbine cycles: Thermodynamics, efficiency, and specific power. *Woodhead Publishing Limited*, 2013.

[4] M. Seraffon, N.J. Simms, J. Sumner, and J.R. Nicholls, "The development of new bond coat compositions for thermal barrier coating systems operating under industrial gas turbine conditions," *Surf. Coat. Technol.*, **206** [7] 1529–1537 (2011).

[5] R. Vaben, D. Sebold, G. Pracht, and D. Stover, "Corrosion rig testing of thermal barrier coating systems," *Ceram. Eng. Sci. Proc.*, **27** [3] 47–60 (2007).

[6] W. Fan, Y. Bai, J.R. Li, Y. Gao, H.Y. Chen, Y.X. Kang, W.J. Shi, and B.Q. Li, "Microstructural design and properties of supersonic suspension plasma sprayed thermal barrier coatings," *J. Alloys Compd.*, **699** 763–774 (2017).

[7] N. Czech, H. Fietzek, M. Juez-lorenzo, V. Kolarik, and W. Stamm, "Studies of the bond-coat oxidation and phase structure of TBCs 1," **113** 157–164 (1999).

[8] T.R. Kakuda, C.G. Levi, and T.D. Bennett, "The thermal behavior of CMAS-infiltrated thermal barrier coatings," *Surf. Coatings Technol.*, **272** 350–356 (2015).

[9] R. Ochrombel, J. Schneider, B. Hildmann, and B. Saruhan, "Thermal expansion of EB-PVD yttria stabilized zirconia," *J. Eur. Ceram. Soc.*, **30** [12] 2491–2496 (2010).

[10] Y. Wang, M.X. Li, and H.L. Suo, "Mechanical properties of YSZ thermal barrier coatings with segmented structure," *Surf. Eng.*, **28** [5] 329–332 (2012).

[11] W. Ma and H. Dong, "Ceramic thermal barrier coating materials," *Therm. Barrier Coatings*, 25–52 (2011).

[12] H. Chang, C. Cai, Y. Wang, Y. Zhou, L. Yang, and G. Zhou, "Calcium-rich CMAS corrosion induced microstructure development of thermal barrier coatings," *Surf. Coatings Technol.*, **324** 577–584 (2017).

[13] X. Chen, "Calcium-magnesium-alumina-silicate (CMAS) delamination mechanisms in EB-PVD thermal barrier coatings," *Surf. Coatings Technol.*, **200** [11] 3418–3427 (2006).

[14] S. Krämer, J. Yang, C.G. Levi, and C.A. Johnson, "Thermochemical Interaction of Thermal Barrier Coatings with Molten CaO–MgO–Al$_2$O$_3$–SiO$_2$(CMAS) Deposits," **3175** 3167–3175 (2006).

[15]     V.H. Mohan, P., Patterson, T., Sohn, Y., & Desai, "Degradation of yttria stabilized zirconia thermal barrier coatings by molten CMAS (CaO-MgO-Al$_2$O$_3$-SiO$_2$) Deposits," *Mater. Sci. Forum*, **598** [January] 207–212 (2008).

[16]     A.R. Krause, H.F. Garces, G. Dwivedi, A.L. Ortiz, S. Sampath, and N.P. Padture, "Calcia-magnesia-alumino-silicate (CMAS)-induced degradation and failure of air plasma-sprayed yttria-stabilized zirconia thermal barrier coatings," *Acta Mater.*, **105** 355–366 (2016).

[17]     P. Mohan, T. Patterson, B. Yao, and Y. Sohn, "Degradation of thermal barrier coatings by fuel impurities and CMAS: Thermochemical interactions and mitigation approaches," *J. Therm. Spray Technol.*, **19** [1–2] 156–167 (2010).

[18]     C. Cai, S. Chang, Y. Zhou, L. Yang, G. Zhou, and Y. Wang, "Microstructure characteristics of EB-PVD YSZ thermal barrier coatings corroded by molten volcanic ash," *Surf. Coatings Technol.*, **286** 49–56 (2016).

[19]     A.D. Gledhill, K.M. Reddy, J.M. Drexler, K. Shinoda, S. Sampath, and N.P. Padture, "Mitigation of damage from molten fly ash to air-plasma-sprayed thermal barrier coatings," *Mater. Sci. Eng. A*, **528** [24] 7214–7221 (2011).

[20]     J. Di Campli, "Aeroderivative gas turbine fuel flexibility," *Power Eng.*, **117** [9] (2013).

[21]     A. Oasmaa and S. Czernik, "Fuel oil quality of biomass pyrolysis oils - state of the art for the end users," *Energy and Fuels*, **13** [4] 914–921 (1999).

[22]     J.P. Bons, J. Crosby, J.E. Wammack, B.I. Bentley, and T.H. Fletcher, "High-pressure turbine deposition in land-based gas turbines from various synfuels," *J. Eng. Gas Turbines Power*, **129** [1] 135–143 (2007).

[23]     S.C. Singhal and R.J. Bratton, "Stability of a ZrO$_2$(Y$_2$O$_3$) thermal barrier coating in turbine fuel with contaminants," *J. Eng. Gas Turbines Power*, **102** [4] 770–775 (1980).

[24]     A. Bradshaw, N.J. Simms, and J.R. Nicholls, "Hot corrosion tests on corrosion-resistant coatings developed for gas turbines burning biomass and waste derived fuel gases," *Surf. Coatings Technol.*, **228** 248–257 (2013).

[25]     J. Webb, B. Casaday, B. Barker, J. Bons, a D. Gledhill, and N.P. Padture, "Characteristics of Four Coal Ash Types," 1–10 (2011).

[26]     M.P. Borom, C.A. Johnson, and L.A. Peluso, "Role of environment deposits and operating surface temperature in spallation of air plasma sprayed thermal barrier coatings," *Surf. Coatings Technol.*, **86**–**87** 116–126 (1996).

[27]     J.H.R. Velasco, G. Kilaz, and R.W. Trice, "Application of biofuel impurities and effect on the hot corrosion of yttria-stabilized zirconia thermal barrier coatings," *Surf. Coat. Technol.* (2018).

[28]     A.A. Novopashin and N.N. Seregin, "Calculation of the thermal-expansion coefficient of silicate glasses from their structure-energy characteristics," *Sov. J. Glas. Phys. Chem.*, **60** [December] 389–395 (1979).

# 6. GENERAL CONCLUSIONS AND OUTLOOK

## 6.1 Summary and remarks

The growing importance of biofuels worldwide makes it necessary to identify and analyze the effect of alternative fuel contaminants on gas turbine components that were assumed to perform in conditions set by fossil fuel combustion. Mass spectrometry analysis of alternative fuels has shown that biofuels are simpler than fossil fuels. However, biofuel impurities composition and concentration are challenging to control due to their dependence on biomass source (e.g., grass, wheat, pine), and synthesizing process (e.g., FT, SIP, HEFA). The list of biofuel impurities includes the same corrosive compounds found in fossil fuels and contaminants with no precedent in gas turbines. Therefore, the combustion of biofuel in gas turbines arises the possibility to form CMAS without flying in a desert sand or volcanic ash environment and to exacerbate the corrosive effect of CMAS through the addition of more contaminants.

Within this thesis, we introduced a methodology that uses "impurity cocktails" to study the effect of varying compositions of biofuel impurities on TBCs. Advantages of using impurity cocktails are a partial separation of the erodent effect of flying particles to the thermochemical degradation originated by the composition of the deposits of impurities, and the capability to control the concentration of the contaminants deposited on the topcoat. To address the evaluation of TBCs in thermal conditions similar to a gas turbine, we designed and assembled an oxy-acetylene ablation rig. Our ablating setup took into consideration ASTM standards and the burner rigs at NASA and Julich. The capabilities of our instrumentation include the characterization of the burning atmosphere with digital flow meters that measure the oxygen/acetylene ratio, and the temperature measurement of the ablated surface and substrate. For the case of the ablated coating a special-wavelength pyrometer (i.e., 10.5µm), was used to diminish the error associated with changes of emissivity of YSZ, while for the substrate a long-wavelength pyrometer was used (8-14µm). Due to the low cost and excellent thermomechanical properties, a graphite sample holder was designed to fix the samples in the same position (i.e., characterized heat flux) and to allow natural or forced convection cooling of the substrate.

The work reported here enclosed three study cases. In the first one, an impurity cocktail with a CMAS reference composition was applied in equal concentrations on APS and EB-PVD TBCs. After depositing the impurities, the coatings were successively ablated in cycles of 10 minutes. SEM and EDS analysis elucidated differences in the degradation mechanisms that took place in each coating type. The APS coating exhibited spallation of the coating and the vertical cracks filled with presumable glass formed from CMAS impurities. With every ablation cycle, the APS sample continued losing material from the TBC. However, the impurities did not reach the bondcoat layer, presumably due to the tortuosity of pores and vertical cracks. For the case of the EB-PVD coating, the impurities infiltrated the topcoat thoroughly, crystallizing in the interface between the bondcoat and bondcoat. In both cases, cracks were observed propagating in the vecinity of the crystallizing impurities. It was found that no matter the deposition method employed to manufacture the TBCs, the samples exposed to CMAS delaminated after thirty minutes in the thermal gradient testing.

In a second study, the effect of the individual and combinations of C-M-A-S was investigated on APS TBCs. The study departed from the premise that contaminants found in biofuels include the necessary oxides to form CMAS-like compositions without flying in a desert sand or volcanic ash environment. APS YSZ TBCs were sprayed with six systems of impurities (i.e., S, C-S, C-A, C-A-S, C-M-S, C-M-A-S). After ablation cycling, cross-sections micrographs revealed that the deposited impurities induced the failure of the YSZ topcoats either by infiltrating the coating or by solidifying on the surface of the TBC. In any case, the evidence suggested that the CTE mismatch between the impurities and the topcoat induced the nucleation and propagation of cracks along the coating. However, EDS analysis elucidated that S, C-A, and C-S induced a thermochemical degradation of the YSZ by leaching yttrium out of the TBC matrix. Notoriously, the rate of degradation at which the samples delaminated was different in every case but not related to the number of contaminants applied to the samples. No evidence suggested that a single or a specific combination of impurities triggered the degradation of the TBCs.

In a final case of study, the impurities exclusive of biofuels were identified (i.e., $Fe_2O_3$, $TiO_2$, $ZnO$, and $K_2O$) and combined with C-M-A-S unreacted constituents. After spraying APS TBCs with the contaminants, the samples were ablated in the same thermal conditions as in previous studies. The goal was to identify biofuel impurities that could exacerbate the detrimental effect of

CMAS on YSZ TBCs. Evidence elucidated that the main factor contributing to the delamination rate (i.e., topcoat weight percent change) was the CTE of CMAS in combination with the additional impurities. The samples that exhibited the highest rate of degradation were exposed to $Fe_2O_3$ and ZnO. Only the system sprayed with $K_2O$ exhibited depletion of yttrium from the YSZ topcoat. Therefore, delamination rate of the samples was attributed mainly to thermomechanical interactions for the rest of the cases.

With the design and construction of the ablation rig, the effect of biofuel impurities on YSZ was studied with a validated methodology. This work was focused on the impurities concentration and composition deposited on TBCs to evaluate the lifetime of the coatings. However, Poreschke et al. [1] noted that not all PM flying through the engine adheres to the turbine blades since the thermal behavior, viscosity, and particle size change the adhesivity of the contaminants in the gas turbine. The last is important since the ultimate purpose of testing TBCs in the laboratory is to replicate the conditions encountered by a gas turbine as close as possible. To acquaint for the additional factors that may affect the behavior of biofuel impurities in the gas turbine, an in-progress improvement of the ablation rig contemplates the incorporation of a UniSprayJet-SE thermal spray gun (Ibeda Co., Neustadt, Germany), enabling ablation of samples with higher heat flux. Also, the thermal spray gun will enable the incorporation of a powder feeder model 1270 (Praxair Technology Inc., Indianapolis, USA) to spray powders with the composition of impurities directly into the flame. Both the thermal spray gun and powder feeder are intended for future studies taking into consideration contaminants chemistry, particle morphology, and rate of deposition of impurities. The ultimate purpose is to incorporate the parameters into a model that allows us to predict the lifetime reduction of TBCs based on the complete properties of the contaminants present in biofuels.

Finally, it is crucial to recognize that even though international efforts have focused on replicating the conditions of gas turbines in a laboratory, the main challenges are to mitigate the damage induced by CMAS and contaminants entering the gas turbines, predict the failure of TBCs, and to monitor operating conditions of the coatings. Some of the ideas under development are reviewed in this work.

## 6.2    Thermal barrier coatings outlook

### 6.2.1    Materials for mitigation of the effect of CMAS on TBCs

Hot corrosion of YSZ TBCs results in the eventual failure of the coatings, ultimately shortening the lifetime of blades and vanes. The efficiency loss in gas turbines due to molten impurities degradation makes it necessary to develop methodologies to protect TBCs from contaminants like CMAS. To provide protection against the thermomechanical and thermochemical effect originated from molten impurities that infiltrate the ceramic coatings, manufacturers have developed methodologies to deposit denser coatings to prevent corrosive elements infiltrate the TBC through the porous paths. High-Velocity Oxy-Fuel (HVOF) and cold spray,  allow to deposit feedstock with densities ranging between 0.5 and 5 %. However, the low porosity density does not eliminate the penetration of corrosive species. For that reason, there is a particular interest in developing methodologies capable of stopping the negative effect of corrosive compounds on TBCs. Hasz et al. [2] and Hazel et al. [3] patented methodologies to mitigate CMAS-induced degradation of TBCs. The most promising methodologies are using a sacrificial surface coating and manufacturing impermeable barrier coatings.

*Sacrificial coating*

One of the most promising approaches to mitigate the corrosive effect of molten impurities is adding an additional oxide layer  (e.g., $Al_2O_3$, MgO, $MgAlO_4$) on top of the TBC [4]. The purpose of the extra layer is to react with the adhered contaminants on the topcoat surface and modify their thermophysical properties, ultimately increasing the viscosity and melting temperature of the impurities. The main idea is that the highly viscous fluid of partially molten impurities will find it difficult to flow through the porous paths of TBCs. As a result, the depth of the infiltration of chemically modified impurities is lower than "raw" impurities. However, a drawback of this methodology is the consumption of the sacrificial coating through the interaction of the metallic oxide and the molten impurities. Therefore, a sacrificial coating only offers the possibility to extend the lifetime of the TBC by retarding the effect of contaminants like CMAS. Also, Mukherjee et al. [5] noted that a sacrificial coating only limits the infiltration of CMAS into the TBC, but the corrosive effect of the contaminants is not completely mitigated. Therefore, it could be expected the eventual failure of the TBC as the sacrificial coating is depleted.

*Impermeable barrier coating*

A recent proposal to mitigate the infiltration of molten CMAS is to tailor the surface of TBCs as to fabricate an impermeable topcoat. By employing a laser glazing, Batista et al. [6] modified the surface of a YSZ topcoat to fabricate a non-wetting surface at the top of the TBC. When the modified TBCs were exposed to CMAS, the molten impurities were incapable of sticking to the TBC surface. Similar observations in surface-modified TBCs exposed to $Na_2SO_4$ and $V_2O_5$ indicated that the corrosion of the coatings was minimized. However, as with sacrificial coatings, impermeable barrier coatings did not stop the negative effect of the corrosive impurities. Even though impurities did not adhere to the TBC surface, a fraction of the molten impurities were capable of the TBC through the vertical cracks or porous paths of the sample.

*Reactive coatings:*

A promising idea to develop coatings capable of providing ultimate protection against corrosive compounds is reactive coatings, reactive materials that upon contact with contaminants (i.e., ash, sand), seals the passages in the coating and avoid further infiltration [7, 8]. However, reactive coatings rely on a fast-thermochemical interaction of the coating with the melt to seal the tortuous path to the coating. Therefore, one of the limitations of reacting coatings is finding materials with the proper characteristics for TBCs and capable of reacting when exposed to molten impurities. Drexler et al. [9] studied the interaction of rare earth element zirconates with CMAS. The study concluded that $Y_2Zr_2O_7$, $Yb_2Zr_2O_7$, and $Gd_2Zr_2O_7$ reacted with CMAS and sealed the open passages of the TBCs through the formation of secondary phases (e.g., apatite and anorthite). However, the use of $Y_2Zr_2O_7$, $Yb_2Zr_2O_7$, and $Gd_2Zr_2O_7$ as TBCs is limited by low erosion-resistance and low strain tolerance.

### 6.2.2 Smart coatings for gas turbines applications

Smart coatings are considered the next step in the development of coatings with improved capabilities. In contrast to the passive response of traditional coatings, smart TBCs, offer the capability to react in proportion to and external event. Martin-Tejero et al. [10] reviewed smart coatings technologies under development. Some of the applications currently being researched are photoluminescent coatings and self-healing thermal barrier coatings.

*Photoluminescent Coatings:*

Rather than focusing only on mitigation of the effect of molten impurities on TBCs, smart coatings offer the capability to provide information about the operating condition of the coatings. Photoluminescent coatings offer the capability to monitor the TBC temperature through the incorporation of rare-earth (RE) doped layers that have a temperature dependence of fluorescence. The primary advantage is that this method provides a practical manner to monitor the surface and in-depth temperature of the coating. Eldridge et al. [11] incorporated layers of ($Y_2O_3$:Eu) as thick as 25 μm in between the typical morphology of a YSZ topcoat and characterized the coating temperature in function of the luminescence of the $Y_2O_3$: Eu layers. However, one of the main concerns with the application of a photoluminescent layer on TBCs is the possibility to shorten the coating lifetime due to thermomechanical stresses inherent of the CTE mismatch of YSZ and $Y_2O_3$: Eu. Several authors have conducted successful studies in which by using the proper ratio of Eu in yttria, the modified coating has matched the lifetime of a common TBC [12–15].

*Self-healing coatings:*

Regardless of the interaction between molten impurities with a TBC, regular heating and cooling cycles characteristic of gas turbines introduce thermal stresses that eventually induce the nucleation and propagation of cracks along the TBC. Nozahic et al. [16] analyzed the possibility of developing coatings capable of "healing" when a crack propagates along the TBC. The concept introduces the possibility to incorporate microcapsules containing a self-healing agent at the moment of thermally spraying the YSZ topcoat on bondcoat and substrate layers [17, 18]. The microcapsules trapped in the matrix of the YSZ, act as a reservoir of material that releases a filling agent when cracks propagating in the topcoat break the microcapsules. Derelioglu et al. [19] incorporated $Al_2O_3$ particles filled with $MoSi_2$ (filling agent) in an APS YSZ topcoat. The study demonstrated that cracks propagating along the YSZ matrix stopped when encountering the $MoSi_2$ material that oxidized and solidified upon reaction with the air. Even though the methodology offers a possibility to counter the propagation of cracks on TBCs, it has been demonstrated that $MoSi_2$ alters the thermal conductivity of the TBC once activated [16, 20]. Lastly, the change of thermal conductivity becomes an issue as the percentage of filler material increases in the overall YSZ matrix, making the superalloy substrate susceptible to thermal-induced damage. Currently,

research has focused on developing materials capable of acting as healing agents without compromising the thermal and mechanical properties of the TBCs.

The introduction of new capabilities in thermal barrier coatings results of importance to monitor the operating conditions and lifetime of TBCs. Even though properties inherent of materials have helped to reduce the effect of molten impurities on the lifetime of TBCs, it is necessary to explore the possibilities that smart coatings carry with them. The final objective is not only to eliminate the detrimental effect of external particles that adhere and melt on the surface of the coatings but also to provide TBCs capable of adapting to the operating conditions, rather than behaving passively with the surrounding environment. Although preliminary tests of self-healing and photoluminescent coatings have proved to be useful, it is necessary to continue research in these fields in order to maximize the utility of the TBCs or at least match actual performance levels.

## 6.3    References

[1]     D.L. Poerschke, R.W. Jackson, and C.G. Levi, "Silicate Deposit Degradation of Engineered Coatings in Gas Turbines: Progress Toward Models and Materials Solutions," *Annu. Rev. Mater. Res.*, **47** [1] 297–330 (2017).

[2]      and M.P.B. W. C. Hasz, C. A. Johnson, "Protection of Thermal Barrier Coating by a Sacrificial Surface Coating," *U.S. Pat. 5,660,885,* [19] 1–5 (1997).

[3]     C.G. Brian Thomas Hazel, Irene Spitsberg and B.A. Nagaraj, "Protection of Thermal Barrier Coating With an Impermeable Barrier Coating," *US 2006/0115659 A1*, (2006).

[4]     A.K. Rai, R.S. Bhattacharya, D.E. Wolfe, and T.J. Eden, "CMAS-resistant thermal barrier coatings (TBC)," *Int. J. Appl. Ceram. Technol.*, **7** [5] 662–674 (2010).

[5]     B. Mukherjee, A. Islam, K.K. Pandey, O.S. Asiq Rahman, R. Kumar, and A.K. Keshri, "Impermeable $CeO_2$ overlay for the protection of plasma-sprayed YSZ thermal barrier coating from molten sulfate-vanadate salts," *Surf. Coatings Technol.*, **358** [October 2018] 235–246 (2019).

[6]     C. Batista, A. Portinha, R.M. Ribeiro, V. Teixeira, M.F. Costa, and C.R. Oliveira, "Morphological and microstructural characterization of laser-glazed plasma-sprayed thermal barrier coatings," *Surf. Coatings Technol.*, **200** [9] 2929–2937 (2006).

[7]     C.G. Levi, J.W. Hutchinson, M.-H. Vidal-Sétif, and C.A. Johnson, "Environmental degradation of thermal-barrier coatings by molten deposits," *MRS Bull.*, **37** [10] 932–941 (2012).

[8]     D.R. Clarke and C.G. Levi, "Materials design for next-generation thermal barrier coatings," *Annu. Rev. Mater. Res.*, **33** [1] 383–417 (2003).

[9]     A.D. Gledhill, K.M. Reddy, J.M. Drexler, K. Shinoda, S. Sampath, and N.P. Padture, "Mitigation of damage from molten fly ash to air-plasma-sprayed TBCs," *Mater. Sci. Eng. A*, **528** [24] 7214–7221 (2011).

[10]     D. Tejero-Martin, M. Rezvani Rad, A. McDonald, and T. Hussain, *Beyond Traditional Coatings: A Review on Thermal-Sprayed Functional and Smart Coatings*. 2019.

[11]     J.I. Eldridge, T.J. Bencic, S.W. Allison, and D.L. Beshears, "Depth-penetrating temperature measurements of thermal barrier coatings incorporating thermographic phosphors," *J. Therm. Spray Technol.*, **13** [1] 44–50 (2004).

[12]     F. Abou Nada, A. Lantz, J. Larfeldt, N. Markocsan, M. Aldén, and M. Richter, "Remote temperature sensing on and beneath atmospheric plasma sprayed thermal barrier coatings using thermographic phosphors," *Surf. Coatings Technol.*, **302** 359–367 (2016).

[13]     L. Yang, D. Peng, C. Zhao, C. Xing, F. Guo, Z. Yao, Y. Liu, X. Zhao, *et al.*, "Evaluation of the in-depth temperature sensing performance of Eu- and Dy-doped YSZ in air plasma sprayed thermal barrier coatings," *Surf. Coatings Technol.*, **316** 210–218 (2017).

[14]     W. a Ellingson, R.J. Visher, R.S. Lipanovich, and C.M. Deemer, "Optical NDT Methods for Ceramic Thermal Barrier Coatings," *Mater. Eval.*, **64** 45–51 (2006).

[15]     X. Chen, Z. Mutasim, J. Price, J.P. Feist, A.L. Heyes, and S. Seefeldt, "Industrial sensor TBCs: Studies on temperature detection and durability," *Int. J. Appl. Ceram. Technol.*, **2** [5] 414–421 (2005).

[16]     F. Nozahic, D. Monceau, and C. Estournès, "Thermal cycling and reactivity of a $MoSi_2/ZrO_2$ composite designed for self-healing thermal barrier coatings," *Mater. Des.*, **94** 444–448 (2016).

[17]     T. Ouyang, X. Fang, Y. Zhang, D. Liu, Y. Wang, S. Feng, T. Zhou, S. Cai, *et al.*, "Enhancement of high-temperature oxidation resistance and spallation resistance of SiC-self-healing thermal barrier coatings," *Surf. Coatings Technol.*, **286** 365–375 (2016).

[18]     J. Kulczyk-Malecka, X. Zhang, J. Carr, F. Nozahic, C. Estournès, D. Monceau, A.L. Carabat, W.G. Sloof, *et al.*, "Thermomechanical properties of SPS produced self-healing thermal barrier coatings containing pure and alloyed MoSi2 particles," *J. Eur. Ceram. Soc.*, **38** [12] 4268–4275 (2018).

[19]     Z. Derelioglu, A.L. Carabat, G.M. Song, S. van der Zwaag, and W.G. Sloof, "On the use of B-alloyed $MoSi_2$ particles as crack healing agents in yttria stabilized zirconia thermal barrier coatings," *J. Eur. Ceram. Soc.*, **35** [16] 4507–4511 (2015).

[20]     K. Portilla-Zea, M.A. González, E. Rodríguez, O. Jiménez, D. Bravo-Bárcenas, and G.I. Vásquez, "Effect of SiC microfibers as a self-healing agent and their influence on oxidation and adhesion resistance of thermal barrier coatings exposed to cyclic thermal oxidation treatments," *Surf. Coatings Technol.*, **372** [May] 376–389 (2019).

# VITA

July 12, 1988             Born – Distrito Federal, México

2010             Six Sigma Green Belt Certification
Arizona State University
Arizona, United States of America

2011             B.S., Mechatronics Engineering
ITESM - CEM
Estado de México, México

2012-2013             Siemens Business Learning Program
Siemens AG
Distrito Federal, México

2013-2016             Research & Development (R&D) Engineer
Siemens – Energy Sector
Querétaro, México

2016-Present             Ph.D. Candidate / Research Assistant
Purdue University
Indiana, United States of America

# CONFERENCE PROCEEDINGS

[1] P. Vozka, M. Romanczyk, **J.H. Ramirez Velasco**, R. Trice, H. Kenttämaa, G. Kilaz. Relationship between fuel chemical composition and fuel properties. Poster presented on the Annual ONR NEPTUNE Program Review, UC Davis, CA.

[2] M. Romanczyk, **J.H. Ramirez Velasco**, P. Vozka, L. Xu, K. Wehde, B. Modereger, R.W. Trice, G. Kilaz, & H. Kenttämaa. Design of Next-Generation Renewable Fuels. Poster presented at the ONR Neptune Program Review, Annapolis, MD. November 2017.

[3] M. Romanczyk, **J.H. Ramirez Velasco**, P. Vozka, K. Wehde, B. Modereger, L, Xu, N. Roe, E. Keating, J. Healy, A. Gordon, R.W. Trice, G. Kilaz, & H. Kenttämaa. Composition/Property/Performance Correlations for Rational Development of Renewable Aviation Fuels. Poster presented at the MIT Energy Initiative, Boston, MA. May 2017.

[4] P. Vozka, M. Romanczyk, K. Wehde, **J.H. Ramirez Velasco**, R. Trice, H. Kenttämaa, & G. Kilaz. Alternative Aviation Fuel Chemistry-Performance Correlations Towards a Sustainable Future. Poster presented at the Purdue Spring Reception, West Lafayette, IN. May 2017.

[5] M. Romanczyk, K. Wehde, P. Vozka, J. Kong, **J.H. Ramirez Velasco**, R. Yerabolu, H. Kenttämaa, G. Kilaz, R.W. Trice. Fundamental Studies on Composition/Performance Correlations for Aviation Fuels. Poster presented on the Naval Enterprise Partnership Teaming with Universities for National Excellence, UC Davis, CA. November 2016.

[6] J. Kong, X. Zhao, **J.H. Ramirez Velasco**, M. Romanczyk, R. Kumar, R. Yerabolu, L. Henderson, Y. An, D. Fearnow, R.W. Trice, G. Kilaz, & H. Kenttämaa. Fundamental Studies on Composition/Performance Correlations for Aviation Fuels. Poster presented on the NEPTUNE fair at Arizona State University, Tempe, AZ. May 2016.

# PUBLICATIONS

*Parts of this thesis have been published in the following journal articles:*

[1] **J.H. Ramirez Velasco**, K. Petrosky. G. Kilaz, and R.W. Trice, "The combined effect of CMAS and biofuel impurities on the degradation of yttria-stabilized zirconia thermal barrier coatings." In preparation.

[2] **J.H. Ramirez Velasco**, K. Petrosky. G. Kilaz, and R.W. Trice, "Thermochemical interaction of biofuel impurities with yttria-stabilized zirconia thermal barrier coatings," In preparation.

[3] **J.H. Ramirez Velasco**, G. Kilaz, and R.W. Trice, "Application of biofuel impurities and effect on the hot corrosion of yttria-stabilized zirconia thermal barrier coatings," Surf. Coat. Technol. (2018). DOI: 10.1016/j.surfcoat.2018.10.019

[4] M. Romanczyk, **J.H. Ramirez Velasco**, Lan Xu, Petr Vozka, Pankaja Dissanayake, Katherine E. Wehde, Nathaniel Roe, Eion Keating, Gozdem Kilaz, Dianne J. Luning Park, Rodney W. Trice, Hilkka Kenttäämaa "The capability of organic compounds to swell acrylonitrile butadiene O-rings and their effects on O-ring mechanical properties," Fuel, (2018). DOI: 10.1016/j.fuel.2018.10.103